

GUT Monopole Detection

with Scintillator

Thesis by

Charles E. Lane

In partial fulfillment of the requirements

for the Degree of

Doctor of Philosophy

California Institute of Technology

Pasadena, California

1988

(submitted September 25, 1987)

Acknowledgments

I would like to express my thanks to my advisor, Professor Barry Barish, for his guidance and support, and to Professor Charlie Peck for the many discussions regarding liquid scintillator counters. My thanks also go to my friend and co-worker Gang Liu, for many years of work together.

Much of my work has been in connection with the MACRO collaboration, and I would like to thank all those in MACRO who have helped to make my participation enjoyable and challenging.

I would like to thank Professor Arie Bodek for the loan of the scintillator used in the prototype monopole detector. Thanks should also go to Dr. Robert Chrien and the staff of the HFBR at Brookhaven National Laboratory for making the low β scintillation experiment possible.

My work at Caltech has been supported by NSF and Millikan Fellowships, and I would like to express my appreciation for their support.

Abstract

Searches for the monopoles predicted by Grand Unified Theories (GUTs) have required new approaches, since these monopoles should be both slow and highly penetrating. The ability of scintillator to respond to particles of velocity $< 10^{-3} c$ has been demonstrated, indicating that scintillator detectors should be useful in GUT monopole searches.

A small monopole detector prototype at the Earth's surface was operated in an effort to understand the problems and possibilities of monopole detection. The design philosophy, techniques, and the lessons learned from the prototype detector could then be applied to much larger monopole detectors. The prototype was not able to set new limits for the GUT monopole flux in cosmic rays, but in a more general analysis it was found that new limits could be set on the flux of lightly ionizing particles of mass $\sim 10^{10}$ GeV.

When GUT monopole detectors are scaled up to the size needed to chal-

lenge astrophysical limits, it becomes more likely that a flux could be found. This motivates a more careful examination of the scintillator counters, since their signal should be clear and unambiguous for a monopole candidate. The performance of the liquid scintillator counters for the MACRO (Monopole And Cosmic Ray Observatory) experiment was given considerable scrutiny, both to try to understand the observed behavior of these counters, and also to improve them for monopole detection.

The results of these tests indicate that MACRO should be able either to establish a monopole flux or to limit it to a small fraction of the 'missing mass' of the universe.

Contents

Acknowledgments	ii
Abstract	iii
List of Figures	x
1 Introduction	1
1.1 Monopoles in GUTs	6
1.2 Monopoles in Astrophysics	9
1.2.1 The Parker Bound	10
1.2.2 Monopole velocities	12
1.2.3 Discussion	13
1.3 Summary	14

2	Monopole Scintillation	16
2.1	Introduction	16
2.2	Monopole Stopping Power	18
2.2.1	Fast Projectiles	19
2.2.2	Slow Projectiles	21
2.3	Scintillation Yield	26
2.4	Other Energy Loss Terms	31
2.5	Summary	32
3	Low β Scintillation Experiment	35
3.1	Description	35
3.2	The Data	43
3.3	Backgrounds	48
3.3.1	Randoms	48
3.3.2	Multiple Scattering in the Target	49
3.3.3	Compton Scattering and Capture Reactions	50
3.3.4	Neutron Scattering and Capture in Wax PMT Enclosures	51
3.3.5	Trigger Electronics Effects	52
3.3.6	Discussion	53

3.4	Analysis	54
3.4.1	^6Li -glass Scintillator Efficiency	55
3.4.2	Scattering Probability	58
3.4.3	Fitting TOF Peaks	61
3.4.4	Neutron Beam Intensity	64
3.4.5	Light Yields	69
3.4.6	Discussion	74
3.5	Conclusions	78
4	The Caltech Prototype Monopole Detector	81
4.1	Introduction	81
4.2	General Description	84
4.3	Acquisition Electronics	89
4.4	Operation & Analysis	96
4.4.1	The Data	99
4.4.2	Slow Particle Analysis	101
4.5	Results	102
4.6	Conclusions	109
5	Liquid Scintillator Optics	111

5.1	Introduction	111
5.2	Basic Concepts	114
5.2.1	Total Internal Reflection	114
5.2.2	A Standard Counter	115
5.2.3	Attenuation	118
5.2.4	Design Variations	122
5.3	Total Internal Reflection Optics	123
5.4	Solid Angle Calculations	126
5.5	The Optical Monte Carlo	131
5.6	End Mirrors and Focussing	133
5.6.1	Flat Mirrors	134
5.6.2	Focussing Mirrors	136
5.7	Lining Materials	145
5.7.1	Dielectric Lining Materials	145
5.7.2	Metallic Linings	146
5.7.3	Aluminum-Backed Teflon	149
5.7.4	Vinyl-Backed Teflon	152
5.7.5	The Effect of Wrinkles	154
5.8	Timing	158

5.8.1	Optical Pulse Shape	159
5.8.2	Timing Jitter	164
5.9	Wavelength Dependence	169
5.9.1	Window Materials	170
5.9.2	Bulk Attenuation	172
5.10	Prototype Results	173
5.11	MACRO Counters	176
5.12	Response to Magnetic Monopoles	178
5.13	Conclusions	179
6	Conclusions	181
A	The Optical Monte Carlo	183
A.1	Description of a Surface	184
A.2	Optical Surfaces	186
A.3	Sources & Rays	187

List of Figures

1.1	Astrophysical limits on GUT monopole flux	11
2.1	Stopping power of protons in NE-110	23
2.2	Dirac monopole stopping power in NE-110	25
2.3	Stopping power to excite electrons across a 5 eV band gap	28
2.4	Scintillation efficiency for protons in NE-110	30
3.1	Layout of HFBR experiment.	36
3.2	Energy of recoil proton with θ	38
3.3	Calculated HFBR filtered neutron beam flux	40
3.4	Trigger electronics for the low β scintillation experiment	41
3.5	Neutron time-of-flight histogram at $\theta = 30^\circ$	44
3.6	Neutron time-of-flight histogram at $\theta = 20^\circ$	45

3.7	Neutron time-of-flight histogram at $\theta = 15^\circ$	46
3.8	^6Li Glass scintillator efficiency	55
3.9	Comparison of scattering probability per unit solid angle.	60
3.10	Fits of runs at 45° and 7.5°	65
3.11	Calculated photoelectron yield as a function of proton recoil energy.	69
3.12	Averaged photoelectron yield as a function of proton recoil energy for all runs. A least-squares fit to the data is shown.	71
3.13	Light yield of recoil protons as function of energy.	74
3.14	Scintillation efficiency calculated from light yield fit	76
3.15	Results of this experiment, and more recent low β scintillation results	79
4.1	Monopole signature expected for slow, lightly ionizing monopole.	83
4.2	The Caltech Prototype Monopole Detector.	85
4.3	Caltech Prototype Electronics overview	87
4.4	Pairs of DAQs used to record PMT pulse times	92
4.5	Event taken with slow particle trigger	93
4.6	Fast particle event taken with the detector	99

4.7	An event which fired the slow particle trigger	100
4.8	A stopping muon event	103
4.9	Lifetime curve for cosmic ray μ s stopping in the detector . . .	104
4.10	Comparison of the monopole flux limit	106
4.11	Limit of the fraction of dark matter that can be attributed to heavy charged particles, as a function of mass.	108
5.1	Liquid scintillation counter prototype	116
5.2	Response curve of the Caltech MACRO prototype counter . .	119
5.3	Factor for obtaining the effective attenuation length	121
5.4	Solid angles useful in analyzing rectangular liquid scintillator boxes	127
5.5	Solid angle that can propagate by total internal reflection . . .	130
5.6	Response curve obtained by OMC2 for a Teflon-lined scintilla- tion counter	132
5.7	Response curve for a counter with flat end mirrors	134
5.8	Time distribution of photoelectron pulses calculated by OMC2	135
5.9	Drawing of the MACRO horizontal counters	138
5.10	Focussing cone intensity comparison	139

5.11 Compound parabolic ('Winston' cone) curve calculated for MACRO liquid scintillation counters	140
5.12 Polar plot of the intensity/unit area for a PMT with a Winston cone	143
5.13 Intensity/area on a PMT	144
5.14 Calculated response curve for metallic lining	148
5.15 Average reflectivity of an aluminized Teflon lining	150
5.16 Response curve of a scintillation counter with an aluminized Teflon lining	151
5.17 Comparison of response curves for a MACRO counter with several different linings	153
5.18 Response curves for a counter with a wrinkled Teflon lining . .	155
5.19 Values of the attenuation from fits of wrinkled Teflon response curves	156
5.20 Values of the acceptance level from fits of wrinkled Teflon re- sponse curves	157
5.21 Time distribution of light calculated analytically, compared with OMC2 data for the same optical configuration.	161
5.22 Calculated time distributions of light for various counter linings	162

5.23	Time distribution of light from a $\beta = 1$ cosmic ray	165
5.24	Time of first photoelectron	167
5.25	Time difference between PMTs	168
5.26	Transmission of PVC windows	170
5.27	Response curves for the liquid scintillator prototype with clear acrylic windows	171
5.28	Response curve from the Michigan prototype	174

List of Tables

2.1	NE-110 Properties Summary	17
3.1	Comparison of calculated and Monte Carlo ϵ_{Li} values	57
3.2	HFBR Experiment Run Summary	62
3.3	Calculated Neutron Beam Intensities	68
3.4	HFBR Light Yields	70
3.5	HFBR Light Yield Averages by Scattering Angle	72

Chapter 1

Introduction

Dirac¹ introduced Magnetic monopoles into quantum physics and showed that the magnetic charge is quantized in units of $e/2\alpha$, where $\alpha \approx 1/137$ is the fine structure constant. There were a number of searches for Dirac magnetic monopoles, but there was little theoretical guidance to the masses of these monopoles or the way in which they could be produced. More recently, Grand Unified Theories (GUTs) have been postulated in which magnetic monopoles are a natural consequence of the theory. This has given impetus to the search for magnetic monopoles, since monopoles are a result of a broad class of these GUT theories.

The GUT monopole has a magnetic charge quantized in units of the

Dirac charge ($e/2\alpha$), and a mass of order of the GUT scale ($\sim 10^{16}$ GeV). The large mass of GUT monopoles indicate that they would be impossible to produce in the laboratory in the foreseeable future, and so one must search for these monopoles as remnants of the extremely high temperatures in the early universe. The presence (or absence) of remnant GUT monopoles is thus one of the few probes one has for the very high-energy GUT scale.

The searches for GUT monopoles, like those for other hypothetical particles, are also impelled by the 'missing mass problem' of cosmology and astrophysics. In short, it appears that much of the mass density of the universe isn't visible to normal observation and is possibly non-baryonic. Monopoles are possible constituents of the missing mass, and the search for magnetic monopoles therefore has implications for cosmology.

This thesis is primarily concerned with monopoles and their detection, emphasizing the design, construction and analysis of monopole detectors. The monopole detection effort at Caltech has evolved from one of trying new and different detection techniques to one of designing and building a large underground monopole detector known as MACRO.

The expected flux of GUT monopoles is quite low, so an inexpensive detector technology is desirable for covering large areas. Scintillation count-

ers are attractive in this respect, but there was some uncertainty about the amount of signal that a monopole would produce in scintillator. The major question was in the amount of scintillation that could be produced by a very slow particle like a GUT monopole.

Some experimental guidance was called for, and S. Ahlen, T. Liss, G. Liu and I went to Brookhaven National Laboratory with an experiment to try to observe scintillation light from low-velocity protons. The experiment has been reported elsewhere², and the results have since been extended to lower velocities³, but the experiment has not been fully described in the literature.

This thesis contains a description of the low-velocity scintillation experiment, of which my own contribution was the trigger electronics. I will also present an independent analysis of the experimental data, which I hope is more thorough than the original analysis. The experiments at Brookhaven showed that scintillation occurs even for very low-velocity protons.

This gave considerable confidence that slow monopoles could also be detected with scintillator, but some experience in the construction and operation of scintillator monopole detectors was also desirable before a major monopole detector project was attempted.

The Caltech monopole group put together a small (4.6 m^2) scintillator

monopole detector prototype, using plastic scintillator borrowed from a Fermilab neutrino experiment. I will describe the prototype in more detail in Chapter 4, giving an overall picture of its construction and operation. My own contribution to the prototype was primarily in the data acquisition electronics and software, particularly in the modification and testing of DAQ modules to be used as a waveform digitizer. I also did some analysis of the prototype data, primarily in extracting the stopping muon decay curve, and in testing and tuning the acquisition system.

We learned a number of valuable things from the Caltech prototype; in particular, we learned the value of a closed geometry and of going underground to reduce the backgrounds. These factors also motivated a number of the people involved with monopole scintillator detectors to form a collaboration to build a large underground detector: MACRO. The MACRO detector provides the ability for the first time to search directly for monopole fluxes below the astrophysical bounds. The MACRO detector, as of this writing, is in the early stages of construction, but much design and development had to be done before the detector could be proposed⁴.

The large area of such a detector drives the detection technology towards the use of large individual scintillator counters. The main constraint in in-

creasing the size of counters is the attenuation length of the scintillator. Plastic scintillators have attenuation lengths of 1–2 m, but a few liquid scintillators were found that have 5–7 m attenuation lengths, and so attention was turned toward liquid scintillator techniques.

A prototype of a MACRO liquid scintillator counter was built at Caltech, and a number of tests were done with it. I developed a Monte Carlo ray-tracing program that was used to examine some timing and light collection questions, and also (with S. Torres) examined the differences between the Caltech prototype and a prototype built with different techniques at the University of Michigan.

I will try to examine the liquid scintillator work in a coherent way, not as it actually happened, and to indicate the understanding that has emerged from these dissections of counter performance. Some of the more recent results, such as the measurements of scintillator oil attenuation length, will be mentioned only in passing. These results are of interest in the design of MACRO counters, but they can mostly be ‘decoupled’ from the rest of the counter design issues, and my involvement in them was peripheral.

Inevitably, there was much work that was not included in this thesis, but that formed an important background for the development of monopole

detection techniques and of the MACRO collaboration.

1.1 Monopoles in GUTs

Monopoles arise in non-Abelian GUTs when there is a compact covering group G that has a $U(1)$ factor when it is broken. The breakdown may be illustrated schematically (with a standard model) by

$$G \rightarrow SU_c(3) \times SU_L(2) \times U_Y(1) \rightarrow SU_c(3) \times U_{EM}(1),$$

where the second breakdown here is due to the electroweak theory. The GUT mass scale is on the order of 10^{14} – 10^{18} GeV, and it is at this mass scale that the breakdown of G occurs. The ‘desert hypothesis’ asserts that there are no intermediate mass scales between the GUT scale and the electroweak scale (~ 100 GeV), and so the results of GUT calculations need not be modified by intermediate scale physics.

The covering group G is broken when the scalar field Φ takes a vacuum expectation value. It was shown by ‘t Hooft⁵ and Polyakov⁶ that suitable configurations of Φ describe magnetic monopoles. These configurations cannot be transformed to the vacuum by a gauge transformation and so are

topologically stable. The GUT monopoles produced by this mechanism have a Dirac magnetic charge

$$Q_M = e/2\alpha \approx \frac{137e}{2},$$

or some multiple of a Dirac charge, which appears quite naturally in the theory.

't Hooft used an example with $G = SO(3)$ in which the monopole solution is particularly clear; if T_i are the generators of G ($i = 1, \dots, 3$), then the monopole solution has

$$\Phi = \phi(r)r_i T_i$$

(for a monopole at the origin). It can be seen that Φ is in a 'hedgehog' configuration: the direction in group space is aligned with the direction vector r . Such a configuration cannot be unwound by a gauge transformation. The *ansatz* for Φ can be inserted into the $SO(3)$ Lagrangian

$$\mathcal{L} = -\frac{1}{4}\text{Tr}G_{\mu\nu}G^{\mu\nu} - \frac{1}{2}\text{Tr}D_\mu\Phi D^\mu\Phi - V(\Phi)$$

and a solution obtained for $\phi(r)$ and the gauge fields. When the electromagnetic part of the gauge field is extracted, one finds that it describes the field of a magnetic monopole at the origin.

't Hooft showed only an $SO(3)$ monopole, but indicated that the solutions should exist in a large class of gauge theories. Explicit monopole solutions have been found for more realistic covering groups, such as $SU(5)$ ⁷, and a lower limit for monopole masses has been found⁸,

$$M > M_X/\alpha,$$

in the limit of vanishing potential in the Lagrangian, where M_X is the GUT mass scale. The GUT monopole which this theory predicts is thus extremely massive and could be produced only in the very early universe.

There are other phenomena that arise with GUT monopoles (nucleon decay catalysis, nucleon binding, dyons, etc.) that have not been considered because they are not particularly important to the detection efforts, which will be discussed later. For the detection of magnetic monopoles experimentally, the quantities of interest from the above calculations are the mass of the monopole and the magnetic charge. Most of the 'GUT' effects of the monopole are hidden in the short-range behavior and generally are too model-dependent to be useful as an experimental signature.

It is the superheavy mass and the Dirac magnetic charge of the monopole that are useful parameters in the design of experiments: the mass because

it indicates that GUT monopoles should be slow and yet highly penetrating, and the charge, indicating the ‘minimum’ interaction that one should expect from a monopole passing through a detector. When the model-dependent GUT effects are considered, they generally increase the detectability of the monopole.

1.2 Monopoles in Astrophysics

If one naively adds up all the matter that one sees in the universe, one finds that the ‘visible’ density is considerably less than that needed for the universe to be closed. However, it is known from cosmological evidence that the universe is near closure, and so it seems that a substantial fraction (0.5–0.9) of the density of the universe is unaccounted for; this is what is called the ‘missing’ or ‘dark’ matter.

The problems that arise when explaining the missing mass in terms of normal astronomical objects have led many to speculate that the missing mass is non-baryonic and interacts only weakly with normal matter. Remnant GUT monopoles from the early universe would be a constituent of non-baryonic missing mass, and so the limits on the amount of missing mass

can be applied to monopole fluxes.

1.2.1 The Parker Bound

The connection of GUT monopoles with astrophysics allowed Turner, Parker, and Bogdan⁹ to propose limits on the monopole flux based on the mass density of the universe and on the effect of monopoles on galactic magnetic fields. The mass density limits are based on two possibilities: the monopoles are distributed uniformly, or they are ‘clumped’ on a galactic scale.

Monopoles are accelerated by magnetic fields, and thus extract energy from the fields. The existence of galactic magnetic fields thus allows a limit to be set on the maximum flux of monopoles. This is lower than those obtained so far by direct searches for slow ($\lesssim 10^{-2} c$) monopoles and are useful for evaluating the plausible fluxes of GUT monopoles.

Figure 1.1 shows the astrophysical limits displayed as a function of monopole velocity for a monopole mass of 10^{16} GeV. The limits are conservative, erring on the side of being less restrictive. These limits are commonly known as the ‘Parker bound’ on monopole flux.

There have also been suggestions¹⁰ that the galactic magnetic field could

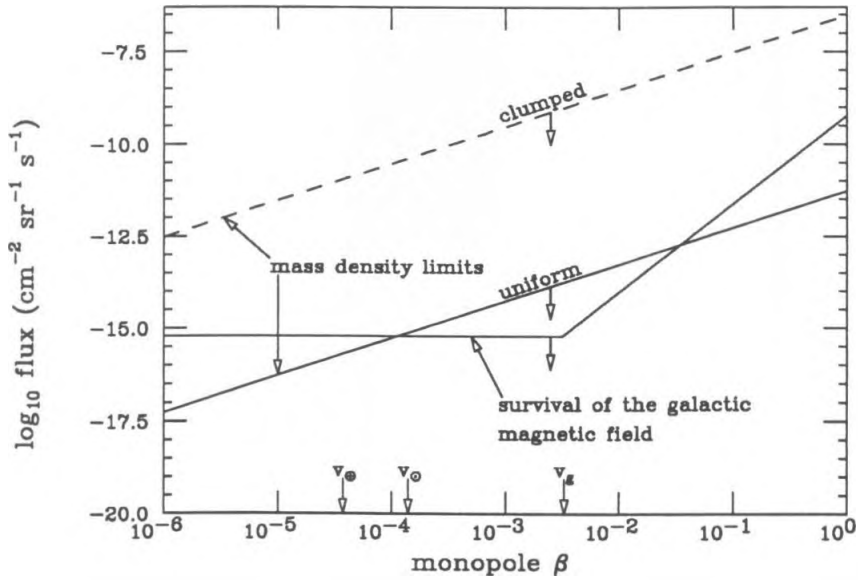


Figure 1.1: Astrophysical limits on GUT monopole flux, for a 10^{16} GeV monopole as a function of velocity. The escape velocities from the galaxy (v_g) the solar system (v_{\odot}) and the earth (v_{\oplus}) are shown. The 'uniform' and 'clumped' indicate the limits obtained for monopoles that are distributed uniformly, or clumped on a galactic scale.

be generated as a result of a monopole-plasma oscillation. This, in fact, gives a *lower* bound on the acceptable monopole flux, but direct monopole searches seem to rule out this possibility, and further calculations have shown this scenario to have stability problems.

There are stringent experimental limits on monopoles with velocities $\gtrsim 10^{-2} c$, primarily from pre-GUT monopole searches, which are not shown in the figure above. The velocities expected of GUT monopoles are lower than this, and so the Parker bound remains the best limit on the GUT monopole flux.

1.2.2 Monopole velocities

Monopole velocities in cosmic rays are estimated from astrophysical velocity scales. The lighter GUT monopoles can be accelerated to galactic escape velocities, and so would not clump on galactic scales. These ‘extragalactic’ monopoles would have velocities of $\sim 10^{-2} c$, while more massive monopoles bound gravitationally in galaxies would have velocities of order $10^{-3} c$.

It is possible that GUT monopoles could be gravitationally bound in the solar system, with even lower characteristic velocities. Monopoles bound

on this ‘local’ scale would show an greatly enhanced flux over galactic or extragalactic monopoles. The escape velocity from the earth, $3.7 \times 10^{-5} c$, is the minimum velocity expected of a monopole in cosmic rays, and so local monopoles should have velocities $\sim 10^{-4} c$.

Overall, it is most plausible that GUT monopoles will have characteristic velocities $\sim 10^{-3} c$ in cosmic rays, but lower velocities are still a possibility. This has been a motivation for the efforts made to extend detector response to lower velocities.

1.2.3 Discussion

The astrophysical limits are useful as a guide for what fluxes are plausible, which then indicates the size of detectors required to establish a monopole flux. The Parker bound indicates that detectors of ‘football field’ ($\sim 10^4 \text{ m}^2$) size are required if one hopes to see a flux in about a year.

The monopole velocities obtained from astrophysical arguments must be considered in the design of GUT monopole detectors, since it raises questions about the detectability of such slow particles in scintillator.

The expected velocities of GUT monopoles also invalidate many of the

previous monopole searches. The old pre-GUT monopole searches were generally looking for relatively light monopoles that would have velocities $\sim c$ because of acceleration by the galactic magnetic field. These searches for fast, highly ionizing monopoles are not applicable to GUT monopoles, primarily because of the difference in the expected monopole velocity.

1.3 Summary

I have indicated how monopoles arise in a natural way in GUTs and have shown how their fluxes are constrained by some astrophysical limits. Other experimental limits have not been cited explicitly, since they aren't very pertinent to the rest of this thesis, and astrophysical limits of a more speculative nature have been ignored here as well.

The GUT monopole has been shown to have some basic characteristics that are relevant to their detection: They have magnetic charge quantized in units of the Dirac charge; they should be supermassive ($\sim 10^{16}$ GeV) and hence highly penetrating; their velocities should be typically $v \sim 10^{-3} c$ from gravitational and magnetic acceleration, and their expected flux in cosmic rays should be very low.

A magnetic monopole detector should then look for lightly ionizing particles moving with a low, constant velocity. This signature is not unique to monopoles; supermassive particles with electric charge would produce a similar signal. This should not be considered to be a disadvantage, since the detection of a supermassive particle would be remarkable regardless of its nature.

Chapter 2

Monopole Scintillation

2.1 Introduction

One attractive possibility for large-scale GUT monopole detectors is the use of scintillation techniques, but first one must have some confidence that monopoles can be detected in such a fashion. This is particularly true for very slow GUT monopoles where the energy loss mechanism is not as well understood as it is for larger velocities.

In the discussion of the stopping power and scintillation yield of magnetic monopoles, it is convenient to have a standard scintillator with which to compare results. The plastic scintillator known as 'NE-110' is used here as

Table 2.1: NE-110 Properties Summary

Density	1.032 g/cm ³
Refractive Index	1.58
Light Output (ref. Anthracene)	60 %
Decay Constant (primary)	3.3 ns
Wavelength of Maximum Emission	434 nm
H/C atomic ratio	1.104
n_H	$5.24 \times 10^{22} \text{ cm}^{-3}$
n_C	$4.74 \times 10^{22} \text{ cm}^{-3}$

such a standard of comparison. The characteristics of NE-110 for detecting electrically charged particles are well known, and there are tabulated light yield figures that allow comparison to other commercial scintillators. Table 2.1 gives a summary of the physical properties of NE-110, as published by its manufacturer¹¹.

2.2 Monopole Stopping Power

The stopping power of magnetic monopoles in matter is the starting point for examining the detectability of monopoles in scintillator. In what follows I will use the notation S for the stopping power, defined as $-dE/dx$ of the projectile, and in general the quantity β refers to v/c of the projectile.

Stopping power calculations will be done for Dirac monopoles (charge $137e/2$), since this represents a minimum plausible monopole charge. Since the stopping powers increase as the square of the projectile charge, it is easy to scale the calculations here to other magnetic charges. Similarly, calculations of stopping power for electrically charged particles are done for protons, since they are of unit electric charge and may be considered to be 'infinitely massive' for many of the calculations.

There is an intimate connection between the calculation of stopping power for electrically and magnetically charged particles, and they will be shown together below. It should also be mentioned that there is a natural dichotomy between the high- and low- β regimes where the behavior of the stopping power is quite different. The dividing line between the regimes is the orbital velocity of electrons in the medium, since at projectile velocities less than

electron orbital velocities it is the electron orbital velocities that dominate the relative velocity of the system.

At even lower projectile velocities ($\beta \lesssim 10^{-4}$) the effects of ‘nuclear’ stopping dominate. Nuclear stopping comes from energy loss to atoms as a whole, rather than to individual electrons. It seems unlikely that this energy loss mechanism could contribute to scintillation, and so it will not be treated directly here. Empirical formulae that were used for nuclear stopping were taken from Wilson *et al.*¹², based on the work of Lindhard, Scharff, and Schiøtt¹³.

The ‘high- β ’ regime ($0.1 \lesssim \beta < 0.9$) is the most familiar for stopping power calculations, and so will be dealt with first. The stopping powers of relativistic projectiles ($\beta \gtrsim 0.9$) will not be examined since they are not pertinent to GUT monopoles.

2.2.1 Fast Projectiles

A natural starting point for stopping power calculations is the Bethe-Bloch equation^{14,15}, which describes the stopping power of electrically charged particles. Here I am ignoring some of the terms that are important for relativistic

particles, but are small corrections for the β range of interest.

$$S_e = \frac{4\pi N e^4 Z^2}{m c^2 \beta^2} \left[\ln \left(\frac{2 m c^2 \beta^2 \gamma^2}{I} \right) - \beta^2 \right], \quad (2.1)$$

where N is the number density of electrons in the medium, Z is the atomic number of the projectile, γ has the usual definition

$$\gamma = (1 - \beta^2)^{-1/2},$$

and m is the electron mass. Density and shell-correction terms have been ignored above, and I is the ionization energy of the medium.

An estimate of monopole stopping power comes from the examination of the induced electric field of a monopole of charge g , which can be used to make an 'effective' Z ,

$$e Z_{\text{eff}} = \beta g,$$

when compared to electrically charged projectiles. This procedure gives a monopole stopping power

$$S_m \sim \frac{4\pi N e^2 g^2}{m c^2} (\dots \text{other terms } \dots),$$

where the $1/\beta^2$ of the Bethe-Bloch equation has been cancelled. It would be mistaken to continue the analogy with electrically charged particles fur-

ther here, since the close scattering and large impact parameter effects of monopoles and electrically charged particles are quite different.

Ahlen^{15,16} calculated the monopole stopping power properly, using the Kazama, Yang, Goldhaber (KYG) calculation¹⁷ for the monopole-electron scattering cross section. The result for monopoles of $\beta \gtrsim 0.1$ is

$$S_m = \frac{4\pi N e^2 g^2}{m.c^2} \left[\ln \left(\frac{2mc^2 \beta^2 \gamma^2}{I_m} \right) + \frac{K(|g|)}{2} - \frac{1}{2} - B(|g|) \right], \quad (2.2)$$

where the density effect term in the original equation has been ignored. Here I_m is the counterpart of the ionization energy I above, and $K(|g|)$ and $B(|g|)$ are the KYG and Bloch correction terms, respectively. For a Dirac magnetic charge ($g = 137e/2$), the values of these two terms are $K \approx 0.41$ and $B \approx 0.25$. Both I and I_m may be calculated from the complex dielectric constant of the medium, and I_m may be approximated by I for NE-110 with only $\approx 5\%$ error.

2.2.2 Slow Projectiles

When monopole and charged particle stopping powers are examined at lower velocities, the assumptions used in the derivation of the equations above break down. It is then necessary to examine the atomic physics of energy

loss more carefully. A useful approximation is to treat the electrons of the medium as a degenerate Fermi gas with a Fermi velocity v_F . The crossover from the high- β to the low- β regimes is at $\beta c \sim v_F$; below this the relative velocity of the projectile-electron system comes primarily from the electron. The Fermi velocity is

$$v_F = \frac{\hbar}{m} (3\pi^2 N)^{1/3}, \quad (2.3)$$

which gives (using $N = 3.37 \times 10^{23}/\text{cm}^3$)

$$v_F = 8.3 \times 10^{-3} c$$

for NE-110. This value is actually somewhat of an overestimate for NE-110, since it assumes that all of the electrons in the solid are part of the Fermi gas, but it will be used here since it results in a lower bound on the stopping power of monopoles.

Lindhard¹⁸ obtained a stopping power for low-velocity, electrically charged projectiles using a Fermi gas model,

$$S_e = \frac{4\pi N e^4 Z^2 \beta c}{2m v_F^3} C_1, \quad (2.4)$$

which is a good fit to the experimental data. Note that the stopping power is now linear in projectile velocity, rather than the $1/\beta^2$ dependence of the

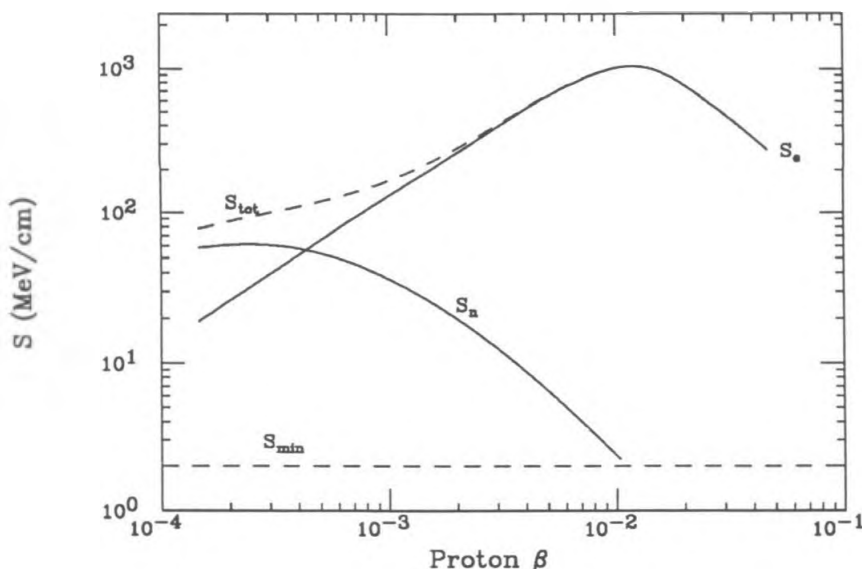


Figure 2.1: Stopping power of protons in NE-110. The electronic stopping power S_e comes from the equations in the text. The nuclear stopping power S_n is shown, and S_{tot} is the sum of the electronic and nuclear stopping power. S_{min} is the stopping power of a minimum-ionizing particle.

Bethe-Bloch equation. Lindhard's C_1 term depends on v_F , and may be evaluated numerically. This gives $C_1 = 0.423$ for a proton in NE-110; the stopping power obtained is

$$S_e = (127 \text{ GeV/cm}) \beta.$$

Figure 2.1 shows the stopping powers calculated for protons in NE-110. The nuclear stopping power is also shown, which was calculated from Wilson *et al.*¹², and S_{tot} is the sum of the nuclear and electronic stopping powers.

The stopping power for slow monopoles is a bit more complicated to

derive, but it has the same basic form as Eqn. 2.4. The induced electric field of the moving monopole is not screened by the atomic electrons, unlike that of an electrically charged projectile, but it is generally less efficient at transferring energy to the electrons. The interaction of the monopole's magnetic field with the magnetic moment of an orbital electron can also complicate the issue. This effect has been ignored, but it should be noted that it can increase the stopping power.

Ahlen and Kinoshita¹⁹ calculated the stopping power of monopoles at low velocities, using the same techniques as those used by Lindhard for slow electrically charged projectiles, and obtained

$$S_m = \frac{4\pi N e^2 g^2 \beta}{2m c v_F} \left[\ln \left(\frac{2v_F}{\alpha c} \right) - \frac{1}{2} \right]. \quad (2.5)$$

When evaluated for NE-110, this gives

$$S_m = (15.6 \text{ GeV/cm}) \beta$$

for a Dirac monopole. Figure 2.2 shows calculations of monopole stopping power in the the high- and low- β regimes for NE-110. Unlike the proton stopping powers, no interpolation has been done between the two regimes.

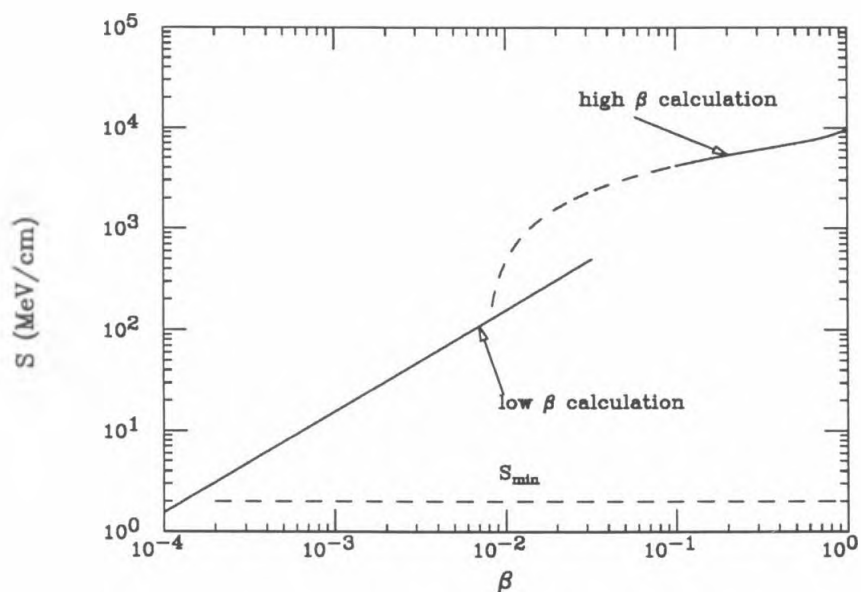


Figure 2.2: Dirac monopole stopping power in NE-110. The high- and low- β calculations are shown, with the value of the stopping power of a minimum-ionizing particle shown for comparison.

2.3 Scintillation Yield

The stopping power is informative, but it is the energy that is available as scintillation light (here denoted L) that produces the experimental signal, so one should ask how much energy dissipated by a monopole is going to result in scintillation light.

It is well known that scintillators saturate when the stopping power is large²⁰, becoming less efficient at converting the energy loss of a projectile into scintillation. Although there are more complex models for scintillator saturation, the data are well characterized by the expression for the scintillation efficiency

$$\frac{dL}{dE} = \left(\frac{dL}{dE} \right)_{max} (1 + B \cdot S_e)^{-1}, \quad (2.6)$$

with B an empirical constant in the range of 0.01 cm/MeV, and typical plastic scintillators (such as NE-110) having

$$\left(\frac{dL}{dE} \right)_{max} \approx 0.03 .$$

Scintillators require excitation above a threshold in order to produce scintillation. This has been modeled as a band gap in the electron Fermi gas, and should have an effect on the scintillation efficiency. The effect of a gap is

to produce a sharp threshold in β below which there is no scintillation light, because of the kinematics of a projectile-electron collision. The maximum energy which a slow massive particle can impart to an electron in an elastic collision is

$$\delta E_{max} = 2mv(v + v_F),$$

where the electron is originally on the Fermi surface.

Aromatic molecules, which are the basis of most organic scintillators, have a band gap which is roughly 5 eV. This would give a sharp cutoff in dL/dE and dL/dx at $\beta \approx 6 \times 10^{-4}$ for both monopoles and electrically charged projectiles. For example, NE-110 consists primarily of polyvinyltoluene (PVT), which has benzene rings connected to a long hydrocarbon 'backbone.' The lowest energy absorption feature (corresponding to an electronic transition) of PVT occurs at about 4.1 eV, and its absorption peak is at about 4.6 eV²¹. These are the transitions that are excited to produce scintillation light, and so a cutoff at $\beta = 4.6 \times 10^{-4}$ might be expected. Figure 2.3 shows the stopping power S_g , which goes to exciting a band gap, in this case assumed to be 5 eV.

Figure 2.4 shows the scintillation efficiency of protons in NE-110 as a

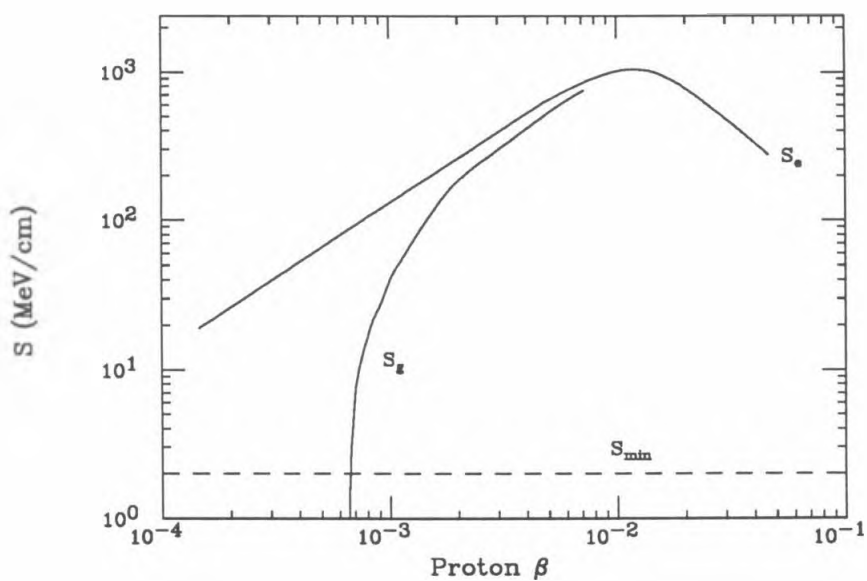


Figure 2.3: Stopping power to excite electrons across a 5 eV band gap S_g , estimated for NE-110 by Ahlen and Tarlé²². S_g is zero below $\beta \approx 6 \times 10^{-4}$ because of kinematic constraints.

function of energy. The data points are from Verbinski *et al.*²³, and the dL/dE curves were fitted to the data. In these fits it was found that a single value of B in Eqn. 2.6 would not fit the data well for the full energy range, and so a $C \cdot S_e^2$ term was included. The fitted value of C was small enough ($C \sim 10^{-6} \text{ cm}^2/\text{MeV}^2$) that it only affected the fit near the stopping power peak.

The extrapolation of the scintillation efficiency to lower β is shown, using the stopping power models with and without a 5 eV band gap. These extrapolations should be considered speculative, since the mechanisms for scintillator saturation by low-velocity particles have not been examined very much.

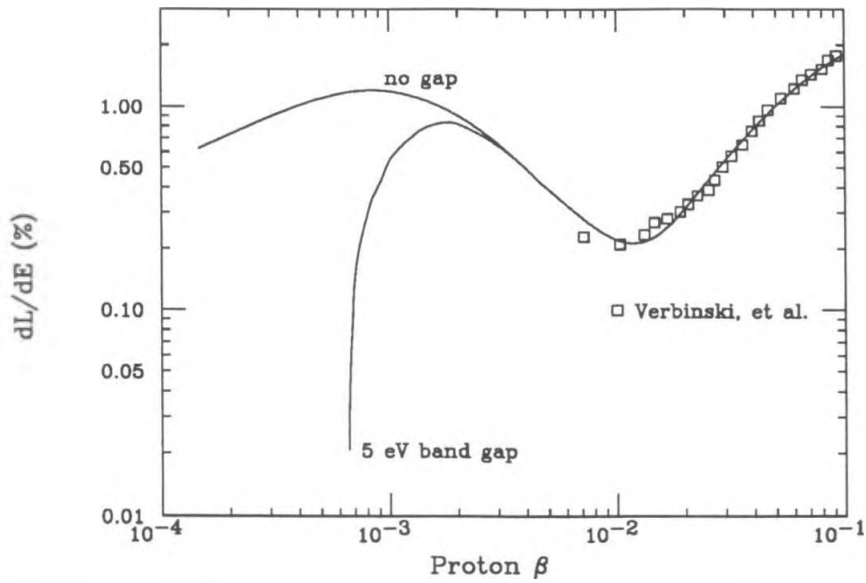


Figure 2.4: Scintillation efficiency for protons in NE-110, as a function of proton β . The data points have been fitted with an empirical dL/dE function and extrapolated to lower β . The 'band gap' curve was calculated using the stopping power S_g of a previous figure, and the 'no band gap' curve using S_e .

2.4 Other Energy Loss Terms

There were terms left out of the derivation of Eqn. 2.5, and in particular the effect of a monopole's magnetic field on the energy levels of an atom or molecule has been neglected. This effect has been calculated for hydrogen and helium²⁴, and it results in an enhanced light yield at low- β .

This level of detail in calculating monopole-atom interactions is only feasible for simple systems, which is why the calculations have been confined to hydrogen and helium atoms. It is possible that other atomic or molecular systems exhibit similar enhancements, but without a calculation of the effect one must rely on the more general stopping power estimates.

Monopoles should also lose energy through the effects of nuclear stopping power. There has been a calculation of this effect²⁵, but it becomes dominant only for very low monopole velocities ($\beta \lesssim 10^{-4}$), which are less plausible cosmologically. It does not seem likely that nuclear stopping could add to the detectability of monopoles in scintillator.

Coupling between electron magnetic moments and the magnetic field of a monopole has been ignored here. This subject has not been adequately treated in the literature, but it has been estimated¹⁹ that this coupling could

increase the stopping power of monopoles by as much as a factor of two.

2.5 Summary

Both electrically and magnetically charged particles have stopping powers that are proportional to velocity in the low- β regime. It is this velocity range that is of particular interest for GUT monopole searches in cosmic rays.

Taking the ratio of the monopole and charged particle stopping powers gives

$$\frac{S_m}{S_e} \approx 0.12 \left(\frac{g}{137e/2} \right)^2 \quad (2.7)$$

for low velocities in NE-110. This should be treated as a lower limit, since some possible effects mentioned above have been left out of the monopole stopping power.

It should be mentioned that the ratio S_m/S_e is sensitive to the value chosen for v_F . A calculation was made by Ahlen and Tarlé²² used $v_F = 6.9 \times 10^{-3} c$, based on an argument that four out of seven of the electrons in an aromatic hydrocarbon system could participate in low energy plasma excitations. They found $S_m/S_e \approx 0.25$ for Dirac monopoles in NE-110.

Perhaps a more realistic estimate of v_F is the velocity of a π electron in a benzene ring. A calculation using a simple molecular model gives $v_F = 2.9 \times 10^{-3} c$ for the Fermi velocity. The monopole stopping power calculation in Eqn. 2.5 must be modified somewhat, since the π electrons are spread over the entire molecule rather than a single atom. This affects only the logarithmic term, and the result is $S_m/S_e \approx 0.4$ for a Dirac monopole in NE-110.

The range of values for S_m/S_e just mentioned illustrates the bounds that may be safely placed on this ratio. Since it is primarily the minimum detectability of a monopole that is of interest in the design of a detector, the ratio $S_m/S_e = 0.12$ for a Dirac monopole in NE-110 will be used in further calculations.

Determination of the scintillation yield from monopoles requires a better understanding of the scintillation efficiency for slow particles. It is not clear that the simple models for scintillation efficiency remain valid at very low velocities, and some experimental guidance is required.

An examination of the scintillation efficiency of low-velocity protons can thus shed some light on low-velocity monopole scintillation. Since the stopping power of slow monopoles will be less than that of protons of the same

velocity, monopoles should not saturate scintillator to the same extent as protons. Thus, the scintillation efficiency of monopoles should be at least as large as that of protons, and in combination with the stopping power ratio provides a useful lower bound on the signal expected of a slow monopole in scintillator.

Chapter 3

Low β Scintillation Experiment

3.1 Description

An experiment was undertaken at the High Flux Beam Reactor (HFBR) at Brookhaven National Laboratory to measure the scintillation yield from low-beta protons. This experiment established that scintillation light is produced for protons with velocities $\approx 10^{-3} c$, and so monopoles should be detectable at velocities this low.

Figure 3.1 shows the general layout of the HFBR experiment. A filtered beam of neutrons was elastically scattered from protons in a plastic scintillator target and scintillation from the recoil protons detected with photomulti-

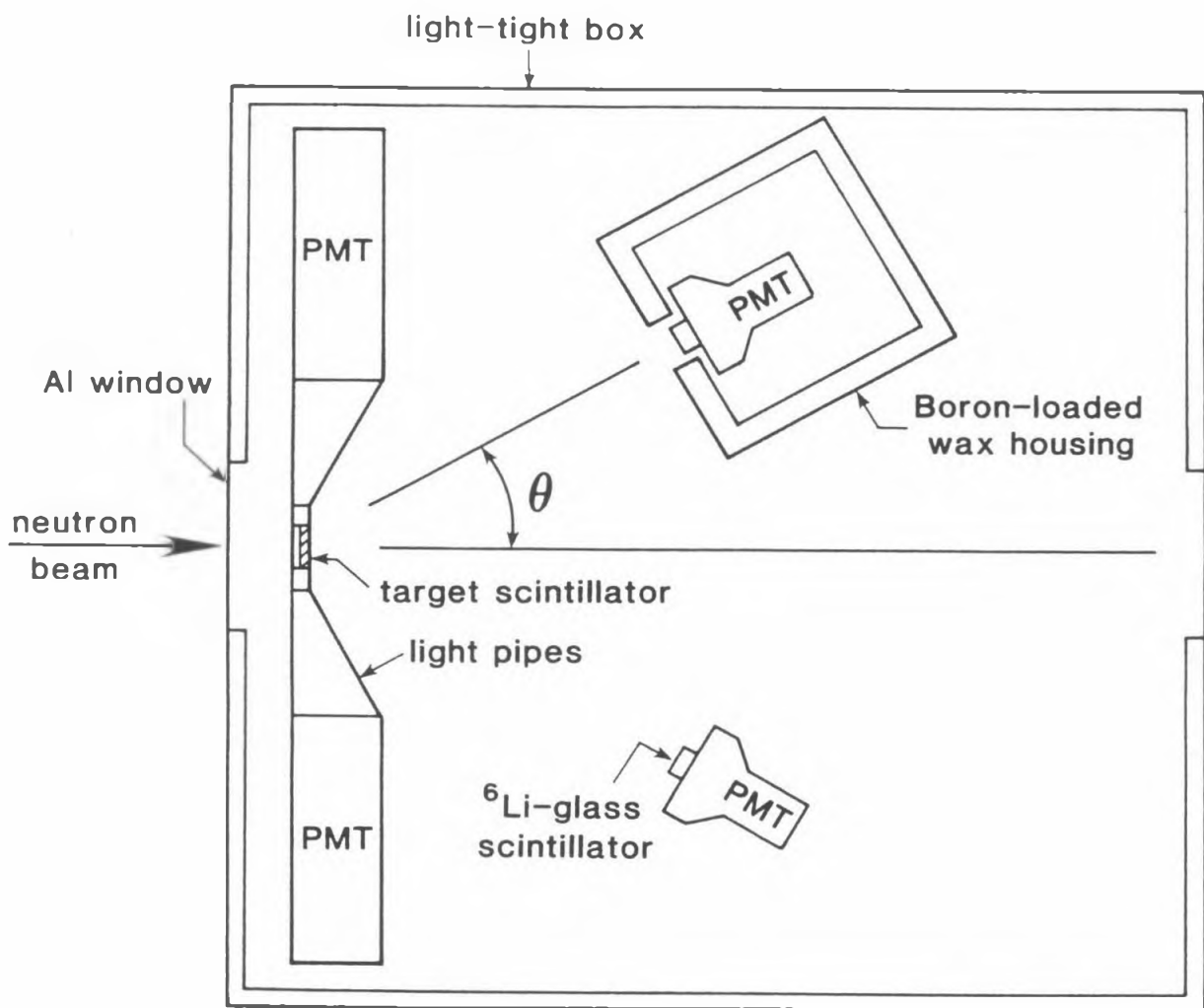


Figure 3.1: Layout of HFBR experiment.

pier tubes. The scattered neutrons were detected with ${}^6\text{Li}$ -glass scintillators and the relative timing between the scintillation in the target and the ${}^6\text{Li}$ -glass gave a time-of-flight signature. It has been noted that scintillators have surface effects²⁰ that reduce their scintillation efficiency for particles introduced at the surface of the scintillator. The use of recoil protons produced by np elastic scattering in the scintillator was motivated by the need to avoid such surface effects.

The angle of scattering determined the energy of the recoil protons by two body kinematics, with

$$E_p = E_0 \sin^2 \theta,$$

where E_0 is the neutron beam energy and θ is the scattering angle, and the neutron/proton mass difference is neglected (See Figure 3.2). The time-of-flight (TOF) between a signal in the target scintillator and in the ${}^6\text{Li}$ -glass scintillators was used to distinguish the signal from the background counts and contaminant energy groups in the neutron beam.

The apparatus was contained in a light-tight box to avoid the necessity of wrapping the scintillator target. Although the figure shows a ${}^6\text{Li}$ -glass scintillator in a boron-loaded wax enclosure, they were used in these enclosures

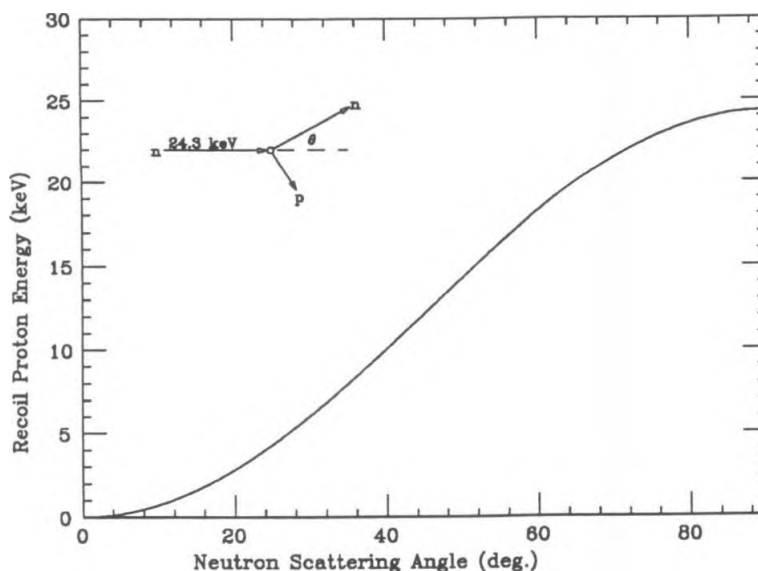


Figure 3.2: Energy of recoil proton with θ ; the neutron beam energy is 24.3 keV.

only during the last half of the experimental runs, including those taken at low scattering angles. The wax enclosures were used to reduce the thermal neutron background in the ${}^6\text{Li}$ -glass scintillators.

The scintillator target was viewed by a pair of RCA 8850 photomultiplier tubes. These photomultiplier tubes (PMTs) have a high-gain first stage, which made it possible to determine the number of photoelectrons in a signal by the pulse amplitude. The single- and double-photoelectron peaks were distinct and separable.

The ${}^6\text{Li}$ -glass scintillators were coupled with optical grease to RCA 4900

PMTs and covered with aluminum foil to improve the light collection efficiency and to isolate them optically from the scintillator target. The light collection from the ${}^6\text{Li}$ -glass scintillators was excellent, yielding large pulses from detected neutrons.

The neutron beam consisted of ‘filtered’ neutrons from the core of the HFBR. A quasi-monochromatic beam was produced by passing neutrons through an iron-aluminum filter. The ${}^{56}\text{Fe}$ $l = 0$ resonance at 27.70 keV gives an interference minimum in the total neutron cross section at about 24.3 keV, and a similar resonance in ${}^{27}\text{Al}$ results in a beam with about 2 keV FWHM and with contamination from other resonances $\lesssim 1\%$ of the 24.3 keV flux²⁶. Figure 3.3 shows the beam intensity (as a neutron time-of-flight plot) that was calculated for the beam filter, using tabulated cross sections for the ${}^{56}\text{Fe}$ and ${}^{27}\text{Al}$ resonances²⁷ and a $1/E$ epithermal neutron distribution. The energy spread of the 24.3 keV beam has little effect on the TOF measurements, since it is completely obscured by experimental timing resolutions.

Neutrons scattered in the scintillator target were detected with ${}^6\text{Li}$ -loaded glass scintillators. The ${}^6\text{Li}(n, {}^3\text{H}){}^4\text{He}$ reaction has a cross section²⁷

$$\sigma_c = (941 \pm 3 \text{ b}) \cdot \frac{v_t}{v}, \quad (3.1)$$

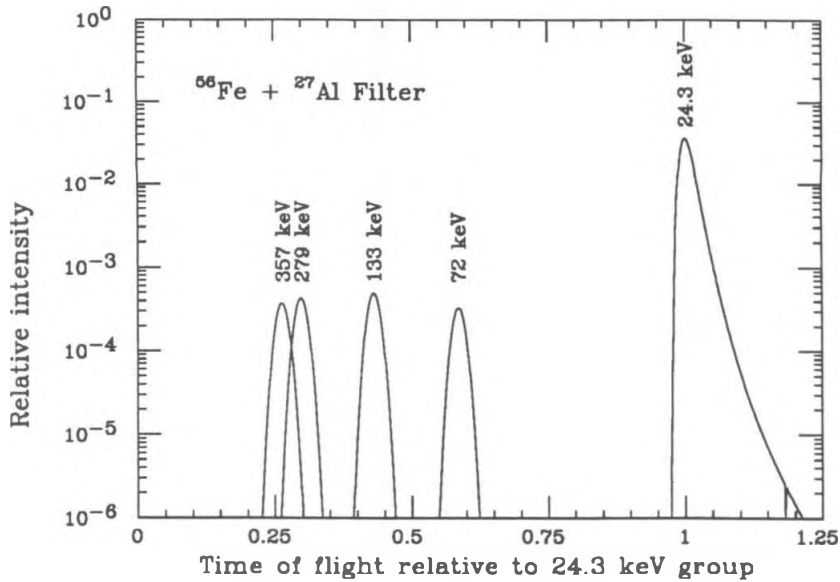


Figure 3.3: Calculated HFBR filtered neutron beam flux shown in a time-of-flight plot.

where v_t is the velocity of a thermal neutron (2200 m/s), and the reaction has $Q = 4.78$ MeV. The large amount of light from the ^6Li -glass scintillators allowed a tight discriminator window to be set on their signals, removing essentially all of the noise rate associated with the photomultiplier tubes. The singles rate from the ^6Li -glass scintillators was measured as ~ 75 Hz while running, from stray neutrons, γ s, and cosmic rays.

The experiment was triggered by a delayed coincidence of the target and ^6Li -glass scintillators in a coincidence gate of 400 ns. Figure 3.4 shows the electronics used. The PMT outputs from the target and ^6Li -glass scintillators

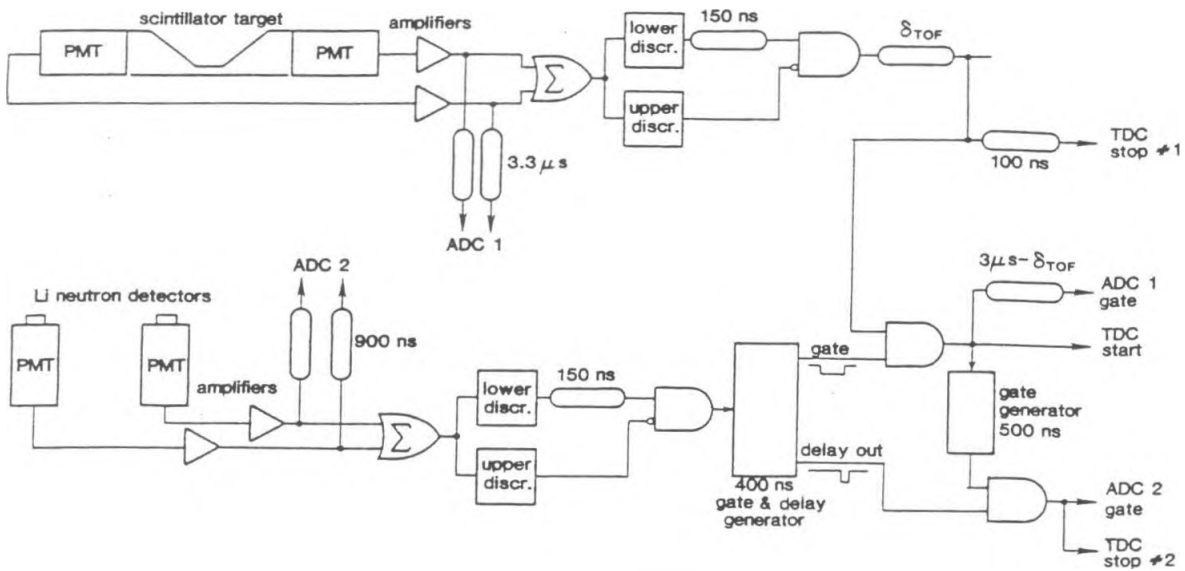


Figure 3.4: Trigger electronics for the low β scintillation experiment. A delayed coincidence of the target scintillator PMTs and the ${}^6\text{Li}$ -glass scintillator PMTs generates the trigger. The ADC gates are taken from the trigger and delayed so that they ‘track’ the PMT pulses. The neutron time-of-flight timing range could be selected by transferring cables between the cable delays δ_{TOF} and $3\mu\text{s} - \delta_{TOF}$, leaving the rest of the trigger timing invariant.

were amplified and fanned out to the acquisition electronics. The two target PMT signals were then summed and passed through upper- and lower-level discriminators, forming an acceptance window in pulse height. The ${}^6\text{Li}$ -glass scintillators were treated similarly, and the output used to trigger a gate generator that produced a 400 ns pulse.

The coincidence of the target scintillator PMT delayed by δ_{TOF} and the gate generator output produced a trigger. The trigger was delayed by $3\ \mu\text{s} - \delta_{TOF}$ and used to form an ADC gate for the target PMT signals. The delays were accomplished by shifting cables between δ_{TOF} and $3\ \mu\text{s} - \delta_{TOF}$, leaving the total delay in the ADC gate signal constant while changing the TOF timing range in steps of 200 ns. This allowed the ADC gate to ‘track’ the PMT pulses within the 400 ns coincidence window, regardless of the TOF timing offset.

The ADC gate for the ${}^6\text{Li}$ -glass scintillator signals was taken from the end of the gate generator signal, so that it was at a fixed delay from the ${}^6\text{Li}$ -glass signal, and would also ‘track’ the ${}^6\text{Li}$ -glass pulse. The pulses were sent to LeCroy 2259B ADCs and 2222 TDCs for digitization, and the data were read out and recorded by a LeCroy 3500 computer for offline analysis.

The pulse-shaping electronics used in this experiment gave Gaussian pulse

shapes. This provides optimal pulse height resolution, but since the timing was done with fixed voltage discriminators, there was a considerable amount of ‘time-walk’ in the signals from the discriminators.

The time-walk was corrected in the TOF spectra by fitting the time vs. amplitude scatterplot of events caused by γ s, which had good statistics and a large amplitude range, with a Gaussian peak shape scaled by threshold levels. This was found to be a good correction for all of the runs.

One effect of the time-walk was to cause some high-amplitude γ events to fall inside the delayed coincidence window, while the γ events with low pulse height were rejected. This helped to reduce the event rate of background events, while still leaving part of the γ peak to help define the timing. This peak is seen on the left side of the TOF histograms.

A total of 40 runs was taken over a period of five days, with scattering angles between 50° and 7.5° ; there was a total of 64.5 hours of live time with 5.9×10^4 events.

3.2 The Data

Figures 3.5 through 3.7 show the TOF histograms obtained for several of the

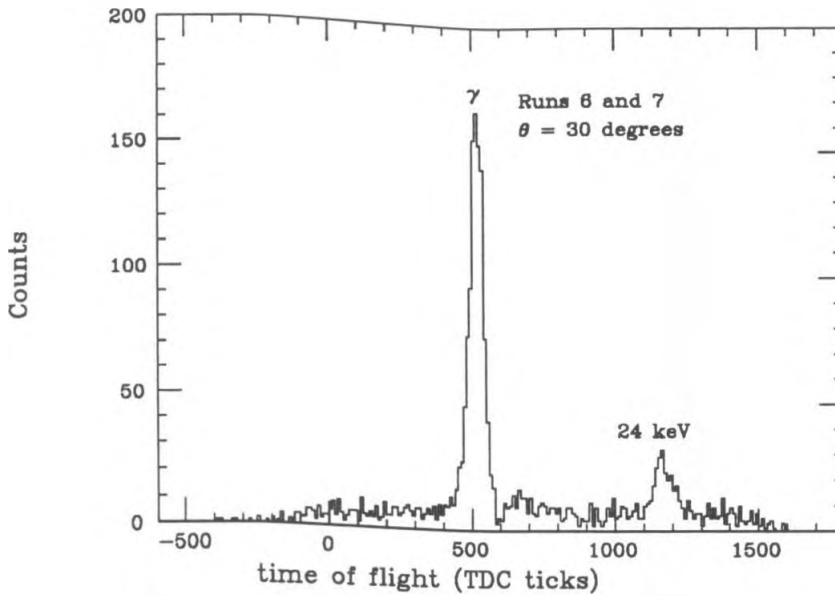


Figure 3.5: Neutron time-of-flight (TOF) histogram at $\theta = 30^\circ$. Each TDC tick is approximately 0.25 ns. The trigger timing puts the γ peak (TOF \approx 0) at about 500 TDC ticks. The peak from 24.3 keV neutron scattering is indicated.

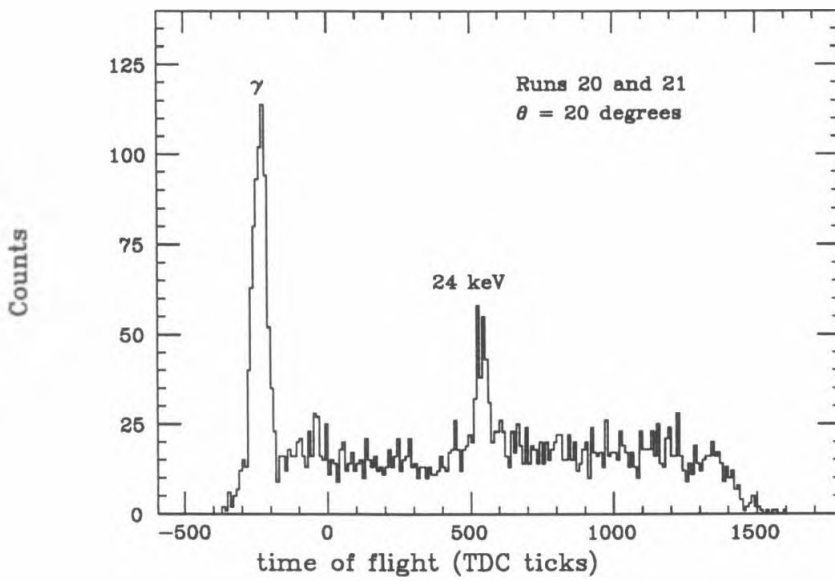


Figure 3.6: Neutron time-of-flight (TOF) histogram at $\theta = 20^\circ$. A different trigger timing offset has suppressed the γ peak, so that the 24.3 keV neutron scattering is more prominent.

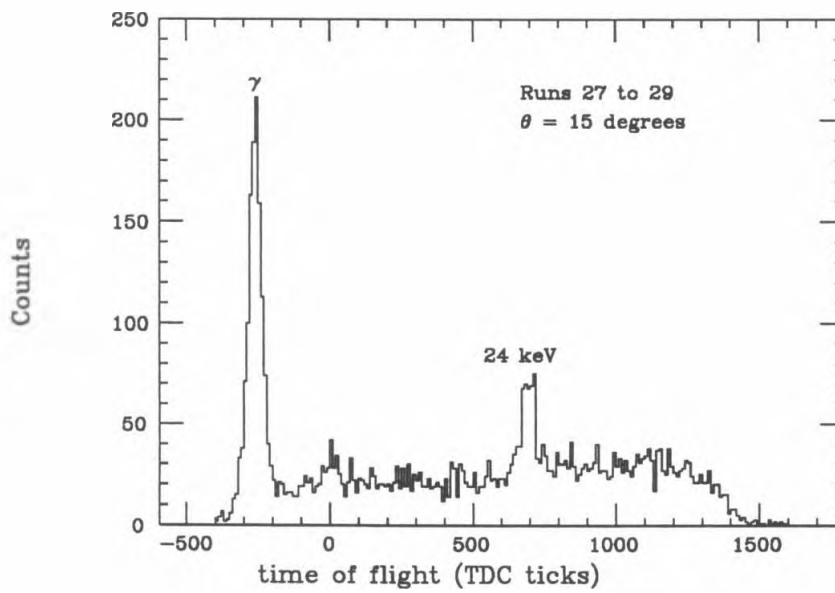


Figure 3.7: Neutron time-of-flight (TOF) histogram at $\theta = 15^\circ$. The TOF background is slightly higher at TOFs greater than that of the 24.3 keV neutron scattering peak.

runs. The time scale is relative to the TDC gate, after time-walk correction. There is typically a prominent γ peak on the low TOF side of the histogram, and a smaller peak from 24.3 keV np elastic scattering. The positions of both the γ and the TOF peak match the times expected, based on kinematics and the event delays.

Several of the histograms show a background level 'shift' between one side of the neutron scattering peak and the other, with a higher background level at larger TOFs. In general, the earlier runs with a 0.1 cm target and without a wax PMT enclosure show an overall flat background, while the later ones show the background shift. It was not possible to determine whether this was an effect of the thicker target or of the wax enclosure (or just more visible because of reduced background with a wax enclosure) since these changes were made at nearly the same time. The flat background was calculable within about 10% from measured noise rates, but 'shifted' background levels were several times higher than calculated, often with a $\gtrsim 5\sigma$ significance.

This background shift had to be accounted for in fitting the peaks, since one could not be certain of the background shape under the TOF peak. An examination of the backgrounds that could produce such a shift was thus necessary before the analysis could proceed.

3.3 Backgrounds

In the analysis of the data from this experiment, any events that were not the result of a single np elastic scattering of a 24.3 keV beam neutron in the target were considered to be background. This included multiple scattering, randoms, Compton scattering, etc. These will be detailed individually, with possible effects on the background shift noted.

A simple neutron scattering Monte Carlo was written to examine some of the issues with backgrounds and efficiencies. It will be referred to occasionally in connection with some of the more difficult background questions.

3.3.1 Randoms

The simplest background was from the random coincidence of singles from the target and ${}^6\text{Li}$ -glass scintillators. The neutron beam passing through the target scintillator generated a 5–10 kHz PMT singles rate from neutron scattering, which dominated the dark current of the PMTs. Singles from the ${}^6\text{Li}$ -glass scintillators were at a much lower rate (50–100 Hz) and were primarily caused by thermal or other stray neutrons.

Random coincidences of the singles then could not be distinguished from

scattering signals by their pulse heights, since the pulse heights in both the target and the ${}^6\text{Li}$ -glass scintillators were correct for neutron scattering events. The random coincidences occurred with equal probability throughout the coincidence window and could be taken as a flat background in TOF. A flat background was included in all of the TOF fits.

3.3.2 Multiple Scattering in the Target

Multiple scattering of neutrons in the target scintillator caused a background with a 'tail' on the long-TOF side of the single scattering peak. At larger scattering angles it was also possible for the multiple scattering to have shorter TOFs than the single scattering by scattering from both protons and carbon nuclei.

The background from multiple scattering decreases quickly with TOF. When it is adjusted for the ${}^6\text{Li}$ -glass target scintillator photoelectron efficiencies, then it becomes flat enough to be a plausible source for the 'background shift.' The multiple scattering TOF spectra obtained with the neutron Monte Carlo (and corrected for efficiencies) still had too few events at long TOFs to account completely for the background shift.

3.3.3 Compton Scattering and Capture Reactions

Compton scattering of γ contamination of the beam into the ${}^6\text{Li}$ -glass scintillator produces a 'prompt' (TOF ≈ 0) coincidence between the target and ${}^6\text{Li}$ -glass scintillators. Neutron capture in the target, dominated by the ${}^1\text{H}(n,\gamma){}^2\text{D}$ reaction ($Q=2.22$ MeV), also gives a prompt coincidence similar to Compton scattering.

Neutrons detected by the ${}^6\text{Li}$ -glass scintillators show a narrow peak in their pulse height distribution, while γ s have a much wider pulse height distribution, which is then cut off by the lower- and upper-level discriminators.

Most of the γ peak came from thermal neutron capture events in the scintillator or plastic light guides; the cross section for Compton scattering of γ s energetic enough to register in the ${}^6\text{Li}$ -glass scintillator drops rapidly with increasing scattering angle, yet the γ peak appears to be as evident at 45° as at 15° . An isotropic γ flux is typical of (n, γ) captures; however, the cross section for (n, γ) captures from the beam at 24.3 keV is much too small to account for the number of events because of the $1/v$ capture cross section. Thermal neutron contamination of the beam can account for much of the γ peak, since thermal neutrons have much higher capture cross sections.

These effects all produce prompt coincidences, which are easily separable from the neutron scattering signal. While they are a prominent feature of the TOF histograms, it seems unlikely that they could have a role in the background shift.

3.3.4 Neutron Scattering and Capture in Wax PMT Enclosures

Some Monte Carlo runs were made to determine the effect of neutrons scattering in the boron-loaded wax enclosures. While the exact geometry and acceptances were somewhat uncertain, the Monte Carlo did indicate that for typical situations, the flux of scattered neutrons would drop very rapidly with time (~ 3 decades in 100 ns) after the single scatter neutron TOF. This is only slightly affected by corrections for target and ${}^6\text{Li}$ -glass scintillator efficiencies. Since the observed TOF dependence of the background shows at most a small variation in background level, it seems unlikely that this could contribute much to the background.

Neutron (n, γ) reactions in the enclosures produce similar delayed TOF signatures, but it should be noted that the ${}^6\text{Li}$ -glass scintillator ADC distri-

butions of the post-TOF background rule out significant (n, γ) contribution to this background.

3.3.5 Trigger Electronics Effects

The possibility of an electronic effect, in which a noise pulse from the target scintillator could trigger the experiment before the recoil-proton signal arrived, was examined carefully, since the difference of background levels would then be an independent measure of the number of photoelectrons in the TOF peak. This would provide a useful check on the neutron beam intensity. This effect gives a flat post-TOF background, and so would make an attractive explanation of the background level shift.

The probability of a noise pulse ‘pre-empting’ the scintillation pulse was calculated, based on PMT singles rates and the coincidence gate width, to be about 3×10^{-3} . This is too small to be a significant effect in the background shift.

3.3.6 Discussion

The shape of the background is consistent with multiple scattering effects; however, the level is still higher than one would expect on the basis of Monte Carlo calculations.

After examining the hypotheses above, multiple scattering in the target still seemed the most likely cause of the raised background levels in the post-TOF signal. The other hypotheses have much larger discrepancies with the background rate or TOF distribution. While one hopes that such scattering calculations can be done accurately, perhaps it should not be so surprising that a discrepancy could exist between the calculated and observed multiple scattering backgrounds.

Because of this, it was necessary to scale the Monte Carlo TOF histograms for use in fitting the experimental data. The change in the fitted peak areas from this background scaling was comparable to statistical errors.

3.4 Analysis

The counting rate for coincidences due to neutron scattering in the scintillator target may be expressed as:

$$N = IT \mathcal{P}_S \epsilon_{\text{Li}} \epsilon_{PE}, \quad (3.2)$$

where N is the number of scattering events detected in time T , I is the neutron beam intensity, \mathcal{P}_S is the probability of scattering a beam neutron into a ${}^6\text{Li}$ -glass scintillator, ϵ_{Li} is the efficiency of the ${}^6\text{Li}$ -glass and ϵ_{PE} is the statistical photoelectron efficiency of the target scintillator signal. We may also express ϵ_{PE} as

$$\epsilon_{PE} = 1 - e^{-\mu},$$

using Poisson statistics, where μ is the mean number of photoelectrons per scatter. The object of most of the analysis will be to determine values of μ .

The calculation of the various terms of 3.2 will be dealt with separately below, and the determination of N was accomplished by fitting the TOF peaks.

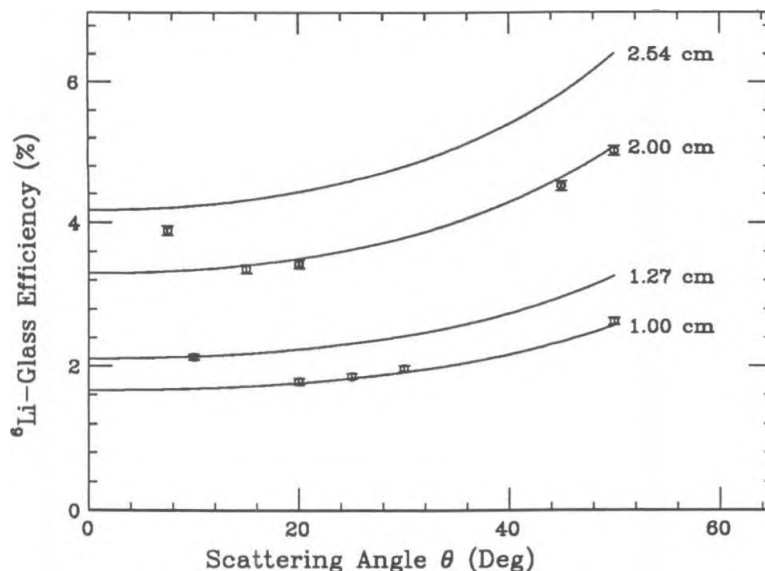


Figure 3.8: ${}^6\text{Li}$ -glass scintillator efficiency as a function of neutron scattering angle, labelled by the ${}^6\text{Li}$ -glass thickness. The data points were calculated by Monte Carlo for the actual ${}^6\text{Li}$ -glass configurations which that used in the experiment. Errors are statistical.

3.4.1 ${}^6\text{Li}$ -glass Scintillator Efficiency

The quantity ϵ_{Li} may be calculated from cross section data for ${}^6\text{Li}$ and the concentration of ${}^6\text{Li}$ in the ${}^6\text{Li}$ -glass scintillators:

$$\epsilon_{\text{Li}} = 1 - \exp(-\sigma_c n_{\text{Li}} \delta z), \quad (3.3)$$

where δz is the thickness of the ${}^6\text{Li}$ -glass, n_{Li} is the number density of ${}^6\text{Li}$, and σ_c is the capture cross section, which is given by Equation 3.1. Figure 3.8 shows curves of ϵ_{Li} calculated from the equation above. The ${}^6\text{Li}$ capture cross

section varies with the scattered neutron velocity, causing the variation in ϵ_{Li} with scattering angle.

Equation 3.3 is an approximation, since it takes into account only the effect of direct capture by the ${}^6\text{Li}$, not of scattering in the ${}^6\text{Li}$ -glass scintillator. Studies of these effects have been done previously²⁸, but the exact geometry of the ${}^6\text{Li}$ -glass plays an important role in the efficiency, and so Monte Carlo calculations were used to determine ϵ_{Li} .

The ${}^6\text{Li}$ -glass scintillator efficiencies were typically 2–5%, and there is good agreement between the efficiencies calculated with Eqn. 3.3 and those obtained by Monte Carlo. In most configurations the Monte Carlo efficiencies are slightly higher because of scattering effects in the ${}^6\text{Li}$ -glass. A few runs have a lower ϵ_{Li} from having the ${}^6\text{Li}$ -glass scintillators stacked parallel to the neutron direction of flight; any scattering tends to scatter neutrons out of the ${}^6\text{Li}$ -glass and reduce its efficiency (See Table 3.1). The expected systematic errors from the ${}^6\text{Li}$ -glass scintillator efficiency are on the order of 2–3%, and come from differences between the actual ${}^6\text{Li}$ -glass composition and the standard tabulated values¹¹.

Table 3.1: Comparison of calculated and Monte Carlo ϵ_{Li} values

Run(s)	θ	δz	ϵ_{Li} (Calc.)	ϵ_{Li} (M/C)
1	50°	1.00 cm	2.56×10^{-2}	$(2.63 \pm 0.05) \times 10^{-2}$
4, 8, 19-21	20	1.00	1.76×10^{-2}	$(1.79 \pm 0.04) \times 10^{-2}$
6, 7, 16	30	1.00	1.91×10^{-2}	$(1.97 \pm 0.04) \times 10^{-2}$
10-15	10	1.27	2.13×10^{-2}	$(2.13 \pm 0.04) \times 10^{-2}$
17, 18	25	1.00	1.82×10^{-2}	$(1.86 \pm 0.04) \times 10^{-2}$
22-24	20	2.00	3.49×10^{-2}	$(3.43 \pm 0.06) \times 10^{-2}$
25	50	2.00	5.06×10^{-2}	$(5.02 \pm 0.07) \times 10^{-2}$
26	45	2.00	4.61×10^{-2}	$(4.51 \pm 0.07) \times 10^{-2}$
27-29	15	2.00	3.39×10^{-2}	$(3.36 \pm 0.06) \times 10^{-2}$
30-33,35,38-40	7.5	2.54	4.18×10^{-2}	$(3.89 \pm 0.06) \times 10^{-2}$

3.4.2 Scattering Probability

An expression for \mathcal{P}_S in Eqn. 3.2 may be obtained in the thin-target approximation:

$$\mathcal{P}_S = \frac{d\sigma}{d\Omega}(\theta) \cdot \Delta\Omega \cdot n_H \cdot a, \quad (3.4)$$

where $d\sigma/d\Omega$ is the differential np scattering cross section, $\Delta\Omega$ is the solid angle subtended by the ${}^6\text{Li}$ -glass scintillators, n_H is the number density of hydrogen atoms in the target, and a is the target thickness. The equation above is valid only in the limit of thin targets, in which the probability of multiple scattering is small. In the case at hand, the probability of a neutron scattering in the target is ~ 0.2 , and so a better approximation to \mathcal{P}_S is required.

If the intensity remaining in the beam is denoted $\mathcal{I}(z)$, then we find that

$$\mathcal{I}(z) = \mathcal{I}_0 e^{-z/\lambda_1}, \quad (3.5)$$

where \mathcal{I}_0 is the neutron beam intensity with energy E_0 entering the target, and λ_1 is the attenuation length of the beam neutrons, which we may obtain from

$$\lambda_1 = \lambda(E_0), \quad (3.6)$$

with

$$\lambda(E) = \left[\sum_j \sigma_T^{(j)}(E)n_j \right]^{-1} \quad (3.7)$$

being the more general expression for attenuation length. Here, $\sigma_T^{(j)}(E)$ and n_j are the total neutron cross section (at energy E) and the number density of the j th species in the target, respectively. We examine the case of a neutron entering the target, scattering once from a hydrogen nucleus at a distance z into the target, and exiting with scattering angle θ without suffering further scattering. Let λ_2 be the attenuation length of 'scattered once' neutrons:

$$\lambda_2 = \lambda(E_n),$$

where E_n is the energy of the neutron after scattering once from hydrogen, given by

$$E_n = E_0 \cos^2 \theta .$$

The scattering cross sections $\sigma^{(j)}$ are mostly constant in the energy region of interest, the variation being dominated by the np cross section for which the theoretical cross section was used²⁹.

The outgoing intensity per unit solid angle for single scattering from hydrogen is given by

$$\frac{dI_k}{d\Omega}(\theta) = \int_0^a I_0 \exp(-z/\lambda_1) \cdot \frac{d\sigma^{(k)}}{d\Omega}(\theta)n_H \cdot \exp[-(a-z)/(\lambda_2 \cos \theta)] dz, \quad (3.8)$$

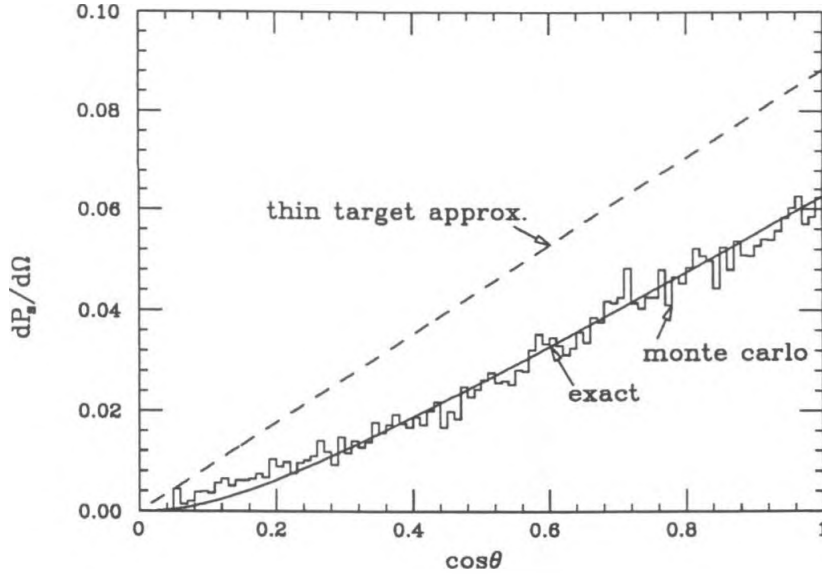


Figure 3.9: Comparison of scattering probability per unit solid angle for 0.3 cm of NE-110. The dashed line shows the thin-target approximation and the solid line the more exact calculation. The histogram was produced by a Monte Carlo.

where a is the thickness of the target. The integral yields

$$\mathcal{P}_S = \frac{d\sigma^{(H)}}{d\Omega} \cdot \Delta\Omega \cdot n_H \cdot e^{-a/\lambda_2} \cdot \lambda_T \left(e^{-a/\lambda_T} - 1 \right), \quad (3.9)$$

where

$$\lambda_T^{-1} = \lambda_2^{-1} \sec \theta - \lambda_1^{-1}.$$

Figure 3.9 shows the comparison of the thin-target calculation of \mathcal{P}_S (Eqn. 3.4) and the more exact calculation above and the data from the Monte Carlo obtained by selecting those events that scatter only once from hydrogen. The

thin-target approximation overestimates \mathcal{P}_S , while the more exact calculation and the Monte Carlo are in good agreement.

3.4.3 Fitting TOF Peaks

Runs at the same angle were combined for fitting whenever this was possible, as is reflected in Table 3.2. In some cases this was not possible because of differences in trigger timing or thresholds, and these runs were treated separately. The TOF peaks were fitted with Gaussians, using a combination of a flat overall background level and a background from multiple scattering that was obtained by Monte Carlo calculations.

The Monte Carlo used 3×10^7 beam neutrons and collected TOF histograms for a 0.3 cm target at the scattering angles and distances that corresponded to those of the HFBR runs. The runs with 0.1 cm targets had little or no significant background shift, and so a flat background was used in fitting them.

The Monte Carlo gave the number of multiple scattered neutrons in a 1° angular bin in scattering angle and at a particular TOF. These 'events' then had to be weighted by an estimated detection efficiency in order to

Table 3.2: HFBR Experiment Run Summary

Run(s)	T (min.)	θ	$\Delta\Omega$ (sr)	ϵ_{Li}	\mathcal{P}_S	Counts
1	59	50°	1.13×10^{-2}	2.63%	1.81×10^{-4}	268±23
4	128	20	4.06×10^{-3}	1.79	9.85×10^{-5}	68±18
6,7	64	30	1.13×10^{-2}	1.97	2.51×10^{-4}	156±18
8	33	20	1.63×10^{-2}	1.79	3.94×10^{-4}	70±12
10	21	10	1.28×10^{-2}	2.13	3.26×10^{-4}	33±10
11-13	176*	10	6.53×10^{-3}	2.13	1.66×10^{-4}	78±17
14,15	107	10	6.53×10^{-3}	2.13	1.66×10^{-4}	46±11
16	86	30	6.35×10^{-3}	1.97	1.41×10^{-4}	140±18
17,18	158	25	6.35×10^{-3}	1.86	1.48×10^{-4}	227±26
19	80	20	6.35×10^{-3}	1.79	1.54×10^{-4}	77±14
20,21	96*	20	6.35×10^{-3}	1.79	3.59×10^{-4}	198±24
22-24	112*	20	3.18×10^{-3}	3.43	1.79×10^{-4}	271±26
25	65	50	3.18×10^{-3}	5.02	1.12×10^{-4}	365±28
26	81	45	3.92×10^{-3}	4.51	1.56×10^{-4}	375±29
27-29	374	15	2.12×10^{-3}	3.36	1.24×10^{-4}	331±28
30-33,						
35,38-40	1383	7.5	2.84×10^{-3}	3.89	1.71×10^{-4}	598±45

* Estimated time, ± 2 min.

have a proper TOF distribution. The efficiency of detecting the event in the target scintillator was estimated as proportional to the total amount of proton recoil energy; carbon recoils were not considered as contributing to the detection efficiency. The events were also weighted inversely with the scattered neutron velocity to simulate the $1/v$ cross section of the ${}^6\text{Li}$ in the ${}^6\text{Li}$ -glass scintillators. The effect of the ${}^6\text{Li}$ -glass timing resolution was included by 'smearing' the background with a Gaussian of the same width as the TOF peak. This also smoothed the background to a more suitable shape for use in fitting.

The effects of the weighting were most noticeable in the long-TOF tail, where the weighting was necessary to obtain the observed flatness of the background. Near the TOF peak the variation of the weighting factors was small, and the shape of the multiple scattering background was not much affected; the fitted area under the TOF peak was thus mostly insensitive to the weighting. The resolution smearing affected the fitted areas very slightly; the change was typically $\lesssim 1\%$ of the fitted area, amounting to a $\approx 0.1\sigma$ difference in area.

The multiple scattering background was aligned with the TOF peak and scaled to fit the TOF distributions. The scaling factor and the flat back-

ground level were the only parameters used for background fitting. This procedure was found to fit the data quite well (See Figure 3.10) and was a definite improvement over more naive backgrounds. This background was also used for the fitting of single and double photoelectron TOF distributions.

3.4.4 Neutron Beam Intensity

The neutron beam intensity was the major unknown of this experiment and was the largest source of systematic error. Fortunately, the beam intensity was found to be constant, as measured by ${}^6\text{Li}$ -glass scintillator monitors that were placed in the beam on several occasions. The beam monitor was not particularly helpful for determining the actual beam intensity, since thermal neutron contamination of the beam has $\epsilon_{\text{Li}} \approx 1$, while the 24.3 keV beam has $\epsilon_{\text{Li}} \approx 1.7 \times 10^{-2}$. Thus, a small thermal contamination can seriously bias any intensity measurement, but the constancy of the monitor rates to within about 1%, together with other flux measurements, indicated that the 24.3 keV beam intensity was constant at the few percent level. This is much less than the systematic errors inherent in the beam intensity determination.

The beam intensity was obtained by determining the mean number of

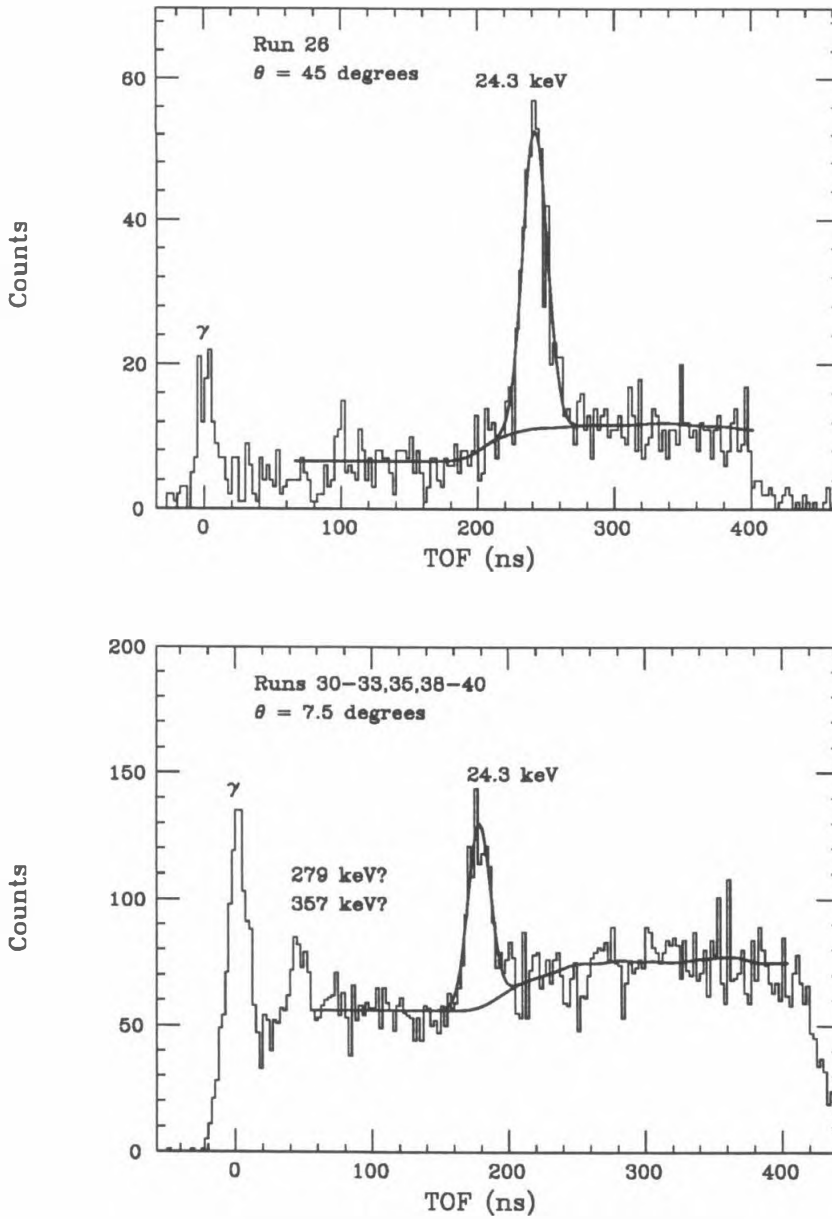


Figure 3.10: Fits of runs at 45° and 7.5° . The background used in the fits is indicated.

photoelectrons μ in the TOF peak, using the ratio of the number of double to single photoelectron events

$$\mu = 2 \frac{N_2}{N_1}$$

from Poisson statistics. This then gives an estimate for ϵ_{PE} which, when combined with the TOF peak area and other calculated factors, gives a value for the beam intensity. The determination of the number of photoelectrons was done with the data from runs at 45° and 50° where μ was relatively large; this reduces the relative error in ϵ_{PE} , since the propagation of the error in μ to ϵ_{PE} is given by (here σ^2 is the variance):

$$\sigma_\epsilon^2 = e^{-2\mu} \sigma_\mu^2 .$$

The photomultipliers had good separation of single and double photoelectron signals, but even in the 45° and 50° runs the number of photoelectrons was only ~ 0.5 . Care was required in separating the single and double photoelectron events, so that the more numerous single photoelectron events wouldn't contaminate the double photoelectron events.

The single and double photoelectron TOF distributions were obtained by making a pulse-height cut. They were then fitted separately using the backgrounds mentioned previously. The double photoelectron events obtained in

this way have some events with three or more photoelectrons; this can be accounted for in the calculation of μ , but is a small effect compared to the other errors.

The single and double photoelectron events were then corrected for the presence of the cut according to

$$\begin{bmatrix} N'_1 \\ N'_2 \end{bmatrix} = \begin{bmatrix} f_1 & 1 - f_2 \\ 1 - f_1 & f_2 \end{bmatrix} \begin{bmatrix} N_1 \\ N_2 \end{bmatrix}, \quad (3.10)$$

where f_1 and f_2 are the fractions of 1 and 2 photoelectron events that are on the correct side of the cut, respectively, the N'_j are the measured number of events on each side of the cut, and the N_j are the true values.

The f_2 factor was determined by examining the effect of the cut on events that were recorded in both target scintillator PMTs and hence were a 'pure' sample of double photoelectron events. A histogram of a single photoelectron ADC distribution was made after the experiment, and it was found to be Gaussian for pulse heights greater than the 1 photoelectron peak. Scaling this to the observed pulse height distributions (which contained both single and double photoelectron events) indicated approximate values for f_1 . The cuts were placed $\approx 3\sigma$ above the 1 photoelectron peak to minimize the contamination of the doubles by the more numerous singles, and the error in f_1

Table 3.3: Calculated Neutron Beam Intensities

Run	θ	$1 - f_1$	f_2	μ	\mathcal{I}_{calc}
1	50°	2×10^{-3}	0.77 ± 0.19	0.52 ± 0.26	(39. \pm 15.) kHz
25	50	4×10^{-3}	0.77 ± 0.13	0.63 ± 0.24	(36. \pm 10.)
26	45	3×10^{-3}	0.85 ± 0.16	0.37 ± 0.15	(36. \pm 12.)
Average					(36.5 \pm 7) kHz

was estimated (conservatively) as $\lesssim 0.01$.

Table 3.3 shows the beam intensities that were calculated by this procedure. The errors given are statistical; it is possible that systematic errors dominate, but they could not be estimated from the available data. The beam intensity calculation includes the effects of errors in f_1 and f_2 .

For convenience, the statistical error in this determination of \mathcal{I} will be subsumed into the systematic error, and the value

$$\mathcal{I} = 36.5 \text{ kHz}$$

used for the remainder of this analysis.

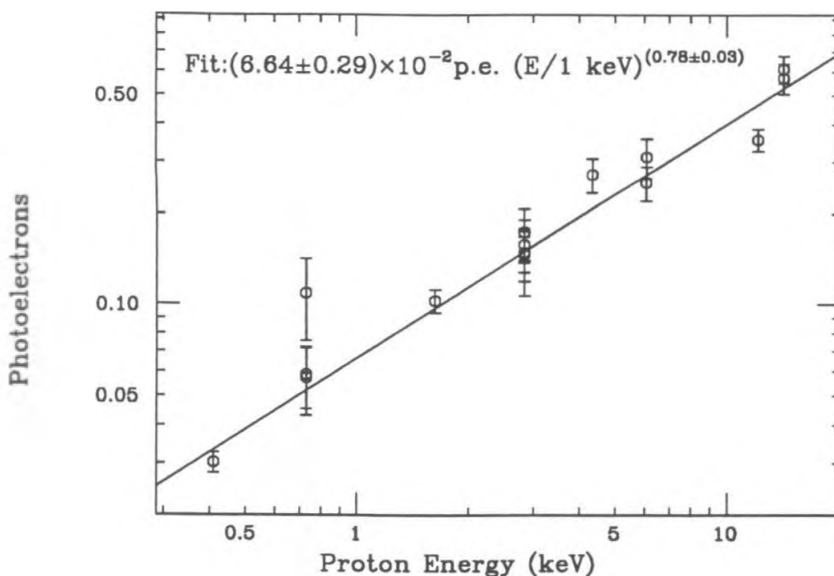


Figure 3.11: Calculated photoelectron yield as a function of proton recoil energy.

3.4.5 Light Yields

With a determination of the beam intensity the ϵ_{PE} values may now be calculated, and from them the average number of photoelectrons μ for a proton recoil may be obtained. Table 3.4 shows the calculated ϵ_{PE} 's and μ 's, where the errors are the statistical errors and do not include any error from \mathcal{I} .

Figure 3.11 shows the photoelectron yields plotted against recoil proton energy. There is some scatter, and it looks as though run 26 may have some systematic deviation, but the overall fit looks quite encouraging. At this

Table 3.4: HFBR Light Yields

Run(s)	θ	E_p (keV)	ϵ_{PE}	μ
1	50°	14.3	$(4.36 \pm 0.44) \times 10^{-1}$	$(5.72 \pm 0.66) \times 10^{-1}$
4	20	2.84	$(1.39 \pm 0.36) \times 10^{-1}$	$(1.49 \pm 0.42) \times 10^{-1}$
6, 7	30	6.08	$(2.26 \pm 0.26) \times 10^{-1}$	$(2.56 \pm 0.34) \times 10^{-1}$
8	20	2.84	$(1.37 \pm 0.24) \times 10^{-1}$	$(1.47 \pm 0.28) \times 10^{-1}$
10	10	0.733	$(1.03 \pm 0.30) \times 10^{-1}$	$(1.09 \pm 0.33) \times 10^{-1}$
11–13	10	0.733	$(5.70 \pm 1.26) \times 10^{-2}$	$(5.87 \pm 1.34) \times 10^{-2}$
14, 15	10	0.733	$(5.56 \pm 1.34) \times 10^{-2}$	$(5.73 \pm 1.42) \times 10^{-2}$
16	30	6.08	$(2.68 \pm 0.34) \times 10^{-1}$	$(3.12 \pm 0.47) \times 10^{-1}$
17, 18	25	4.34	$(2.38 \pm 0.27) \times 10^{-1}$	$(2.72 \pm 0.36) \times 10^{-1}$
19	20	2.84	$(1.60 \pm 0.29) \times 10^{-1}$	$(1.74 \pm 0.34) \times 10^{-1}$
20, 21	20	2.84	$(1.46 \pm 0.18) \times 10^{-1}$	$(1.58 \pm 0.21) \times 10^{-1}$
22–24	20	2.84	$(1.37 \pm 0.17) \times 10^{-1}$	$(1.48 \pm 0.20) \times 10^{-1}$
25	50	14.3	$(4.59 \pm 0.35) \times 10^{-1}$	$(6.14 \pm 0.65) \times 10^{-1}$
26	45	12.2	$(3.00 \pm 0.21) \times 10^{-1}$	$(3.56 \pm 0.30) \times 10^{-1}$
27–29	15	1.63	$(9.81 \pm 0.84) \times 10^{-2}$	$(1.03 \pm 0.93) \times 10^{-1}$
30–33,				
35, 38–40	7.5	0.414	$(2.98 \pm 0.22) \times 10^{-2}$	$(3.02 \pm 0.23) \times 10^{-2}$

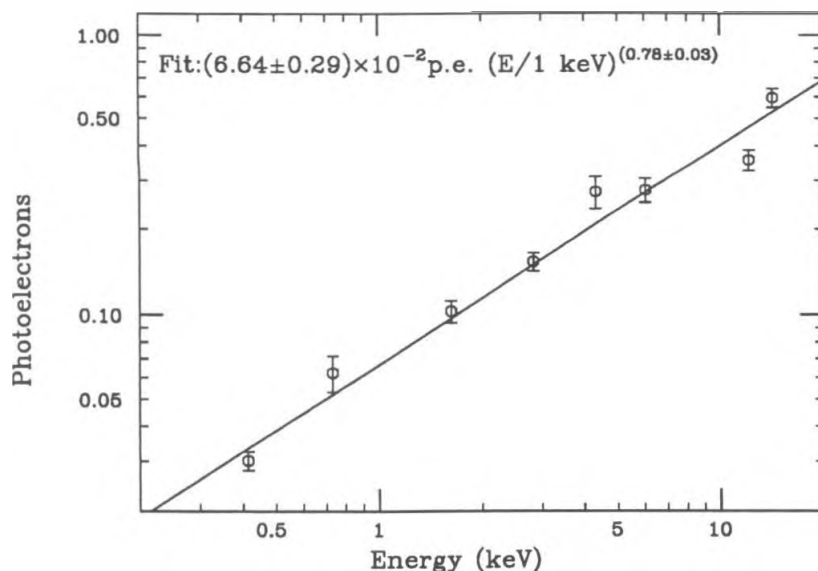


Figure 3.12: Averaged photoelectron yield as a function of proton recoil energy for all runs. A least-squares fit to the data is shown.

point it is useful to start combining runs at the same angle by averaging their ϵ_{PE} values. Table 3.5 and Fig. 3.12 show the averages that were obtained for each angle. A least-squares fit gives

$$\mu(E) = (6.64 \pm 0.29) \times 10^{-2} \text{ photoelectrons} \cdot \left(\frac{E}{1 \text{ keV}} \right)^{0.78 \pm 0.03}, \quad (3.11)$$

where the errors are statistical, and doesn't include errors from the beam intensity.

Before comparing with other experiments, it is necessary to normalize the data to a standard light level. This normalization was accomplished by measuring the number of photoelectrons in the sum of both target scintillator

Table 3.5: HFBR Light Yield Averages by Scattering Angle

θ	E_p	Avg. ϵ_{PE}	μ
7.5°	0.414 keV	$(2.98 \pm 0.22) \times 10^{-2}$	$(3.02 \pm 0.23) \times 10^{-2}$
10	0.733	$(6.05 \pm 0.88) \times 10^{-2}$	$(6.24 \pm 0.93) \times 10^{-2}$
15	1.63	$(9.81 \pm 0.84) \times 10^{-2}$	$(1.03 \pm 0.93) \times 10^{-1}$
20	2.84	$(1.43 \pm 0.10) \times 10^{-1}$	$(1.54 \pm 0.11) \times 10^{-1}$
25	4.34	$(2.38 \pm 0.27) \times 10^{-1}$	$(2.72 \pm 0.36) \times 10^{-1}$
30	6.08	$(2.41 \pm 0.21) \times 10^{-1}$	$(2.76 \pm 0.27) \times 10^{-1}$
45	12.2	$(3.00 \pm 0.21) \times 10^{-1}$	$(3.56 \pm 0.30) \times 10^{-1}$
50	14.3	$(4.48 \pm 0.26) \times 10^{-1}$	$(5.94 \pm 0.46) \times 10^{-1}$

PMTs when an ^{241}Am source was placed on the target scintillator. This measurement was done for both the 0.1 cm and the 0.3 cm NE-110 targets, and yielded 107 ± 5 photoelectrons for the 5.48 MeV α . The difference between the light yield of the two targets was less than the estimated error in the measurements, and so the two sets of data were combined without a relative adjustment.

The ^{241}Am calibration could then be used to normalize to previous proton light yield ($L_p(E)$) measurements, since a set of standardized $L_\alpha(E)$ and $L_p(E)$ measurements were available in the literature²³. The quoted error for $L_\alpha(E)$ was 10%, and that of $L_p(E)$ was 2%. It should be noted that the L_p and L_α measurements were made using NE-213, but it has been shown³⁰ that the light output from NE-213 is identical to that from NE-110 over a range of 24 keV–20 MeV. The normalization with $L_\alpha(E)$ gives a light yield of 116 ± 13 eV/photoelectron, where the error contributes to the systematic error of light level normalization.

Figure 3.13 shows the comparison of this experiment to the $L_p(E)$ curve derived from previous experiments at higher energies^{23,30,31}. It appears that the data points obtained here are offset from the previous measurements by about 15%, an offset is perhaps not so surprising, given the difficulties with

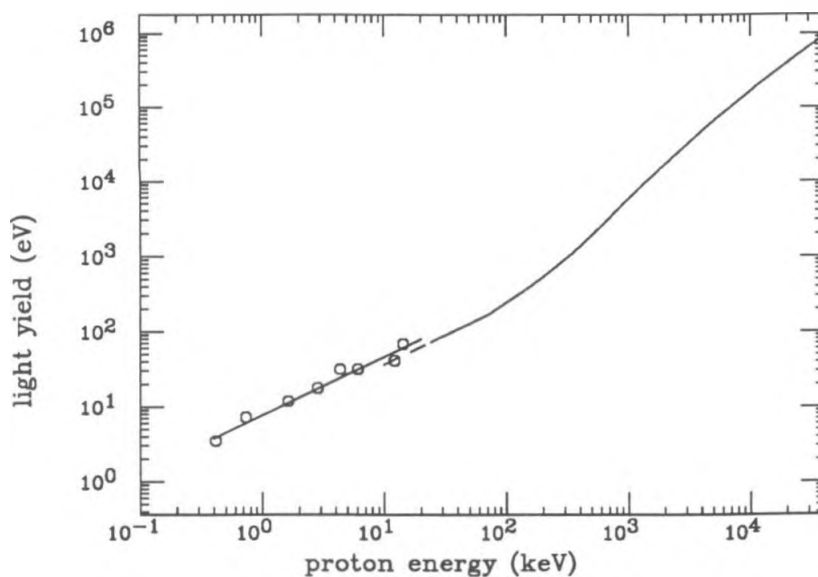


Figure 3.13: Light yield of recoil protons as function of energy. The data points are from this experiment, with a least-squares fit.

systematics in the neutron flux determination and in finding absolute light levels and efficiencies.

3.4.6 Discussion

A previously published analysis² shows a curve that is 20% below the level of the the higher energy data, but lacks a number of the points that were used here. The difference in slope (0.86 as opposed to 0.78 here) can be attributed the method in which the scattering probabilities and ⁶Li-glass efficiencies were calculated, but the two slopes are not inconsistent with each

other when the statistical and systematic errors are considered.

Scintillation Efficiency

The normalization of the response curve is less important than its shape and slope. Just the fact that the trend of the light output as a function of proton energy is continuing is important in evaluating mechanisms of scintillation at low velocity.

The scintillation efficiency may be estimated from the slope of the fit obtained above and compared with the models for scintillation efficiency as a function of dE/dx . An 'average' scintillation efficiency L/E is also useful as an estimate of the scintillation efficiency for proton velocities less than those measured in this experiment. Figure 3.14 shows the fit of the data from this experiment,

$$\frac{dL}{dE} = (6.01 \pm 0.35) \times 10^{-3} \cdot \left(\frac{E}{1 \text{ keV}} \right)^{-0.22 \pm 0.03}$$

and scintillation efficiencies derived from higher energy data.

A more useful form of the scintillation efficiency fit above is in terms of proton β , since this can be used as an estimate of monopole scintillation

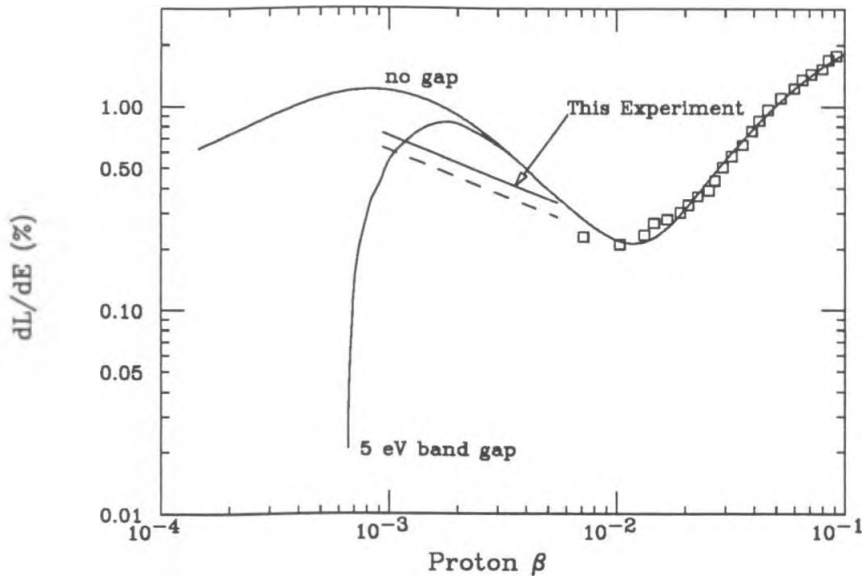


Figure 3.14: Scintillation efficiency calculated from light yield fit, compared with calculations of the previous chapter and the data of Verbinski *et al.*²³ The dashed line shows the scintillation efficiency from the fit when the light yield is matched to the data of Verbinski *et al.*

efficiency.

$$\frac{dL}{dE} = (7.1 \pm 0.4) \times 10^{-3} \cdot \left(\frac{\beta}{10^{-3}} \right)^{-0.44 \pm 0.06}$$

In fact, the scintillation yield at 414 eV ($\theta = 7.5^\circ$) gives a minimum scintillation efficiency (L/E) of $(8.5 \pm 0.6) \times 10^{-3}$.

The dL/dE curves show calculations based on a 5 eV band gap in the scintillator and with no gap. If such a gap is present in NE-110, then there would be no contribution to L from energies below the kinematic cutoff. One then expects L/E to decrease sharply as the proton energy approaches the cutoff. This experiment found no evidence for such a decrease in L/E or in scintillation efficiency with decreasing proton energy.

A kinematic cutoff in scintillation efficiency is ruled out for proton energies greater than 400 eV and seems unlikely for energies greater than ≈ 200 eV, which corresponds to a band gap of 5.5 eV. Since the most probable value of a band gap is 4–5 eV, this experiment must leave the question of the existence of such a band gap open.

Other possible effects

Scintillation from carbon recoils in the scintillator was not observed in this experiment, even at the larger scattering angles where it would be most

noticeable. Because of the low velocity of carbon recoils, it was expected that no signal would be seen corresponding to neutron scattering from carbon; previous studies²³ have reported carbon recoils at higher energies and we may take their data as indicative.

Direct neutron-electron scattering was also not considered as an effect in this experiment as the cross sections are much too small to produce an observable effect. Magnetic scattering of neutrons from electrons was also expected to have no effect on this experiment, since it depends on coherent scattering from unpaired electrons. Coherent scattering is negligible at 24.3 keV, and the covalent bonds in a plastic scintillator should have no such unpaired electrons.

3.5 Conclusions

The primary result of the HFBR experiment was the detection of scintillation light at $\beta = 9.4 \times 10^{-4}$. This is a strong indication that magnetic monopoles will also be detectable at low velocities, and that the light yield for a typical counter thickness (~ 10 cm) is large enough to make detection practical. Using the Lindhard stopping power for protons S_e , and the results from the

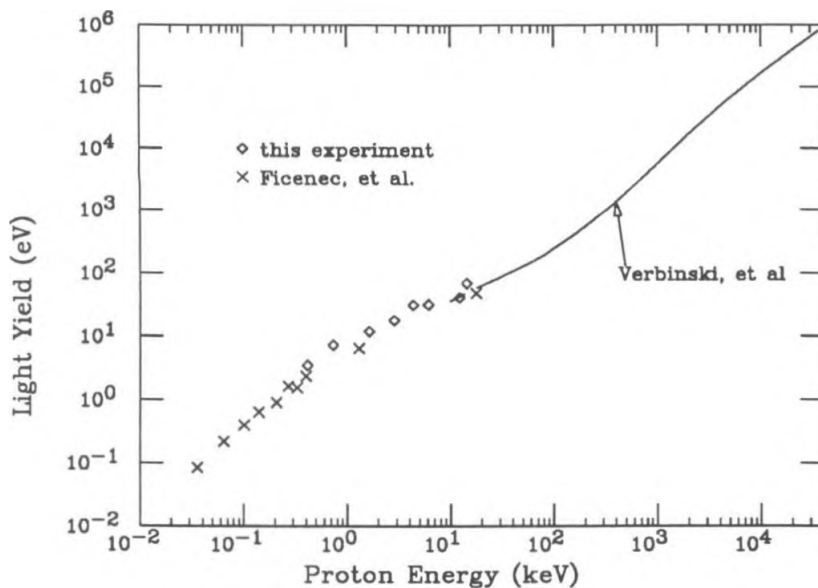


Figure 3.15: Results of this experiment, and more recent low β scintillation results.

previous section for a $\beta = 10^{-3}$ monopole:

$$\begin{aligned}
 N_\gamma &\approx S_e(\beta = 10^{-3}) \frac{S_m dL}{S_e dE} \frac{10 \text{ cm}}{3 \text{ eV}} \\
 &= 3.6 \times 10^5 \text{ photons,}
 \end{aligned}$$

which should be enough for detection.

There has been a further low-velocity scintillation experiment³ since this experiment, extending to velocities as low as $\beta \approx 2.5 \times 10^{-4}$, with scintillation observed even at these low velocities. Figure 3.15 shows the results of this experiment with the higher-energy light yield data, and the newer results. It can be seen that there is no sudden drop in the light yield that would imply

a threshold.

If there is a band gap, these recent results indicate that it must be less than ≈ 2.5 eV, using the calculations of the previous chapter. Since the spectrographic evidence indicates 4–4.5 eV required to excite scintillation, one must conclude that the scintillation mechanism is not as simple as the band-gap model implies.

A rough fit of the newer data gives

$$\frac{dL}{dE} \approx (1.0 \times 10^{-2}) \left(\frac{\beta}{10^{-3}} \right)^{0.85}$$

for $1.5 \times 10^{-3} > \beta > 2.5 \times 10^{-4}$. No errors are given with this fit, since they could not be calculated from the available data.

Further development will be required before the mechanism of low-velocity scintillation is fully understood, but the implication for the detection of monopoles is clear. Slow monopoles should produce detectable scintillation in the velocity range expected from cosmological arguments, and at light levels that are experimentally useful.

Chapter 4

The Caltech Prototype

Monopole Detector

4.1 Introduction

Although the astrophysical limits indicate that very large detectors are required to achieve significant monopole flux limits, it was desirable to gain experience with smaller experiments before building very large ones. The Caltech Prototype Monopole Detector was an attempt at building and operating a smaller version of what was hoped could be scaled to the size needed to challenge astrophysical limits.

Monopole detectors that are too small to search for monopoles below the astrophysical limits have only a small probability that a monopole could actually be detected. Such detectors had sometimes been designed such that a limit could be set by seeing no monopole candidates, but that a monopole candidate would not be unambiguous enough to establish a flux. It is generally easier to limit than to demonstrate a flux, but a large monopole detector must use a different design philosophy since there is a reasonable possibility that viable monopole candidates would be seen.

While we were limited by the available equipment, we attempted to design the detector as if it were a full-scale experiment, with the philosophy that we were trying to establish rather than to limit a flux. We were not completely successful in this, of course, since prototypes are built to find the mistakes in design and execution.

Thus, one of the goals of the design was to try to detect monopoles unambiguously, so that a monopole signal could not be confused with background processes. This goal indicated that a coincidence of several independent scintillators was desirable, and that they should be separated so that the low velocity of a GUT monopole would be apparent in the timing of signals between different scintillators. The use of a timing coincidence then implies

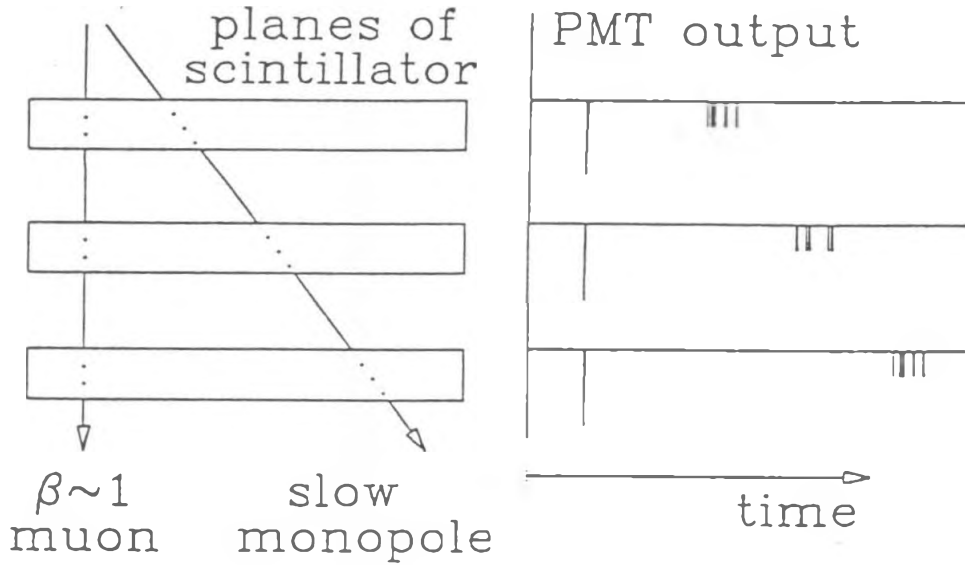


Figure 4.1: Monopole signature expected for slow, lightly ionizing monopole.

that a trigger would be generated near the end of an event, possibly many microseconds after a GUT monopole entered the detector. Figure 4.1 shows the timing signature of a monopole passing through slabs of scintillator, compared with a $\beta = 1$ cosmic ray. For a 'typical' monopole of $\beta = 10^{-3}$, the transit time through our detector was $3 \mu\text{s}$ at vertical incidence, and so the relationship of the trigger to the event timing indicated that some form of signal storage was required. This led to a form of waveform digitization that allowed the events to be reconstructed in time.

When the detector was set up, relatively little was known about the

efficiency of monopoles at producing scintillation light. It was conservatively estimated that slow monopoles would produce a rather small amount of light, on the order of 0.1–0.5 times that of a minimum ionizing particle. Thus, one would expect to observe a few isolated photoelectrons from the PMTs during the transit time of a monopole through a piece of scintillator. If this is the case, then the pulse height information isn't very important, and the monopole signature can be seen in the timing of single photoelectron pulses.

4.2 General Description

The Caltech Prototype Monopole Detector consisted of six 1" thick planes of NE-114 plastic scintillator of dimensions 5' × 10' (See Fig. 4.2). Each plane had two pieces of plastic scintillator with BBQ shifter bars, so that there were four 56DVP PMTs per plane. There was a 'stopping muon target' that consisted of 4" of wood placed between the middle two planes of the detector; some cosmic ray muons would stop in the target and subsequently decay, and the incoming muon and outgoing electron tracks could be detected by the scintillator.

The light yield from a minimum ionizing particle passing through a single

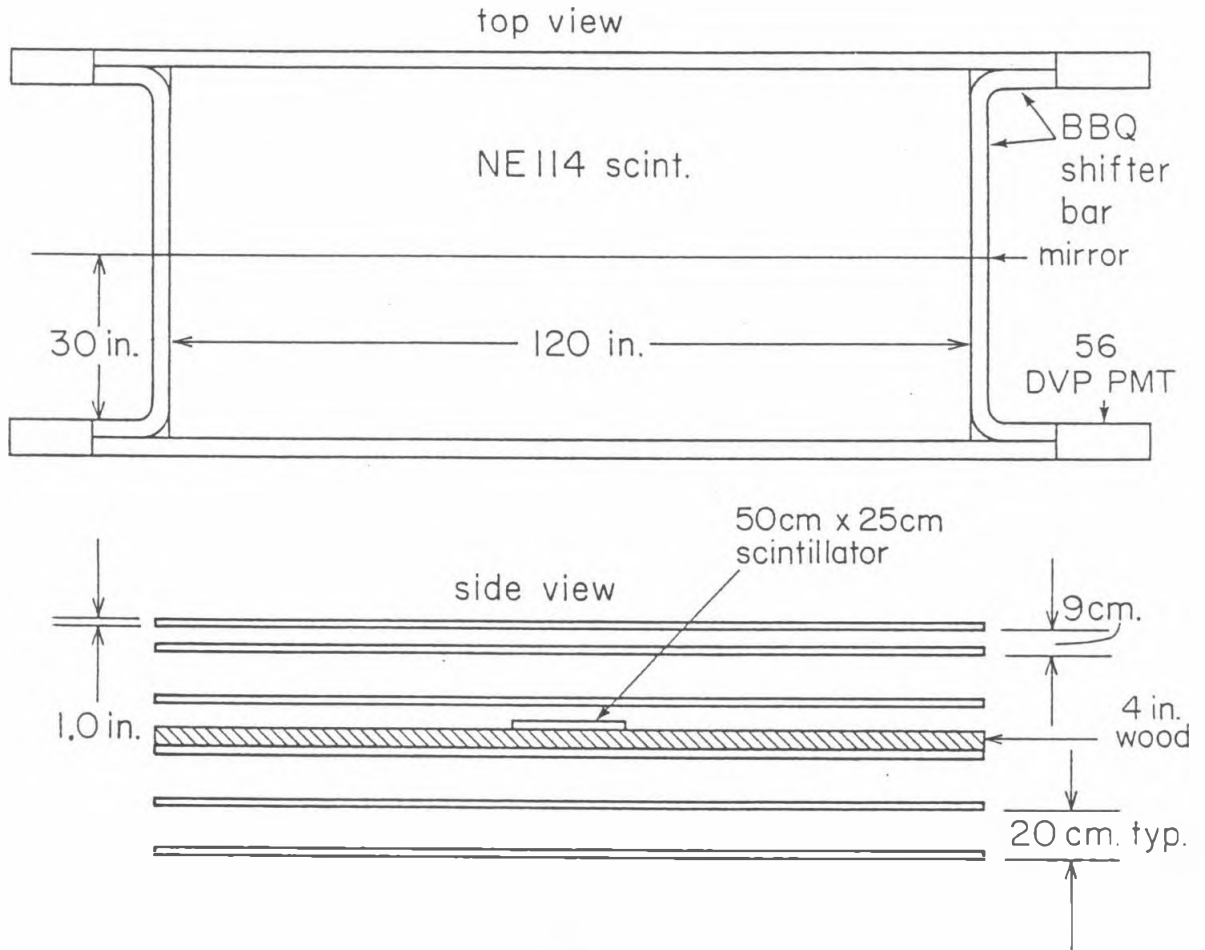


Figure 4.2: The Caltech Prototype Monopole Detector.

scintillator plane was found to be ≈ 14 p.e. in the sum of two PMTs. The PMT signals from each plane were discriminated at the 0.6 photoelectron level and sent to the acquisition electronics. The signals from each plane were also combined to make a timing signal for use in the triggers. Figure 4.3 shows a general overview of the electronics for the monopole detector.

The sum of the PMT signals for each plane was also sent to the acquisition electronics for online monitoring of the detector. This was found to be essential for finding light leaks, bad PMTs, and gain drifts.

The detector was run with several separate triggers:

Slow Particle Trigger: A delayed coincidence of all six scintillator planes, vetoed by the fast particle trigger.

Fast Particle Trigger: Majority of 4 out of 6 planes firing within 50 ns.

Stopping muon Trigger: Coincidence of the top 3 planes and a small scintillator in the center of the array, vetoed by the bottom 3 planes.

'Random' Trigger: A pulser running at 0.01 Hz. Used for diagnostics and in the offline analysis.

The 'Fast Particle' and 'Stopping muon' triggers were prescaled down to rates

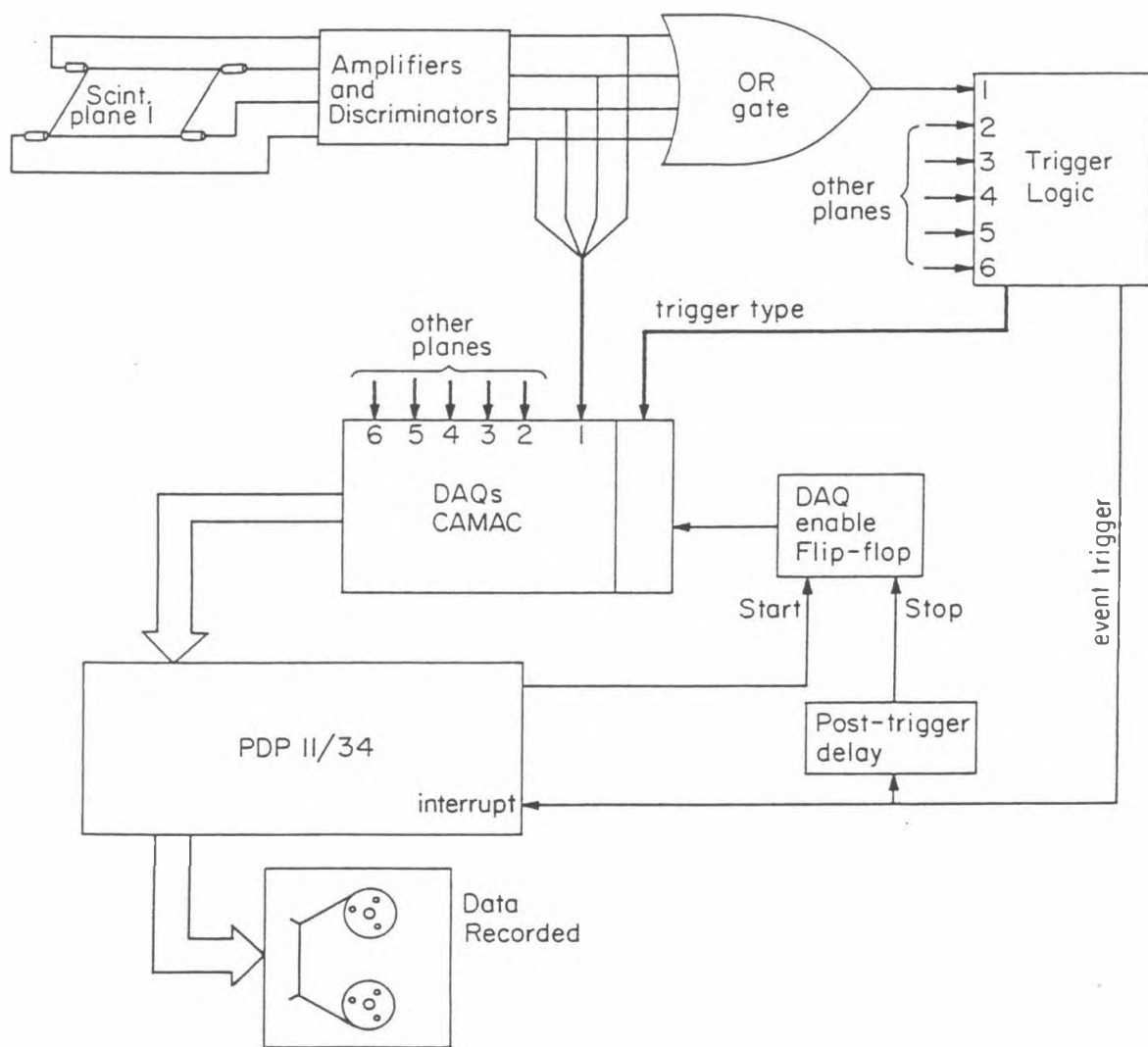


Figure 4.3: Caltech Prototype Electronics overview

of ~ 0.01 Hz so that they would not cause too much deadtime, and to allow tapes on the acquisition computer to be changed at reasonable intervals.

The slow particle trigger used a delayed coincidence between planes to look for downgoing particles. A pulse in the top scintillator plane generated a $2.4 \mu\text{s}$ gate after a ≈ 70 ns delay. A pulse in the second plane in coincidence with this gate would then trigger another delayed gate for coincidence with the third plane. The final coincidence with the bottom plane of the detector was vetoed by the fast particle trigger before triggering the experiment. The slow particle trigger timing was deliberately loose, so that slow particle candidates could be examined offline with better efficiency.

The stopping muon trigger used the coincidence signal of two PMTs on a $\approx 1 \text{ ft}^2$ plastic scintillator, which was placed in the center of the detector on top of the wood muon target. This reduced the number of 'double corner clipper' events, which were a major background for this trigger. The signal from the paddle scintillator was not sent to the acquisition system, nor used for any of the other triggers.

The 'random' trigger was implemented for several purposes. It provided the offline analysis with a sample of typical PMT signals, which were found to be very useful in simulating events and efficiencies offline. As a diagnostic,

it yielded a rough check on the PMT noise rates, which was kept in the data sample. Finally, it provided a minimal event rate which, was useful for the acquisition and monitoring systems.

The various triggers were combined to form a global trigger, which was then sent with the trigger type to the acquisition electronics.

4.3 Acquisition Electronics

The acquisition electronics was contained on 3 CAMAC crates controlled by a PDP 11/34 minicomputer. One of the crates had been previously modified to contain drift chamber DAQ modules for a cosmic ray telescope, with an auxiliary backplane for distributing a global clock.

The DAQ modules were used to record pulses from a multiwire drift chamber. There were 8 ECL inputs for each DAQ, and the logic (aside from the CAMAC interface) was implemented in ECL for speed purposes. The DAQ would record the time from an 8-bit gray code clock running at 125 MHz and 8 bits indicating which wires had fired, allowing a pulse timing resolution of 2 ns over a 512 ns range.

The asynchronous gating of clock times from the auxiliary backplane

required the use of gray code for the clocks. Gray code has only one bit transition per clock interval, which gives an error of at most ± 1 tick because of timing mismatch with the clock transition.

In the original DAQs, the memory filled after the fifteenth pulse and the memory counter would stop at the last memory location so that no more pulses would be recorded. An 'End-Of-Drift' (EOD) signal caused a mark to be written to the ECL memory, and the memory counter reset in preparation for reading out the memory via CAMAC. There was a deadtime after the receipt of a pulse in the DAQ during which another pulse could not be accepted. This was due to the time required (≈ 15 ns) to write the previous pulse into the ECL memory and to update the memory counter.

The original DAQs were read out in time sequence starting at the first pulse in memory and ending when the mark was encountered in the memory. At that point the DAQ would indicate the end of the available data by turning off the CAMAC 'Q' signal and resetting its memory counter. When used with drift chambers, the EOD signal would then be turned off at the start of the next event so that the DAQs would record pulses from it.

Unlike the drift chambers, the prototype monopole detector couldn't turn on the DAQs just before an event, since the event was over by the time a

trigger could be developed. It was necessary to make the DAQs 'free run' until a trigger occurred, and then to read out the most recent pulses. To accomplish this, the DAQs were modified to allow the memory counter to 'roll-over' at the end of its range rather than stopping. The memory would thus constantly overwrite the oldest pulse by the most recent one. To make this work properly on readout, the memory counter had to be prevented from being reset when the EOD signal was turned on. The memory counter would then point to the location after the mark which was written in memory when EOD was turned on, and on readout would cycle through the memory until the mark was encountered, yielding the time history of the event, starting at the oldest pulse.

Both of the modifications above were accomplished with some minimal changes of the DAQ modules, and were fully reversible. Twelve DAQ modules were modified in such a fashion and tested to check for proper functioning.

The timing range of the DAQs as originally used was too short to be useful for examining possible monopole events. The range was increased by using them in pairs with a 'high' and 'low' byte of gray code, yielding 16 bits of clock information, and by slowing the clock rate from 125 MHz to 70 Mhz. This required the design and construction of a 70 MHz 16 bit gray code

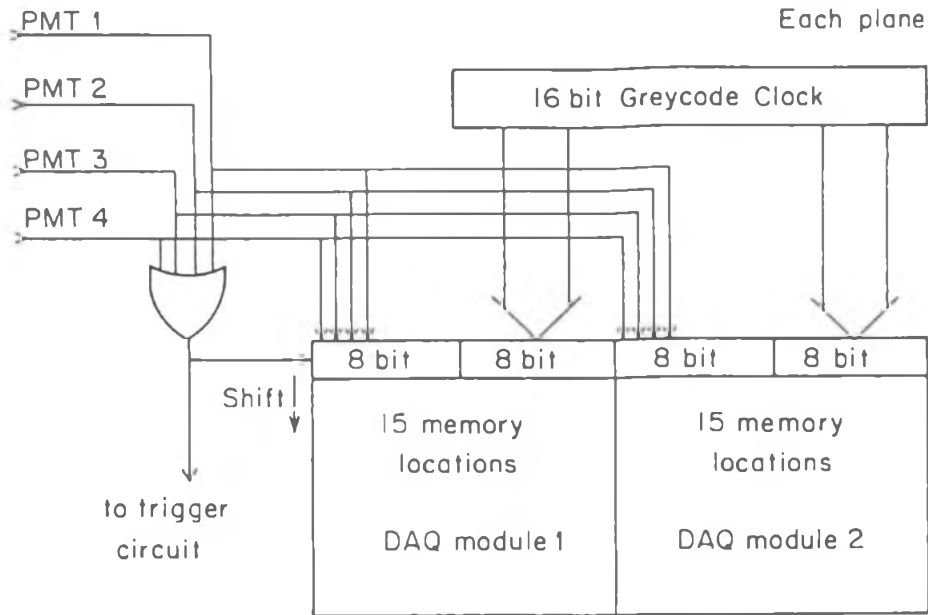


Figure 4.4: Pairs of DAQs used to record PMT pulse times

clock in ECL. The DAQs then had a pulse timing resolution of 7.14 ns with a clock roll-over time of 468 μ s. Figure 4.4 shows schematically how the PMT signals were put into the DAQs with the gray code clock times.

The gray code clock was running while waiting for an event, so it was likely that a clock roll-over would occur at some point in the timing history of an event. The roll-overs could be corrected offline as long as a pulse arrived at the DAQ within the clock roll-over interval. The PMT singles rates made the probability of an undetected clock roll-over quite small ($\approx 3 \times 10^{-7}$).

Since the average singles rate from a scintillator plane was about 32 kHz,

run: 8 event: 2502 type: Slow Particle

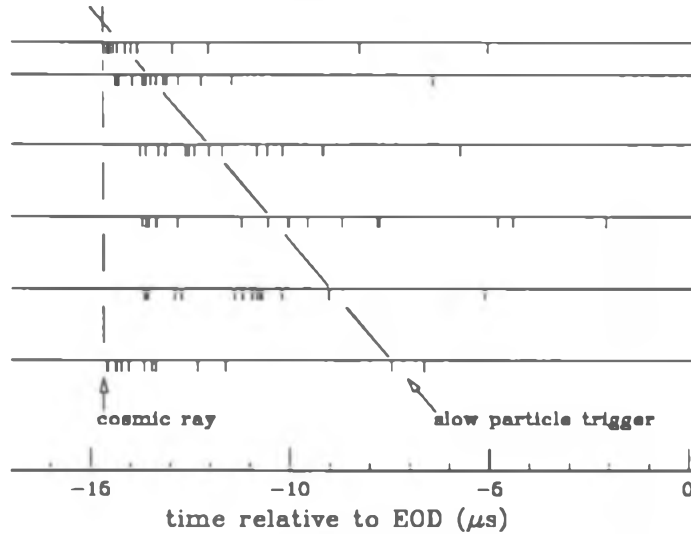


Figure 4.5: Event taken with slow particle trigger. This event was produced by a cosmic ray shower, and produced numerous afterpulses. The DAQs contain only the last 15 pulses from each plane, and so some of the planes don't show the early portion of the event.

the DAQs held an average of 470 μs of event history. In practice, the event history was shorter for all but the 'random' triggers, since the triggers generally picked events which had higher than average pulse rates.

Figure 4.5 shows an event that was taken with the slow particle trigger, but that was the result of a very 'noisy' cosmic ray shower. The timing history of the event is shown like a multitrace oscilloscope, with the horizontal lines representing the six planes of scintillator, and the ticks being pulses from the planes. The relative spacing of the horizontal lines is the same as that of the

detector, so that constant velocities through the detector are seen as straight lines in the timing history.

This event has an extraordinary number of pulses, both from cosmic rays and in afterpulsing by PMTs or scintillator. The DAQs of several of the planes have filled up in this event, and this is why the early history of this event was not seen by all of the planes. The pattern of pulses that fired the slow trigger is indicated.

The experiment was controlled by a PDP 11/34 running a customized version of RT/MULTI. Events from the experiment were logged onto tape for offline analysis on a VAX 780. The events were read into the 11/34 by an interrupt-triggered acquisition subprocess, and there were other subprocesses that handled event logging, experiment monitoring, online analysis, and experiment control. This design allowed the acquisition to proceed with minimal software imposed deadtime, and still to be convenient to work with.

When a trigger occurred, a delay of approximately $10\ \mu\text{s}$ was generated to allow post-trigger pulses to be recorded. The trigger type was latched, the DAQ modules were stopped by turning on the EOD signal, and the 11/34 interrupted via CAMAC to start reading in the event data.

The acquisition subprocess on the 11/34 would then stop the gray code

clock, and then start reading out the DAQs into the event record. The trigger type and the gray code clock time were read and stored in the event record. At the end of an event, the gray code clock was restarted, the interrupt reset, and a pulse sent to turn off the EOD signal and thus to re-enable the DAQs for taking data. A post-acquisition deadtime of $\approx 100 \mu\text{s}$ was imposed on the triggers to restrict the burst trigger rate to one which the 11/34 could handle. The event was tagged with run and event number and the date and time and was passed to the logging subprocess for writing on tape.

The third CAMAC crate was used for experiment monitoring, and was operated from a separate CAMAC controller to avoid contention with the acquisition processes. The monitoring was accomplished by gating a multichannel scaler for $\approx 0.5\text{s}$ and counting PMT singles from each plane, as well as from a pulser. Since a gating period long enough to obtain reasonable count statistics ($> 100\text{ms}$) was required, and the scaler could not be free-running because of roll-over problems, the monitoring was done by a separate subprocess in the 11/34. The gating period of the monitoring scaler was slightly variable because of the acquisition and logging subprocesses having priority on the available processor time, so the fixed rate pulser was used to normalize the singles counts to a standard interval.

A running average was kept of the PMT singles rates, and messages were logged on a hardcopy terminal when the singles rates deviated from the average by more than about 4σ . It was also possible to make a plot of the singles rate as a function of event number so that PMT noise rate excursions could be seen directly.

The monitoring function was found to be extremely useful during the early shakedown running of the experiment, in which a number of PMTs were found to be bad and a NIM crate power supply failed. After the shakedown period, the monitoring gave considerable confidence that the detector could be left unattended and yet not have problems go unnoticed.

4.4 Operation & Analysis

The detector was run for approximately 100 days, taking 9.8×10^5 events for offline analysis.

The first steps of the analysis were to extract and combine the DAQ clock times and PMT bits, convert the DAQ clock times from gray code to standard binary, and insert clock roll-overs where needed. The relative timing of the planes were adjusted by the small amounts needed (typically ± 1 tick) to

account for relative delays in the DAQ modules. The timing of an event was referenced to the gray code time at the end of the event (EOD), since it was uniquely defined by the trigger. Working backwards from the EOD, clock roll-overs were inserted wherever the DAQ time was found to increase from a pulse to the preceding pulse.

The relative timing of the planes was adjusted in software since the cables and other components made such adjustments difficult to do directly. A sample of cosmic ray events was taken and the tracks found in the timing history by their position relative to the EOD. The timing differences between planes were averaged and the offsets applied to bring the planes into agreement. This did not account for timing variations between different PMTs of a plane, nor for variations due to the position of a cosmic ray hit on a scintillator plane, but these effects had been observed to be small enough to be ignored and the subsequent analysis was insensitive to them.

There were a small number of events that required fixing offline due to mismatches of the PMT bits between the high- and low-DAQs, and some that were incomplete because the trigger for them arrived before the DAQs could refill with timing history. These latter events were necessarily removed from the analysis, since the design of the modified DAQs caused them to read out

pulses left from the previous event in such cases, rather than the new pulses. The PMT bit mismatches were due to slight differences in the gating intervals between the high- and low-DAQs, and were fixable by ORing the PMT bits from the two. In nearly all cases, these events were the result of two PMTs of the same plane firing within a short interval.

Another more difficult class of 'bad but fixable' events were those in which there was an offset between high- and low-DAQ timing histories, in general occurring when one of them recorded two PMTs firing at once and the other recorded them as separate pulses. These were found to be fixable by pattern matching the PMT bits and checking for offsets while scanning through the timing history. A small number of these events were ambiguous enough so as to defy fixing, and were necessarily thrown out.

There was about 30% of the events that required the offset fixing at some point in their event history, but in almost all cases the offset occurred early in the timing history and the pulses in the region of interest near the trigger time were not affected by offsets. The slow particle candidates in the analysis were checked and found not to have such possible offsets during the time interval for which candidates were found. The number of events left after the procedures above was 9.6×10^5 .

run: 171 event: 5528; type: Fast Particle

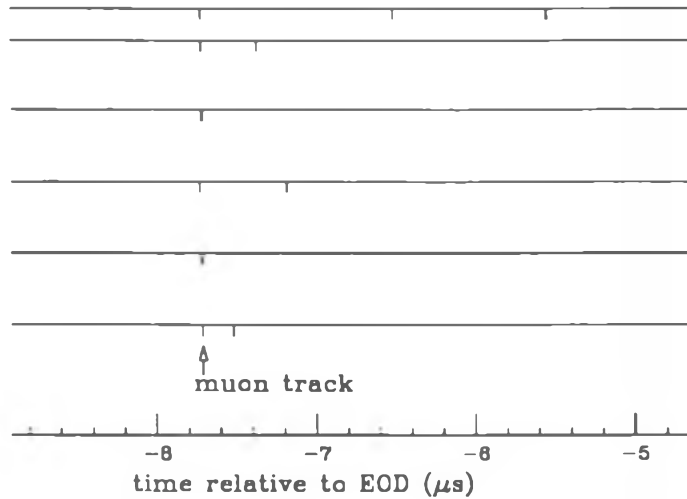


Figure 4.6: Fast particle event taken with the detector. The timing coincidence between the scintillator planes allows the identification of $\beta = 1$ cosmic ray background.

4.4.1 The Data

Figures 4.6 and 4.7 show events that were taken with this detector. The tracks of cosmic rays are clear and distinctive, with a timing difference of ± 1 tick between planes. It is also clear from even a small sample of events that the singles rate after a cosmic ray is much higher than at earlier times.

This was due to afterpulsing in PMTs or the BBQ shifter bars and was a major nuisance in this experiment. Afterpulsing from PMTs occurs when electrons inside the PMT ionize gas atoms, which then drift to a dynode and

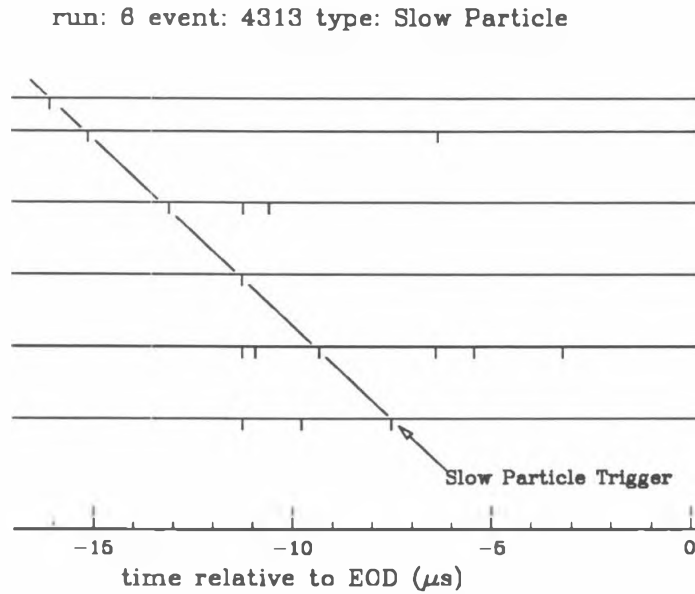


Figure 4.7: An event which fired the slow particle trigger. This particular event was a slow particle candidate in the analysis, but some of the pulses come from a $\beta = 1$ cosmic ray at $\approx -11 \mu s$. The higher rate of pulses to the right of the cosmic ray track comes from afterpulsing.

produce a late pulse. PMTs that have been in a helium-rich environment are particularly prone to afterpulsing, since the helium will diffuse through the glass envelope of the PMT and contaminate it.

BBQ afterpulsing occurs when metastable states in the fluors are excited and subsequently decay. This was not believed to be the primary source of afterpulsing in this experiment, but it could not be ruled out. In either case, the result is that a cosmic ray would often cause afterpulsing for some microseconds after its passage. While the cosmic ray could be identified, and to some extent vetoed at the trigger level, the afterpulses were more difficult to deal with.

4.4.2 Slow Particle Analysis

The slow particle trigger analysis was done elsewhere³², but a short summary of the analysis is appropriate here.

Slow particle candidates were found by searching the events for tracks that corresponded to a fixed, low velocity through the scintillator array. Fast particle tracks were removed by looking for coincidences between adjacent planes within a short period of time, and PMT afterpulses were checked for,

after fast particle tracks, and removed if present. A check was made based on the track geometry, so that candidate tracks were consistent with a straight line through the detector.

The cuts mentioned above were also performed on a sample of Monte Carlo slow particle events. These events were generated by adding pulses typical of a slow particle signature to events of the 'random trigger' data sample. The Monte Carlo events gave an idea of what a slow particle would look like when present in the cosmic rays and PMT noise of the detector. The number of these Monte Carlo slow particle events that passed the cuts above was then used to quantify the efficiency of the cuts.

The analysis efficiencies were factored into the experimental efficiencies and live-time calculations. The final sample of slow particle candidates was examined in terms of ionization and β distribution, and a flux limit set.

4.5 Results

A valuable check on the operation of the detector was provided by events obtained with the stopping muon trigger. The stopping muon trigger events were separated from the data, and an analysis program was used to find

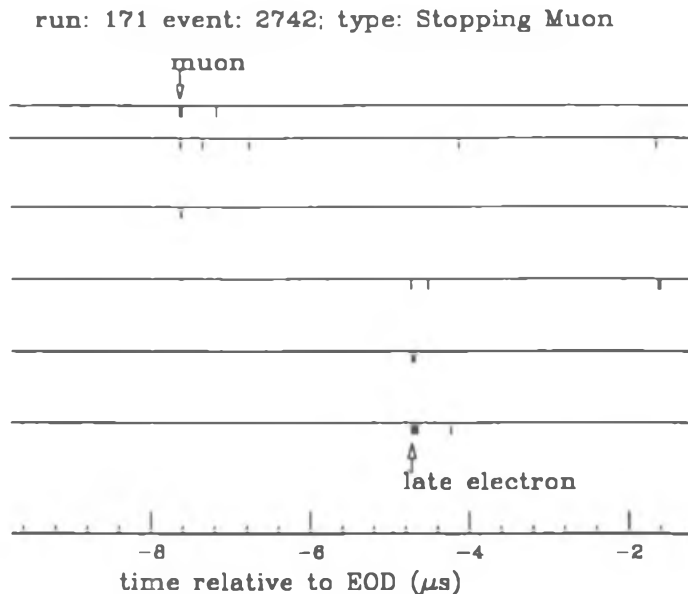


Figure 4.8: A stopping muon event. The stopping muon event has a timing coincidence of the top three planes from the incoming muon, and a later coincidence of the lower three planes from the outgoing electron.

the outgoing electron track from the $\mu \rightarrow e\bar{\nu}_e\nu_\mu$ decay. Figure 4.8 shows a particularly clear example of such an event. The electron track was taken to be a timing coincidence in the bottom three planes at least 50 ns after the stopping muon track. The delay was to help reduce contamination from muon events with afterpulsing.

A histogram of the number of events as a function of the time between the muon and electron tracks is shown in Fig. 4.9. A 'lifetime' slope of $\approx 2 \mu\text{s}$ was fitted to the decay curve. The μ^+ and μ^- lifetimes are different in the

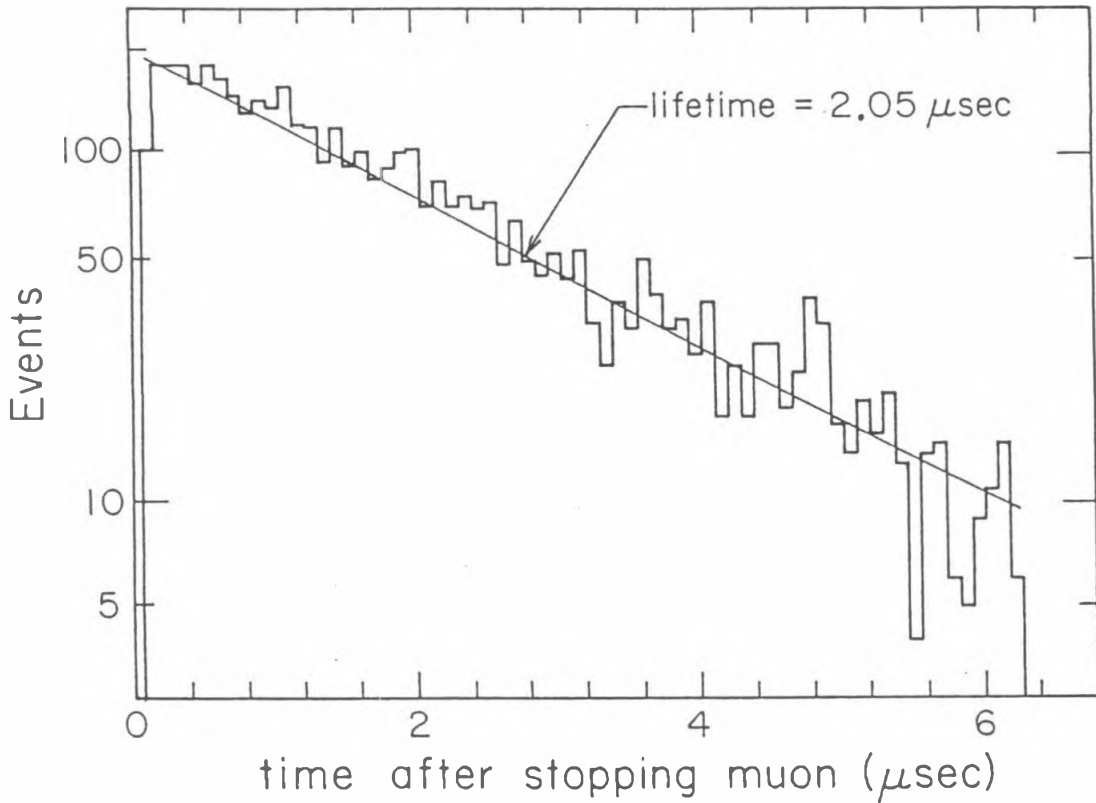


Figure 4.9: Lifetime curve for cosmic ray μs stopping in the detector. The fitted slope of the curve is consistent with muon decay in the wood target. The statistics are insufficient to separate the μ^+ and μ^- components.

target because of nuclear capture effects, but they cannot be separated with the statistics of the decay plot shown.

The analysis of slow particle triggers resulted in a flux limit (90% confidence) of $4.7 \times 10^{-12} / (\text{cm}^2 \text{sr s})$ for massive particles with $2.7 \times 10^{-4} \leq \beta \leq 5 \times 10^{-3}$ and with a light yield greater than 1/3 that of a minimum ionizing particle.

If the stopping power calculations and light yields from preceding chapters are used, a monopole with a Dirac magnetic charge should produce light equivalent to 1/3 of that of a minimum ionizing particle down to at least $\beta \approx 4 \times 10^{-4}$, and possibly as low as $\beta \approx 2 \times 10^{-4}$. It is assumed here that since no β cutoff was observed for proton scintillation, this should also hold for monopoles.

The monopole flux limit achieved with this experiment is well above the Parker bound (See Fig. 4.10), and in fact other experiments have achieved lower flux limits. This was, however, one of the better scintillator monopole searches that have been conducted on the Earth's surface. As such, it was sensitive to slow 'medium heavy' particles of mass $\sim 10^9$ GeV, of either electric or magnetic charge³³. Examples of such particles are nuclearites³⁴, also known as 'strange quark matter,' and particles of 1/5 charge from superstring

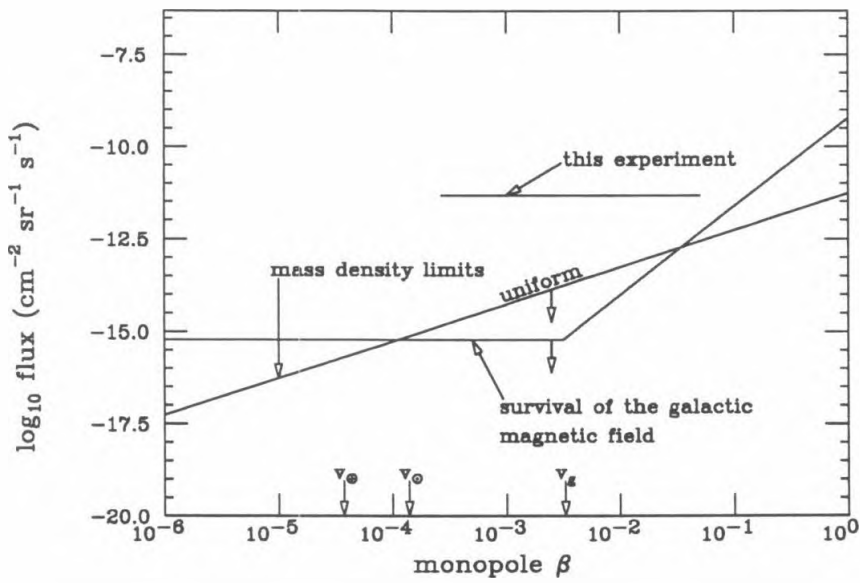


Figure 4.10: Comparison of the monopole flux limit achieved with the prototype monopole detector with the astrophysical limits of Turner, *et al.*⁹ for a 10^{16} GeV monopole.

theories³⁵.

Underground experiments are generally insensitive to this mass range because of the particles stopping in the Earth's crust. Some of the monopole detectors at the Earth's surface used a geometry with vertical layers or high ionization thresholds, and hence were also not very sensitive to these particles. While cosmological limits and bulk matter searches make a significant flux of monopoles of this mass range unlikely, these limits do not apply to electrically charged particles.

The calculations and results from previous chapters indicate that 'medium heavy' electrically charged particles should produce enough light to exceed the $1/3$ minimum ionizing threshold when $\beta > 6 \times 10^{-4}$ for a $|Z| = 1/5$ particle, $\beta > 3.5 \times 10^{-4}$ for a $|Z| = 1/3$ particle, and the full trigger β range is sensitive for a $|Z| \geq 1$ particle. These β thresholds are conservative and will probably decrease when better scintillation efficiency measurements are available.

A new upper flux limit was set for these 'medium heavy' slow particles in cosmic rays, which gives a stringent limit on the fraction of the dark matter that can be composed of such 'medium heavy' particles, shown in Fig. 4.11.

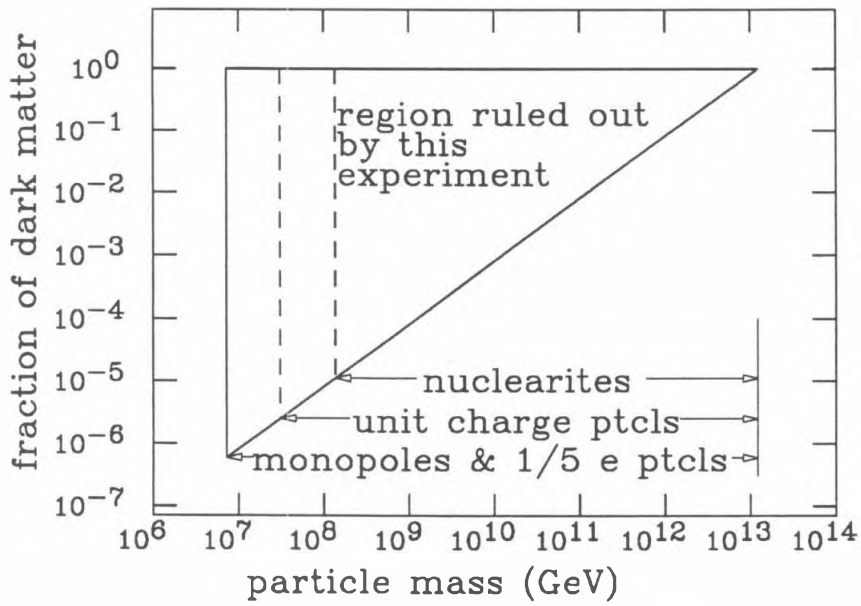


Figure 4.11: Limit of the fraction of dark matter that can be attributed to heavy charged particles, as a function of mass.

4.6 Conclusions

The results obtained with the prototype for ‘medium heavy’ charged particles are certainly new and interesting, but the primary gain that was achieved with our detector was in knowledge applicable to the design and operation of large-scale monopole detectors.

It was clear that the detector had too much background for monopole detection to be unambiguous. The major source of slow particle background was cosmic rays; there was very little slow particle background associated with PMT dark noise or radioactivity. In particular, cosmic rays passing through the detector would cause many afterpulses, which would then generate false slow particle triggers. Direct coupling of the PMTs to the scintillator could eliminate BBQ afterpulsing, and better PMTs were also needed to help reduce afterpulsing.

Cosmic rays would still remain the major background, and the desire to reduce this background led to the consideration of underground detectors. The use of a closed geometry was indicated by the numerous ‘corner clipper’ events that were found among the slow particle candidates.

The desire for coincidence between independent detector elements as part

of a slow particle signature and the use of slow particle timing as part of that signature pointed the way for the use of waveform digitizers in recording slow particle events. More modern techniques for waveform digitization have evolved since this experiment, particularly in providing accurate pulse-height information, but the techniques used in this experiment still stand up well for obtaining accurate pulse times over a wide timing range.

The detector certainly had too little light from the scintillator, which aggravated some of the problems mentioned above. It was clear that a realistic design for a large monopole detector would have to do better at light collection from scintillator, since the scintillation light is the raw material for the subsequent steps in the triggering and data collection processes.

Chapter 5

Liquid Scintillator Optics

5.1 Introduction

The use of liquid scintillator detectors was motivated by the availability of long attenuation length liquid scintillators. These scintillators are based on a solution of pseudocumene (1,2,4-trimethylbenzene) in mineral oil and have relatively low light output compared to plastic scintillators or other liquid scintillators such as NE-213. Still, their attenuation lengths of 6–8 m make them attractive for large detectors.

The MACRO experiment⁴ is a large-scale monopole detector for which liquid scintillation counters were selected. A prototype MACRO liquid scin-

tillation counter was built at Caltech, and much effort has gone into measuring and explaining its performance, and into finding ways to optimize liquid scintillation counters for both slow and fast particle detection. This counter was then shipped to Italy so that it could be used in tests to be conducted in the Gran Sasso tunnel, where the MACRO detector will be built.

There was another prototype counter built with somewhat different techniques at the University of Michigan for essentially the same purpose. This counter used the same photomultiplier tubes (PMTs) and basic dimensions as the Caltech counter, but also had a different lining (aluminized Teflon) and a more transparent window between the PMTs and the scintillator. The differences in response of the Caltech and Michigan counters prompted much of the work in this chapter.

One of the goals of MACRO is to identify upward-going muons produced by neutrino interactions in the rock below the detector. There is a background of $\sim 10^4$ downward-going cosmic ray muons for each upward-going muon, and the separation of the upward-going muons from the background is done with time-of-flight between liquid scintillator counters. Timing and pulse-height measurements are also used to obtain information about the position and ionization of particles passing through the liquid scintillator

counters.

A ray-tracing program was written to simulate the optics in the liquid scintillator counters, to help isolate the effects of various components of the system in a way that can be difficult on an actual prototype, and to help optimize the design. The optimization was primarily directed toward the overall light level, but considerations of dynamic range and pulse timing were still important. In this chapter I will be presenting prototype data, results from the ray-tracing program, and direct calculations with the goal in mind that they should all fit together in explaining the behavior of the counters, and in pointing the way to improve performance of these counters.

In most of this chapter it will be assumed that the scintillation light is monochromatic, so that the refractive indices, attenuation lengths, etc. will be constants. Of course, the light from a scintillator is only approximately monochromatic, and the major effect for which this fact is relevant is in the decrease of attenuation length with decreasing wavelength. Much progress has been made in understanding the wavelength-dependent features of these liquid scintillation counters, but discussion of these issues will be confined to the section on wavelength dependence.

5.2 Basic Concepts

5.2.1 Total Internal Reflection

Light produced by particles passing through a liquid scintillator counter is propagated to photomultiplier tubes by means of total internal reflection. This is accomplished by surrounding the liquid scintillator with a medium of lower refractive index (a 'lining'). The critical angle with respect to the surface normal is given by

$$\Theta_c = \sin^{-1} \left(\frac{n'}{n} \right), \quad (5.1)$$

where n is the refractive index of the liquid scintillator (typ. 1.45) and n' is the refractive index of the lining. Rays of angle $\Theta > \Theta_c$ with respect to the surface normal will be totally reflected, while others will be only partially reflected from the lining.

It can be seen that n' should be made as small as possible to increase the amount of light that is totally reflected. Air makes a good lining ($n' = 1.00029$), but there are difficulties in surrounding a liquid with air on all sides. Instead, Teflon with $n' = 1.33$ is used, giving $\Theta_c = 66.5^\circ$.

The subject of reflection from liquid scintillator linings will be dealt with

further in a later section of this chapter. However, the concepts outlined above are fundamental to the understanding of the optics of liquid scintillator counters, and the rest of this chapter will draw heavily on them.

5.2.2 A Standard Counter

Figure 5.1 shows the liquid scintillator counter which was used for most of the prototype work. The counter was a 50 cm wide and 12m long tank that was filled to a depth of 25 cm with liquid scintillator (Bicron BC-517P), with a Teflon lining on the bottom and sides for total reflection. The air above the scintillator produced total reflection from the top surface. The dimensions (primarily the width) of the prototype are different from that of the liquid scintillation counters that will be used in MACRO, but since the data from the prototype and many of the simulations use the prototype dimensions above, the $50 \times 25 \times 1200$ cm counter will be used as a standard of comparison.

It is convenient to define a coordinate system on the counter, with the z axis along the length of the counter and the x and y axes along the bottom and left side, respectively. Photomultiplier tubes are placed at $z = 0$ and

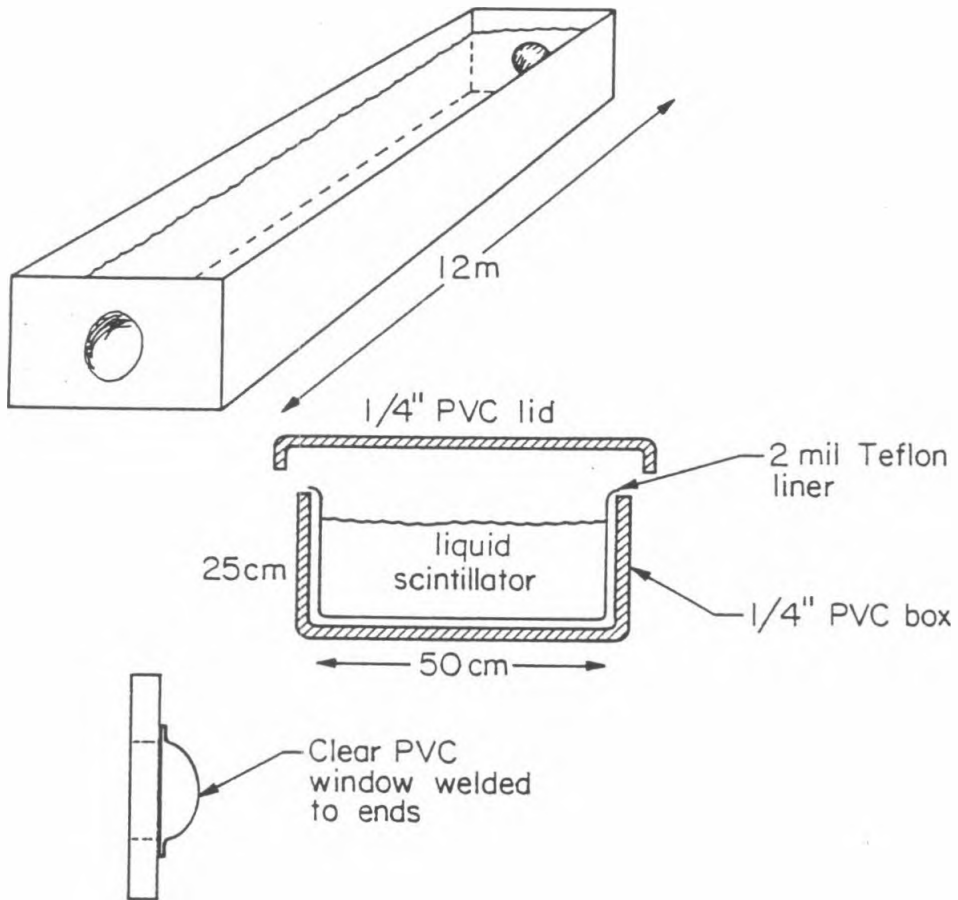


Figure 5.1: Liquid scintillation counter prototype that was constructed for tests. This counter was used at Caltech for about a year, then shipped to Italy for tests in the Gran Sasso tunnel.

$z = 1200$ cm, although in general I will only refer to the PMT at $z = 0$ for simplicity.

For a long rectangular counter it is also useful to use the angle θ of a ray with respect to the z axis in examining its behavior. The use of θ is motivated by the invariance of θ for a ray moving down a rectangular counter by reflections from the sides, and also by its relation to the total internal reflection angles. The angle ϕ denotes the angle of a ray about the z axis with respect to the x axis, so that θ and ϕ are the angles of a spherical coordinate system.

There is a point that may cause some confusion: θ is measured from the z axis, which lies in the planes where most of the reflection occurs, while the angles of reflection are measured from surface normals that are generally perpendicular to the z axis. In this chapter, the symbol Θ will be reserved for angles with respect to surface normals, which is the usual convention in optics, while θ denotes angles from the z axis. In particular, a ray travelling down a counter with angle θ will experience reflections at normal angles that can range from $\pi/2$ to the minimum Θ given by

$$\Theta_{\min} = \frac{\pi}{2} - \theta .$$

In general, I will use Θ when analyzing individual reflections, and θ and ϕ for describing the propagation of a population of photons. Since rays with $\Theta > \Theta_c$ will be totally reflected by the lining material, it can be seen from the equation above that there is an angle θ_c such that all rays with $\theta < \theta_c$ will be totally reflected.

5.2.3 Attenuation

Scintillation light from an ionizing particle is propagated down the counter to the PMTs by total internal reflection, and attenuated by the scintillator and imperfect reflections from the walls of the counter. If $I(z)$ is taken as the intensity of light from a source located at a distance z along the counter, then one can approximate the attenuation in the limit of large z by

$$I(z) = I_0 e^{-z/a} , \quad (5.2)$$

where a is the attenuation length. The quantity I_0 is called the 'light level,' since the equation above decouples the overall light level from the effects of attenuation.

The intensity $I(z)$ is properly a photon or energy flux, but it is often put in terms of the number of photoelectrons detected at the PMT for a

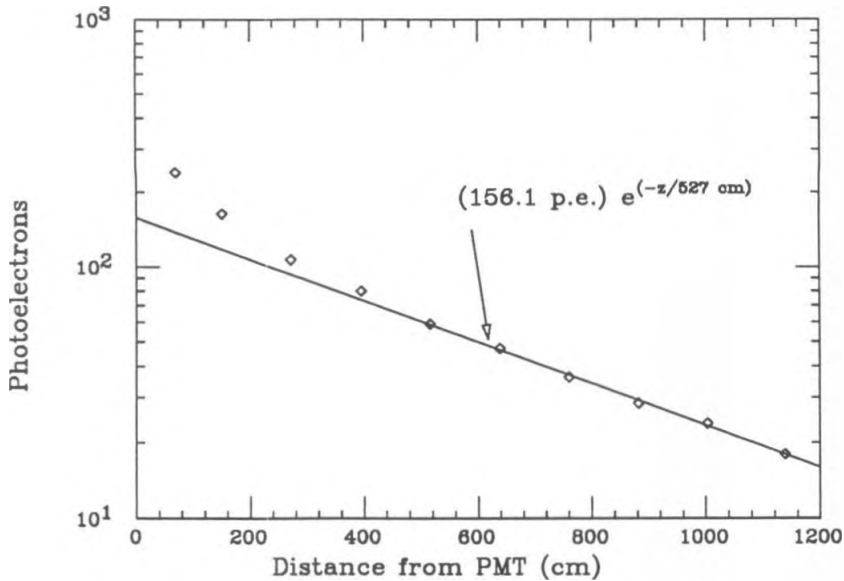


Figure 5.2: Response curve of the Caltech MACRO prototype counter, in photoelectrons for a vertically incident minimum ionizing cosmic ray. The response has been fitted with an exponential. The PMTs were contained in oil-filled housings, with a 'blueish' plastic window.

minimum ionizing particle (such as a cosmic ray muon) passing through a counter vertically. This convention lumps factors such as scintillation and PMT efficiencies into the light level, and is convenient both for experimental calibration and for comparison with theory predictions for other particles. The function $I(z)$ is referred to as the 'response curve' of the counter. Figure 5.2 shows a response curve that was measured on the liquid scintillation counter at Caltech³⁶.

The attenuation length a is also called an 'effective' attenuation length,

since it is the attenuation with distance along the counter rather than along the actual path of a ray. If a given ray propagates down the counter with an angle θ with respect to the z axis, then there is a factor of $\cos \theta$ between the 'effective' path length and the actual distance travelled through the scintillator. The attenuation due to the scintillator ('bulk' attenuation) occurs over the actual path length, so the relationship between the bulk attenuation length (a_b) of the scintillator and effective attenuation length (a) may be expressed as

$$a = a_b \cos \theta \quad (5.3)$$

for a single ray. Thus, for rays emitted within a solid angle element $d\Omega$ one has

$$\frac{dI}{d\Omega}(z) = \frac{dI_0}{d\Omega} e^{-\frac{z}{a_b} \sec \theta} \quad (5.4)$$

for rays that are totally reflected by the lining. An effective attenuation length then represents an average over the angular distribution that is totally reflected. The effective attenuation length will increase with distance as the short attenuation length components of the light die out.

In practice, as long as $\Theta_c \gtrsim 45^\circ$, there is little change in the effective attenuation length with distance. Figure 5.3 shows the ratio of effective to

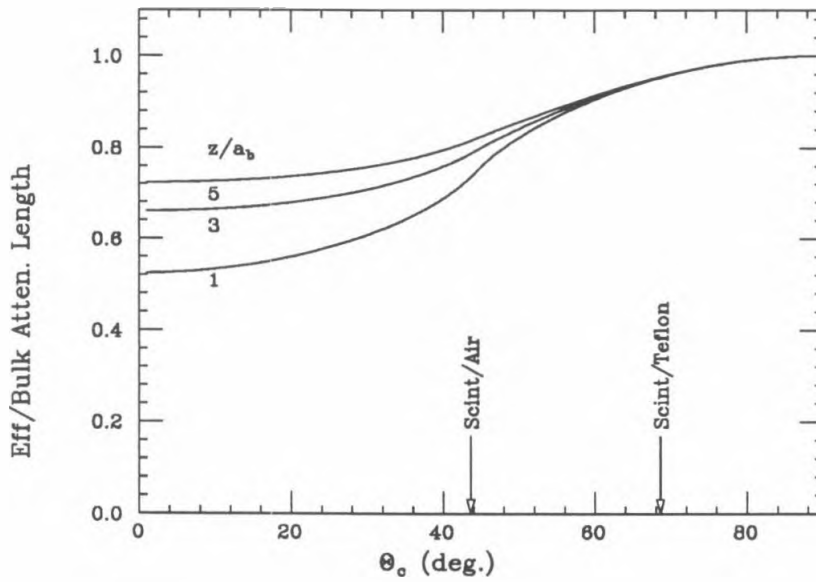


Figure 5.3: Factor for obtaining the effective attenuation length in counters with dielectric lining, as a function of the critical angle θ_c . The curves have been calculated at several values of z/a_b .

bulk attenuation lengths as a function of Θ_c for several distances z/a_b . For liquid scintillator with a Teflon lining (using the Θ_c obtained previously) one finds

$$a = (0.943)a_b$$

with less than 0.5% variation from 1 to 5 attenuation lengths.

5.2.4 Design Variations

There are variations to be considered in the width of counters, the number and size of the PMTs at each end, and of the lining materials used to achieve total internal reflection. The response curve scaling caused by variation of the counter width, as well as the scaling due to variations of PMT size and number, are subsumed into the factor f for the fraction of the area on the end of a counter which is covered by PMTs. This factor appears in the acceptance equations below, where the counter details concealed in f will not be dealt with separately.

The analysis of the different linings of the counters is more difficult, and there are separate calculations applied to the main cases in a section below.

The use of mirrors around the PMTs at the ends of the counters is also

dealt with in a separate section. There are many ways that such mirrors could be configured, but only a few configurations merit consideration.

It is generally undesirable to place PMTs directly in scintillation oil, since the amount of light from radioactive background near the PMTs is then quite large. The PMTs were separated from the scintillator by windows, so that the transparency of the windows becomes an issue in the counter design. Some early tests were done with the PMTs in air; this decreased the response of the counters because of the air/window interface.

Immersing the PMTs in mineral oil (non-scintillating) increased the response by 50% or more. Since the plastics used for windows (PVC's and acrylic) had indices of refraction close to that of mineral oil, the light loss from this PMT coupling arrangement should be minimal. The effects of window variations is considered in the wavelength dependence section (5.9), since that was where they had the greatest effect.

5.3 Total Internal Reflection Optics

Consider a scintillator of refractive index n that exhibits total internal reflection with an external medium, so that the critical angle is Θ_c . Rays with

$\Theta > \Theta_c$ will be totally reflected at the surface, while those with $\Theta < \Theta_c$ will be only partially reflected and will eventually attenuate to a negligible intensity.

The response curve shown of the scintillation counters may be characterized in two regimes. There is the 'near' response ($z \lesssim 2\text{ m}$), for which most of the detected light doesn't reflect from the lining but instead is intercepted by a PMT directly. This may be approximated by

$$I(z) = I_S \frac{\Omega_{\text{pmt}}(z)}{4\pi} e^{-z/a}, \quad (5.5)$$

where Ω_{pmt} is the solid angle subtended by the PMT as viewed from the source of light, and I_S is the intensity of the source. If the PMT is approximated as a circular aperture of radius R centered on the end of a counter, and a point source of light on the centerline of a counter is assumed, then an expression is obtained,

$$\Omega_{\text{pmt}}(z) = 2\pi \left(1 - \frac{z}{\sqrt{z^2 + R^2}} \right) \approx \frac{\pi R^2}{z^2} \text{ for } z \gg R \quad (5.6)$$

which shows '1/ r^2 ' behavior.

When the light source is far enough from the PMT so that several reflections can take place ($z \gtrsim 2\text{ m}$), the response is dominated by a different behavior. Some of the photons will be totally reflected by the counter lining

and propagate down to the end of the counter, with attenuation due to absorption by the scintillator. The rays that are only partially reflected by the lining will lose intensity at each reflection and will quickly fade to a negligible intensity. After a few reflections, the distribution of photons on the end of the counter is essentially random, and the response may be modeled as

$$I(z) = I_S \frac{f \Omega_c}{2 \cdot 4\pi} e^{-z/a}, \quad (5.7)$$

where f is the ratio of the area of the PMT to that of the end of the counter, and Ω_c is the solid angle from a source which is contained within the total internal reflection angles. The factor of one-half indicates that half of the totally reflected light propagates towards each end of a counter. This is the 'far' or 'exponential' response that dominates the response curves of the liquid scintillation counters.

The response curve shown in Fig. 5.2 illustrates the exponential response of these scintillation counters at sufficiently large z , but the response near the PMT doesn't fall off fast enough to be described by Eqn. 5.5 above. This is because the ' $1/r^2$ ' feature seen in prototype data is not geometric in origin, but rather, spectral; part of the scintillation spectrum is being attenuated preferentially, and this shorter attenuation length component mimics a $1/r^2$

response.

The effect of using different lining materials in varying the critical angle is contained in Ω_c , so the calculation of Ω_c is very useful in examining the light level of these counters.

5.4 Solid Angle Calculations

There are some ideas and calculations that should be shown before obtaining a value for Ω_c . Consider an infinite plane that is the interface between scintillator and a medium with a lower refractive index. The critical angle is taken to be Θ_c . A point source of light is assumed in the scintillator, and only those rays outside a cone of half-opening angle Θ_c with respect to the surface normal will be totally reflected (See Fig. 5.4(a)).

If a unit sphere is placed around the source point, then the intersection of the cone and the sphere defines a circle on the sphere. The solid angle that is not totally reflected may now be identified with the area interior to this circle, and is denoted Ω_f . One finds

$$\Omega_f = 2\pi(1 - \cos \Theta_c) \tag{5.8}$$

by simple geometry.

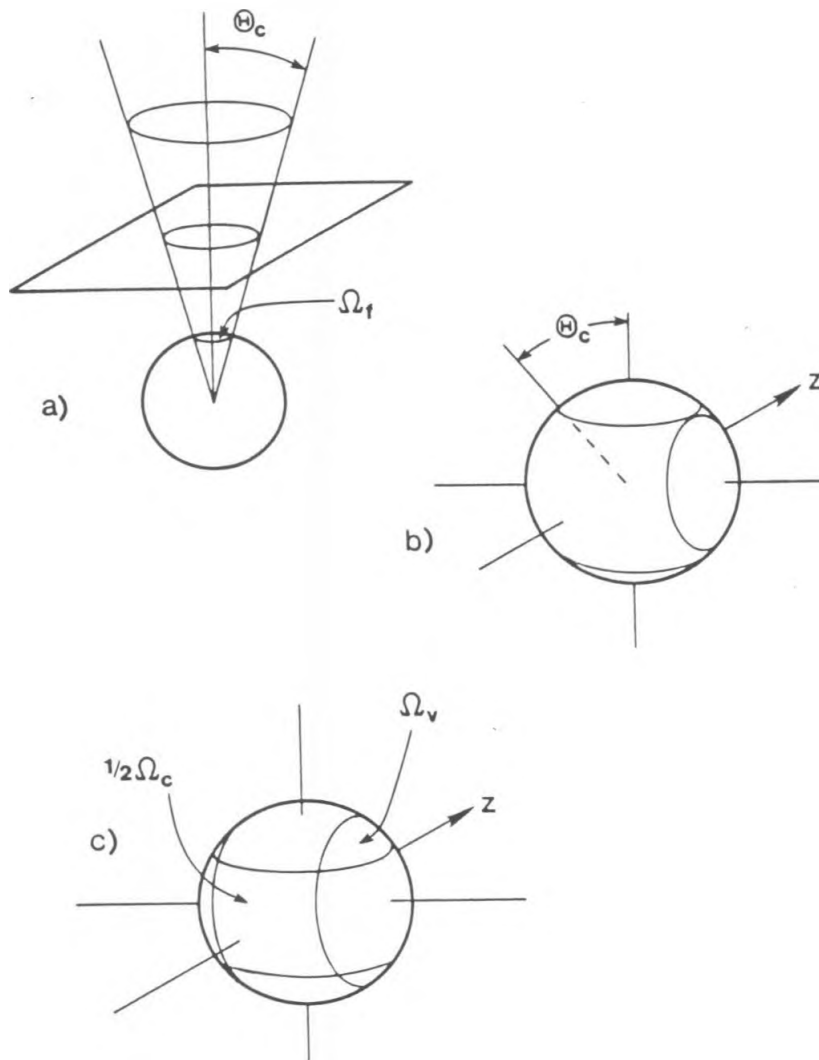


Figure 5.4: Solid angles useful in analyzing rectangular liquid scintillator boxes. (a) Figure shows the solid angle from a point light source that can escape by partial transmission through a plane surface. The solid angle Ω_f is equivalent to the area of a circle on the unit sphere. (b) When the top, bottom, and sides of a box are included, one obtains four such circles on the unit sphere. (c) If $\Theta_c > 45^\circ$, the circles overlap at their edges. The area of each overlap is denoted Ω_v . The solid angle that remains after removing these circles is Ω_c .

If the other planes of a rectangular box are added, then the result is a set of circles (possibly intersecting) on the surface of a unit sphere (see Fig. 5.4(b)). It should be clear that rays from the source point that are emitted into one of these circular areas will escape from one of the faces of the box, although it may require a reflection from one of the other faces. Rays that are not emitted into a circular area will be trapped in the scintillator, and eventually will be attenuated or scattered.

The case of interest is a scintillator counter that is much longer than its width. In calculating Ω_c then, one should subtract from 4π those solid angles that are not totally reflected from the sides, top, and bottom of the counter, and the remainder is what will propagate to the ends of the counter by total reflection. This solid angle corresponds to the area of the unit sphere with four circular areas cut out.

When Θ_c is larger than 45° , the circular areas will overlap at their edges, and this must be accounted for in calculating Ω_c . The solid angle contained in the overlap of two circular areas centered 90° apart on the unit sphere is denoted Ω_v (see Fig. 5.4(c)). It is obtained from the integration of the

overlap area on the unit sphere

$$\Omega_v = \int_{\cos \Theta_c}^{\sin \Theta_c} dy \int_{-(\sin^2 \Theta_c - y^2)^{1/2}}^{(\sin^2 \Theta_c - y^2)^{1/2}} (1 - x^2 - y^2)^{-1/2} dx, \quad (5.9)$$

which eventually yields

$$\Omega_v = 2 \cos^{-1}(\cot^2 \Theta_c) - 4 \cos \Theta_c \cos^{-1}(\cot \Theta_c). \quad (5.10)$$

The derivation of the above equation is tedious and has been omitted here.

For Ω_c it is assumed that the PMTs at the ends of the counters are completely absorbing: there is no 'exit' solid angle for a photon to be detected. This is the case when PMTs are immersed in the liquid scintillator, or otherwise optically coupled with matching refractive indices, and yields

$$\Omega_c(\Theta_c) = \begin{cases} 4\pi - 4\Omega_f(\Theta_c) & \Theta_c < 45^\circ \\ 4\pi - 4\Omega_f(\Theta_c) + 4\Omega_v(\Theta_c) & 90^\circ > \Theta_c > 45^\circ. \end{cases} \quad (5.11)$$

Figure 5.5 shows the value of Ω_c as a function of the critical angle Θ_c . Values of Θ_c for scintillator-oil/Teflon and scintillator-oil/air interfaces are indicated on the figure. Some specific values are:

$$\Omega_c = \begin{cases} 1.35 \text{ sr} & \text{Teflon} \\ 5.63 \text{ sr} & \text{air,} \end{cases}$$

showing that the use of an 'air lining' should increase the light level by a factor of 4.2 over Teflon.

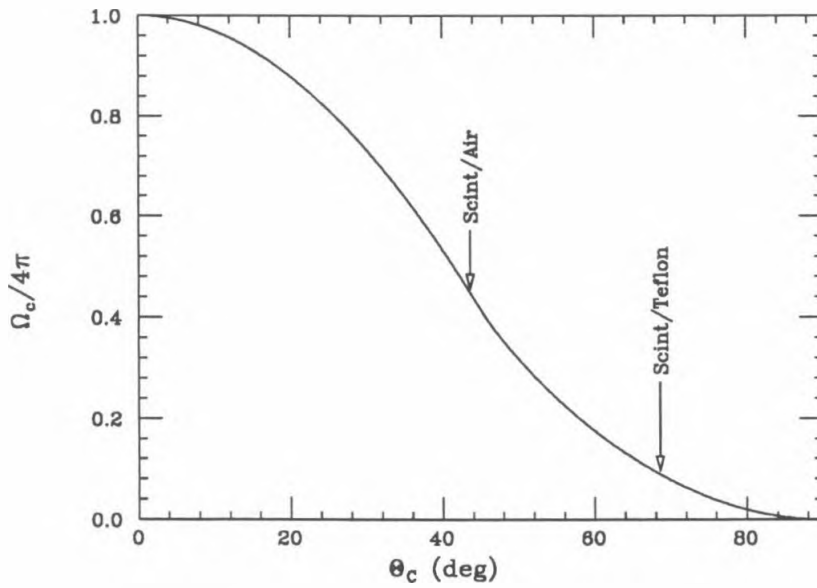


Figure 5.5: Solid angle (as a fraction of 4π) that can propagate by total internal reflection in a rectangular counter with dielectric lining, as a function of the critical angle Θ_c . The values of Θ_c for liquid scintillation counters with air and Teflon linings are shown.

5.5 The Optical Monte Carlo

A Monte Carlo program called OMC2 was developed to study liquid scintillator optics systematically. Appendix A gives details about the program and its capabilities, but a general overview will be given here since the program figures prominently in the rest of this chapter.

The program OMC2 differs from a 'traditional' ray-tracing program in its attention to such issues as scattering, attenuation and timing, which are more characteristic of detector Monte Carlos than of ray-tracing programs. It assumes that the light is in the form of monochromatic 'classical' rays (*i.e.* with continuously variable intensity) rather than photons, and also that the light is unpolarized. Media are either dielectric or metal, and the surfaces are modeled as general quadratic surfaces.

Rays are started with random directions from a light source, propagated through the optical system, and are collected on areas that simulate PMTs. The intensity collected at the PMTs as a fraction of the source intensity is called the 'acceptance' of the optical system, and may be compared to models and to prototype data.

Figure 5.6 shows a response curve for a 50×25 cm counter with a single

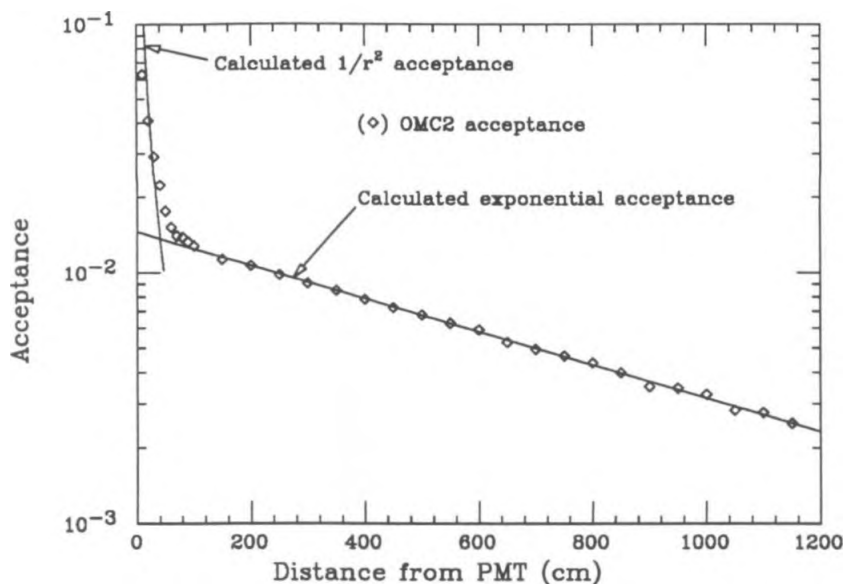


Figure 5.6: Response curve obtained by OMC2 for a Teflon-lined scintillation counter, compared with analytic calculations.

PMT. The straight line shown on the figure is not a fit, but rather a direct calculation from the discussion above. It can be seen that there is excellent agreement between OMC2 and the analytic calculations for the exponential response.

The $1/r^2$ acceptance calculation is also shown and seems not to fit the OMC2 points very well. This is because OMC2 was used with a distributed source of light in order to obtain an average acceptance over the cross section of a counter, while the direct calculation assumes a point source on the centerline. With an appropriate source, there is a better match between

calculation and simulation, but the calculations are slightly inaccurate in the region $z \approx 100$ cm where there is typically 1–2 reflections.

Perhaps the most useful application of OMC2 has been in modeling the effect of different lining materials, and in the examination of light collection mirrors around the PMTs. These applications will be discussed in more detail in the following sections of this chapter.

5.6 End Mirrors and Focussing

One useful application of OMC2 was the simulation of mirrors around the PMTs. The PMTs generally cover only a fraction of the end of large liquid scintillator counters, while the rest of the light striking the end of a counter is lost. One attempts to collect some of the light that would otherwise be lost by using mirrors placed around the PMTs.

There were two distinct situations for the use of mirrors: flat mirrors to reflect light missed by one PMT towards the other end of the counter, and ‘focussing’ mirrors to reflect light into the nearer PMT.

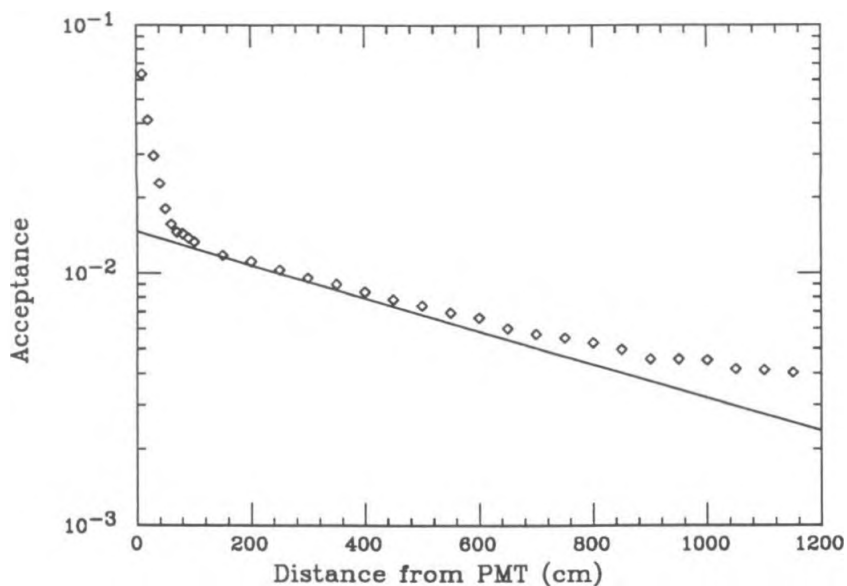


Figure 5.7: Response curve for a counter with flat end mirrors. The data points were calculated by OMC2 for a $50 \times 25 \times 1200$ cm counter with a flat mirror placed around the PMTs. The ‘far end’ response is increased by nearly a factor of two. The response of a counter without such a mirror is shown for reference.

5.6.1 Flat Mirrors

The flat mirrors have the effect of raising the response curve of a counter at the far end, as shown in Figure 5.7.

The difficulty with flat mirrors shows up in the timing of PMT pulses with a flat mirror; a fast particle passing through the counter produces several distinct pulses separated by the light propagation time to the mirror and back (See Figure 5.8). The reflected pulse is close enough in time to increase

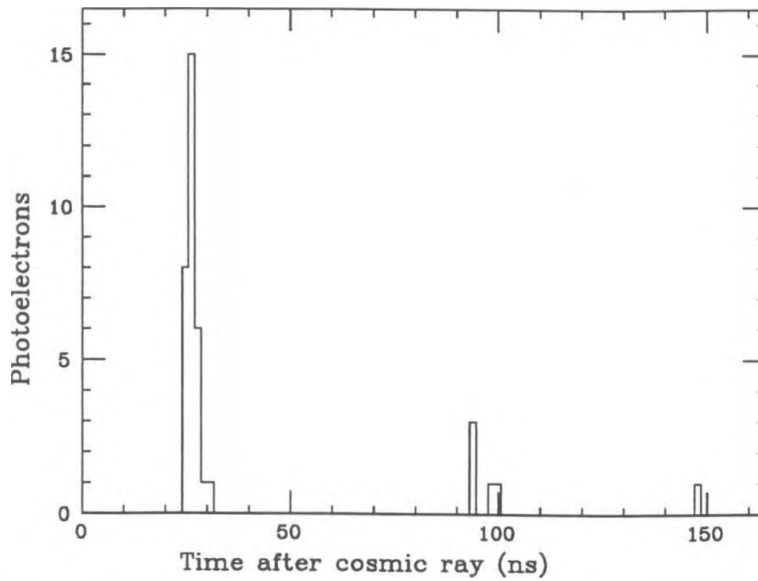


Figure 5.8: Time distribution of photoelectron pulses calculated by OMC2 for a cosmic ray in a counter with flat end mirrors. The cosmic ray was incident at $z = 500$ cm and had a total intensity of 37 photoelectrons. The pulse at $t \approx 25$ ns is direct light from the cosmic ray, and the later pulses are a result of light reflected by the flat end mirrors.

the pulse height of particles that pass through the counter near the far end, but otherwise the extraneous pulses don't help to refine either the timing or pulse height information.

As mentioned in Chapter 4, one of the major problems with background for slow particle recognition came from afterpulses in either the PMT or the scintillator. The time and pulse height distributions of reflected light pulses are more regular than these other sources of afterpulses, and presumably could be removed in offline analysis, but it seems unlikely that a trigger scheme would be able to do so with much efficiency.

Since flat mirrors were found to yield only rather marginal gains and produce serious background problems for slow particle triggers, it was decided that these mirrors should not be given further consideration.

5.6.2 Focussing Mirrors

The focussing mirrors are those which, when placed around a PMT, tend to focus scintillation light onto the PMT. This has the effect of raising the overall light level of a counter, without changing the shape of its exponential response; however, there is some change in the form of the $1/r^2$ response.

It should be noted that the effect of the focussing mirrors depends strongly on the details of the ends of the counters. Without focussing mirrors it was possible to model the PMTs as flat circular apertures with only $\approx 4\%$ error, and the light level could be easily scaled with the dimensions of the counters. This is not the case with focussing mirrors, and so a different approach was required.

A counter was simulated in OMC2, using the configuration of an actual MACRO counter, that is, with an inside width of 73.5 cm and two 8 inch Hamamatsu R1408 PMTs (see Fig. 5.9). The PMTs have a front surface that can be described as an oblate spheroid with 10.2 cm semimajor axes and a 7.5 cm semiminor axis. The purpose of this simulation was not to determine absolute acceptances, which is more easily and accurately done with the simpler models described above, but rather to find the factor by which the acceptance increases, and the changes in the light distribution on the PMT when a focussing mirror is added to the configuration.

A distributed source of rays was used, covering the width and height of the scintillator, 600 cm from the PMT. The distance was chosen to allow the rays propagating down the box to establish an 'equilibrium' angular distribution in θ . The source was restricted so that much of the non-total

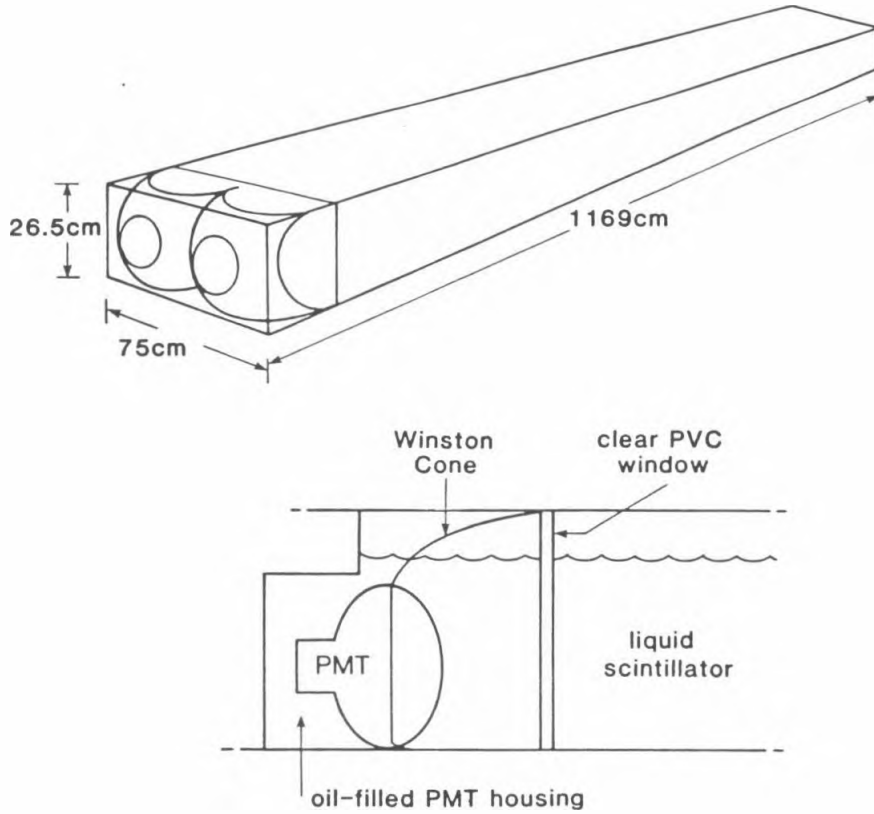


Figure 5.9: Drawing of the MACRO horizontal counters, showing the configuration of PMTs at the ends. These counters use a light focussing cone discussed in the text.

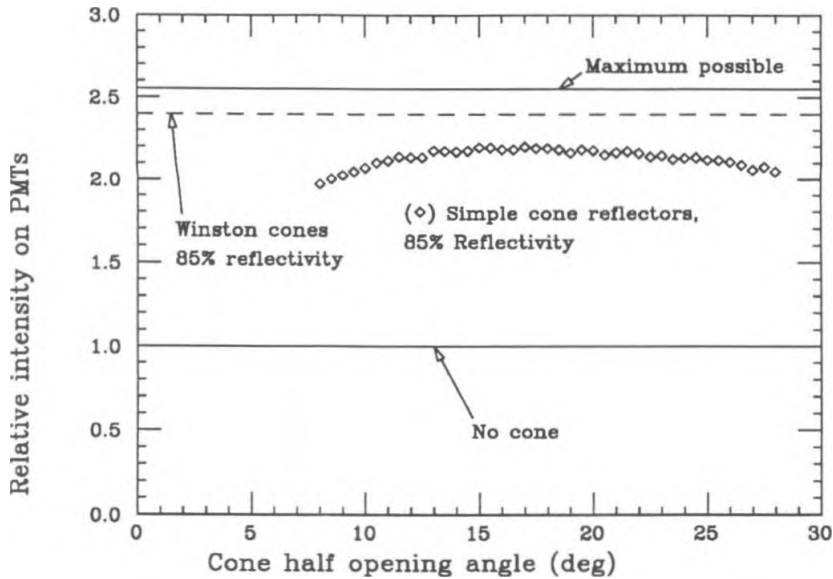


Figure 5.10: Focussing cone intensity comparison. Intensity calculated by OMC2 for PMTs with straight conical reflectors in a MACRO counter, as a function of the cone half opening angle. The reflectors were taken to have 85% reflectivity, and the OMC2 intensity calculations for Winston cones of 85% reflectivity and for a MACRO counter without focussing cones are shown.

internal reflection solid angle was excluded, for the purpose of speeding the simulation.

Figure 5.10 shows the intensity on the PMTs using simple or 'straight' conical mirrors of 85% reflectivity, as a function of cone half-opening angle. Physical constraints on the length of focussing mirrors make cones with larger opening angles more desirable, and it can be seen from the figure that a cone of 25–30° should give a light level increase of ≈ 2.2 times, with only slight

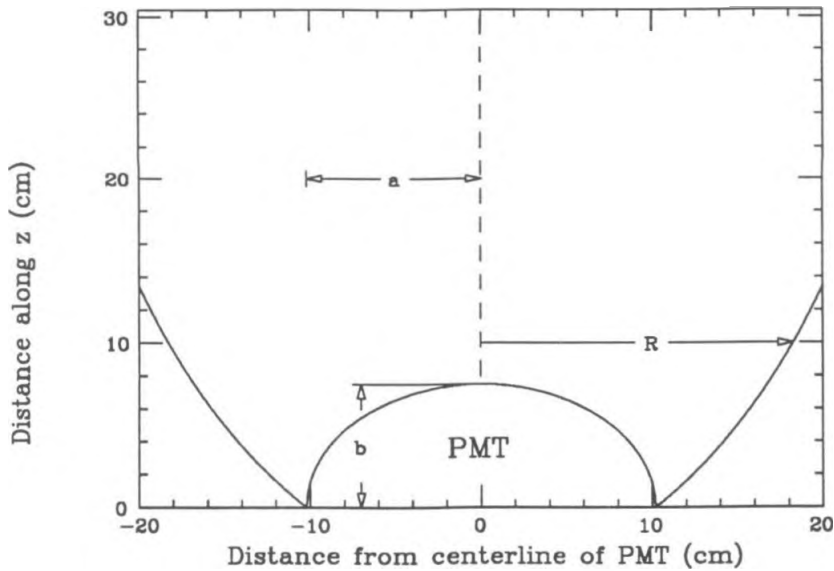


Figure 5.11: Compound parabolic ('Winston' cone) curve calculated for MACRO liquid scintillation counters. The equation for the curve is given in the text. Paraxial rays within $\approx 24^\circ$ of the z axis are focussed on the PMT. The PMT is modeled by a spheroid with semimajor axis $a = 10.2$ cm and semiminor axis $b = 7.5$ cm.

dependence on the opening angle.

Others have studied the methods of such light collection schemes³⁷, and the application of the general principles of nonimaging light collection yields the equation for a compound parabolic reflector ('Winston cone'), which is optimal for paraxial rays. The radius R from the axis of the PMT is given by (See Fig. 5.11)

$$R(z) = \frac{1}{\sin^2 \Theta_c} \left[2\sqrt{f^2 + (z - b)f \sin \Theta_c} - \cos \Theta_c (2f + (z - b) \sin \Theta_c) \right], \quad (5.12)$$

where Θ_c is the critical angle of previous sections, and f is the focal length given by

$$f = \frac{1}{2} \left(a \cos \Theta_c + b \sin \Theta_c + \sqrt{a^2 + b^2} \right), \quad (5.13)$$

and a and b are, respectively, the lengths of the semimajor and semiminor axes of the PMT.

The curve described by Eqn. 5.12 is a quartic (4th order) surface, and so it was not modeled directly in OMC2. Instead, it was approximated by quadratic surfaces within 1 cm slices in z . The error in this approximation was found to be $< 10^{-4}$ cm over the full length of the Winston cone.

An OMC2 simulation of two such cones with PMTs in a MACRO counter showed an increase of light by a factor of 2.40, using a reflectivity of 85% for the cones and the same light source used above for conical mirrors. This is to be compared with a factor of 2.15 for a 23° simple cone, which has the same length as the Winston cone. Although the response improvement of the more complicated surface over that of simple cones is small, they are no more difficult to build, and so this geometry was chosen for use in MACRO

counters.

The distribution of light on the PMTs is shown in Figs. 5.12 and 5.13 in terms of the intensity/area on the PMT face as a function of angle from the z axis. When compared with the distribution of light without a focussing cone, it is seen that the greatest increase in light intensity is at $z \approx 2.5$ cm.

Comparison of the maximum possible collection efficiency for a focussing cone of reflectivity $R = 0.85$,

$$\begin{aligned}\epsilon_{max} &= \frac{A_{pmt} + R(A_{end} - A_{pmt})}{A_{end}} \\ &= 0.903,\end{aligned}$$

with the collection efficiency with no cone

$$\begin{aligned}\epsilon_{min} &= \frac{A_{pmt}}{A_{end}} \\ &= 0.354,\end{aligned}$$

gives a maximum improvement factor of 2.55, which is to be compared with the factor of 2.40 observed with the Winston cone. This improvement factor indicates that the Winston cone is nearly optimal.

The efficiency comparison above also indicates that some of the Monte Carlo calculations may be done with a 'PMT' that covers the entire end of

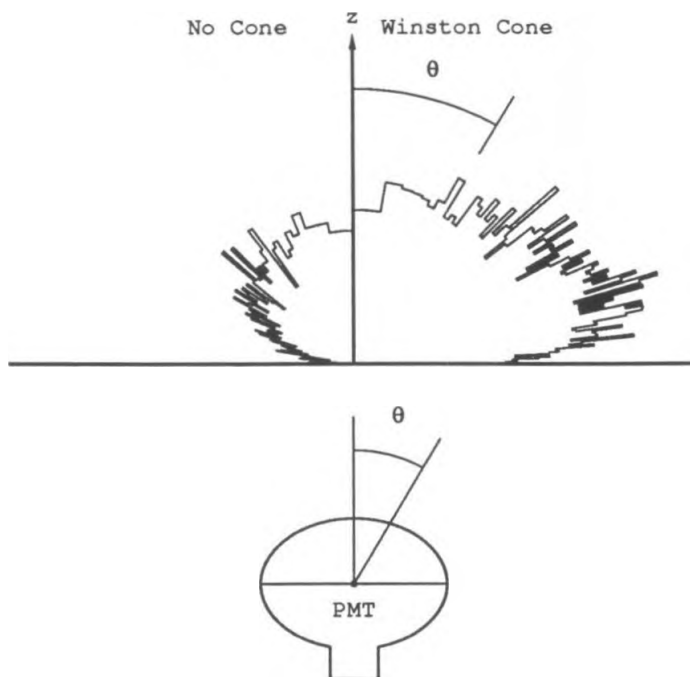


Figure 5.12: Polar plot of the intensity/unit area for a PMT with a Winston cone and without a cone, as a function of angle from the z axis. The data were obtained from OMC2 runs. Note that the largest increase occurs at $\theta \approx 75^\circ$, which corresponds to $z \approx 2.5$ cm from the equator of the PMT.

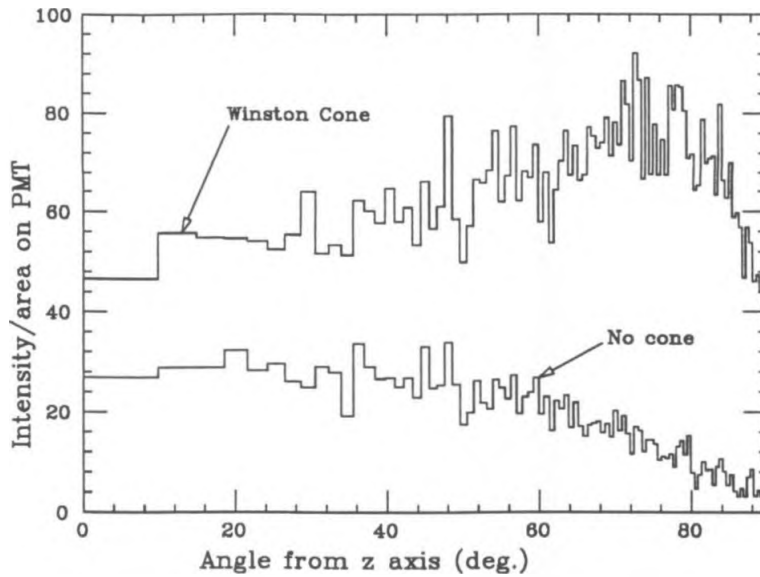


Figure 5.13: Intensity/area on a PMT with and without a Winston cone as a function of the angle θ from the z axis.

the counter. This is very desirable, since OMC2 runs with the Winston cone are quite slow. However, the $1/r^2$ response of a counter and the variations in response over the cross section of a counter must be modeled using the Winston cone, since these cases are sensitive to the details of the optical configuration.

5.7 Lining Materials

There were several different types of lining materials available for the counters. Since each of them has its own peculiarities, they will be dealt with separately. Generally, one has either a dielectric lining of low refractive index that uses total internal reflection, or a reflective metallic lining.

It is also possible to have a dielectric lining with another material behind it, such as Teflon with a reflective aluminum backing. Another such material of interest was white vinyl-backed Teflon, since the vinyl could be modeled as a perfect scatterer.

5.7.1 Dielectric Lining Materials

Dielectric linings may be described by their refractive index, or equivalently by the critical angle Θ_c . The light intensity at a PMT may be expressed by integrating Eqn. 5.4 over the solid angle that is totally reflected.

$$I(z) = \frac{1}{2} f \int_{\text{tot.}}^{\text{tot.}} \frac{dI_S}{d\Omega} \exp\left(-\frac{z}{a_b} \sec \theta\right) d\Omega, \quad (5.14)$$

where f is the area fraction of the end of the counter that is covered by PMTs, and $dI_S/d\Omega$ is the source intensity per unit solid angle. The fraction of 1/2 comes from the fact that half of the totally reflected light propagates in either

direction down the counter. Scintillation light is produced isotropically, so that the equation above becomes

$$I(z) = \frac{1}{2} f \frac{I_S}{4\pi} \int_{\substack{\text{tot.} \\ \text{ref.}}} \exp\left(-\frac{z}{a_b} \sec \theta\right) d\Omega. \quad (5.15)$$

It is now possible to replace the integral above with an effective attenuation length term multiplied by Ω_c , the solid angle that is totally reflected towards one end of the counter, giving an approximation for the intensity at large z

$$I(z) = \frac{f \Omega_c}{2 \cdot 4\pi} I_S e^{-z/a}, \quad (5.16)$$

which is the same as that obtained earlier, where a is an effective attenuation length that has a weak dependence on z .

5.7.2 Metallic Linings

Metallic linings are of interest as a simplified case of Teflon linings with an aluminized backing. These linings may be characterized by their reflectivity R , which for simplicity is assumed not to depend on reflection angle.

The attenuation that results from reflections from the lining may be approximated as:

$$I \sim R^{z/z_r} = \exp(z \ln R/z_r),$$

where z_r is the average distance along the counter between successive reflections from the lining. The distance z_r may also be expressed in terms of an average 'width' of the counter D :

$$z_r = D \cot \theta,$$

where θ is the angle of the ray with respect to the z axis. There is also the attenuation due to the scintillator to be accounted for, which gives

$$\frac{dI}{d\Omega}(z) = f \frac{dI_S}{d\Omega} \exp\left(-\frac{z}{a_b} \sec \theta\right) \exp\left(\frac{z}{D} \ln R \tan \theta\right). \quad (5.17)$$

As a simplifying assumption, we may ignore the attenuation by the medium. The equation above may then be integrated over ϕ ,

$$I(z) = \frac{1}{2} f I_S \int_0^1 \exp\left(-\frac{z}{a_r} \tan \theta\right) d\cos \theta, \quad (5.18)$$

where a_r plays a role similar to attenuation length

$$a_r = -\frac{D}{\ln R} > 0,$$

with the result of

$$I(z) = \frac{1}{2} f I_S \mathcal{F}(z/a_r), \quad (5.19)$$

where the functional dependence has been gathered into \mathcal{F} , given by

$$\mathcal{F}(z/a_r) = 1 - \frac{\pi}{2}(z/a_r) [\mathbf{H}_0(z/a_r) - \mathbf{Y}_0(z/a_r)], \quad (5.20)$$

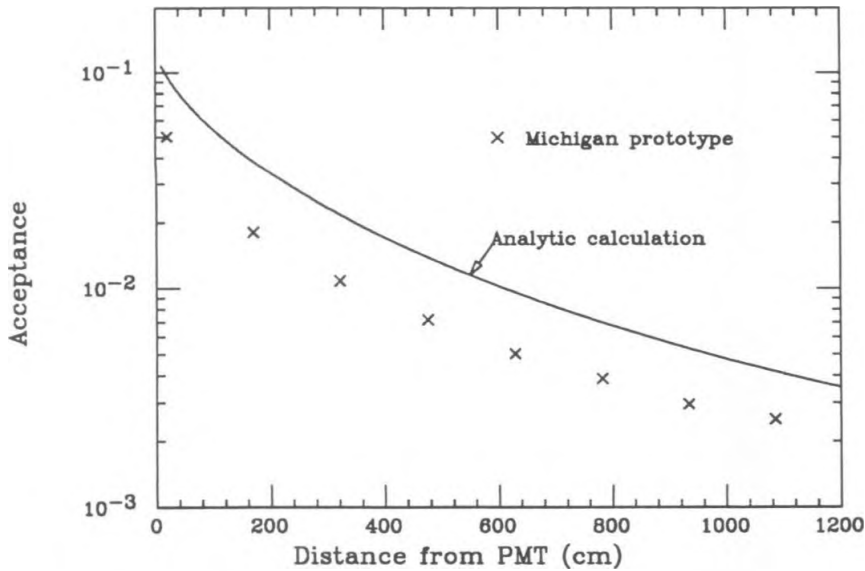


Figure 5.14: Calculated response curve for metallic lining, using values of $R = 0.80$, $D = 50$ cm and $f = 0.251$, typical of the prototypes. Attenuation by the scintillator is not included in the calculation. Response measurements from a counter lined with aluminum-backed Teflon is shown for comparison on an arbitrary vertical scale.

where H_0 is a Struve function, and Y_0 is a Bessel function of the 2nd kind. This parameterization makes the shape of the response depend on a single scale length.

Figure 5.14 shows a response curve calculated from the equations above. While it is smooth and appears to have much the same shape as the measured response curve, this is partially accidental. The effects both of a Teflon over the metallic lining and of attenuation length tend to cancel at $z \gtrsim 800$ cm.

At smaller z , the response curve of the prototype data is reasonably well modeled by a metallic lining, and the equations above may be useful in examining these counters.

Including the effect of bulk attenuation makes the calculations much more difficult, and it is necessary to use numerical integration of Eqn. 5.17. Metallic linings are clearly inferior to Teflon linings with a metallic backing, and so metallic linings were not considered for prototype tests. The calculations above are thus most useful as a limiting case for the aluminum-backed Teflon lining.

5.7.3 Aluminum-Backed Teflon

The analysis of this lining begins with the general equation used above to describe metallic linings. The effect of the Teflon will be to make the reflectivity of the lining unity when total internal reflection is achieved.

$$I(z) = f \frac{I_S}{4\pi} \int_0^1 d\cos\theta \exp\left(-\frac{z}{a} \sec\theta\right) \int_0^{2\pi} d\phi \exp\left(\frac{z}{d} \ln R(\theta, \phi) \tan\theta\right) \quad (5.21)$$

Figure 5.15 shows an 'average' reflectivity with $R = 0.80$ for the aluminum, where a numerical integration over ϕ has been done. The reflectivity at large θ is increased by the $\approx 4\%$ reflectivity of the Teflon at normal incidence.

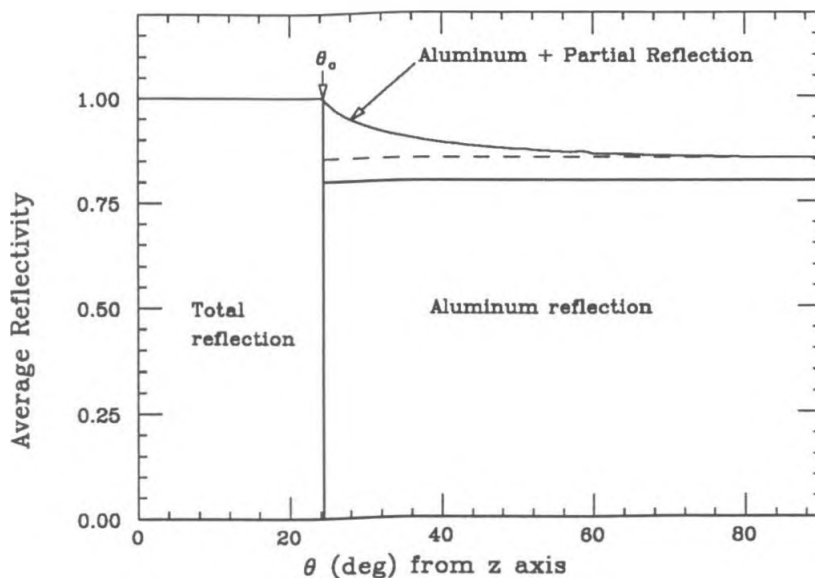


Figure 5.15: Average reflectivity of an aluminized Teflon lining for light propagating down a counter with angle θ to the z axis. Light with $\theta < \theta_c$ is totally reflected from the Teflon. A reflectivity of 80% has been assumed for the aluminum.

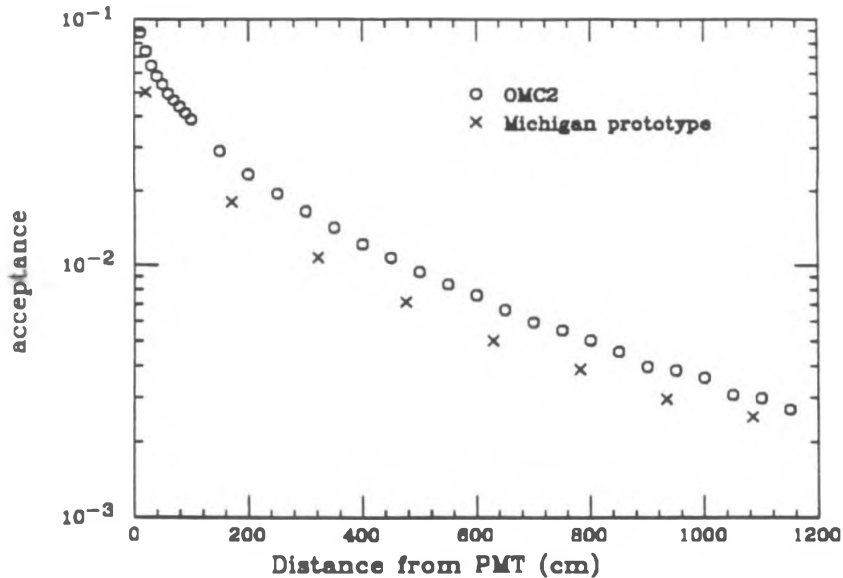


Figure 5.16: Response curve of a scintillation counter with an aluminized Teflon lining, generated by OMC2. The response of the Michigan prototype, which has such a lining, is shown for comparison on an arbitrary vertical scale.

The expression above for the response is complicated enough that it is best evaluated by Monte Carlo methods, since the reflectivity depends on the angles θ and ϕ in a complex manner. Figure 5.16 shows the response curve produced by OMC2 for aluminum-backed Teflon, using 80% reflectivity for the aluminum and a bulk attenuation length of 7 m. The figure also shows some data points (on an arbitrary intensity scale) taken on the Michigan prototype counter³⁸, which has an aluminum-backed Teflon lining. While it is difficult to see if there is an exact match between the two, it can be seen

that the OMC2 data have a similar shape as that from the prototype.

The reflective backing increases the amount of light from the far side of the counter by only about 7%, while light from the near side (where there is already plenty of light) is greatly increased.

While it is generally desirable to have more light from a counter, the increased dynamic range of counters lined with aluminum-backed Teflon can cause problems in the instrumentation. For example, it is difficult to discriminate against radioactivity in a 10 MeV neutrino trigger, when the signal from a 1 MeV decay varies by a factor of ≈ 20 from one end of the counter to the other.

5.7.4 Vinyl-Backed Teflon

It was found that a Teflon film with a white vinyl backing was both economical and easily applied as a scintillation counter lining. The Teflon determines most of the optical properties; however, the light that is not totally reflected by the lining can be scattered by the vinyl backing. Since the scattering takes place outside the scintillator, it cannot give light that will be propagated by total reflection.

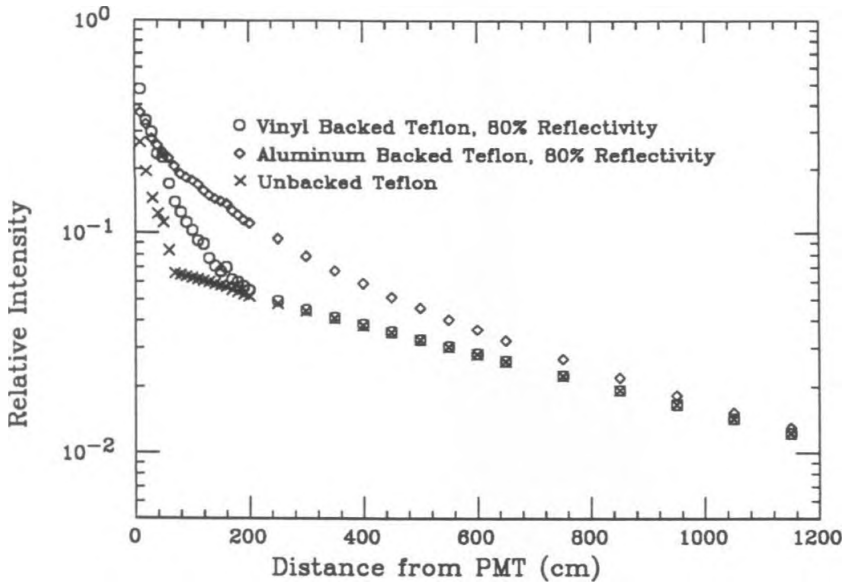


Figure 5.17: Comparison of response curves (generated by OMC2) for a MACRO counter with several different linings. Winston cones were simulated by making the PMT acceptance cover the ends of the counters. There is very little difference between the vinyl-backed Teflon and unbacked Teflon at $z > 200$ cm.

Direct calculation of this effect is more difficult than with an aluminum backing, but it is amenable to Monte Carlo simulation. Figure 5.17 shows a response curve generated with a simulated MACRO counter with a vinyl-backed Teflon lining. The vinyl is assumed to be a diffuse scatterer with 80% reflectivity. The effect of Winston focussing cones on the PMTs was simulated by making the full end of the counter accept light. A curve with unbacked Teflon lining is also shown, as well as a curve generated with 80%

specular reflection, as from aluminum-backed Teflon.

The effect of the vinyl scattering is small at distances greater than about 2 m. The vinyl backing thus increases the response of the counters in the first meter or two, but when wavelength dependence (discussed below) and other small z effects are included, this increase is probably not noticeable.

5.7.5 The Effect of Wrinkles

Differences in light output of two prototype counters caused the question of whether small wrinkles in the liner material could appreciably affect the light output of a counter. It was understood that a liner with a reflective backing should be mostly immune to such effects since it would still have considerably reflectivity outside of total reflection, but an unbacked liner would lose any ray that hit a wrinkle and was reflected outside the critical angle.

This effect was studied with OMC2 by applying a random variation of the surface normal to simulate a surface with wrinkles. Thus, every ray reflected from a wrinkled surface had a random 'wrinkle vector' added to the surface normal. This behaves like a microscopically wrinkled surface, where there is no correlation of the surface normals with position. The distribution of

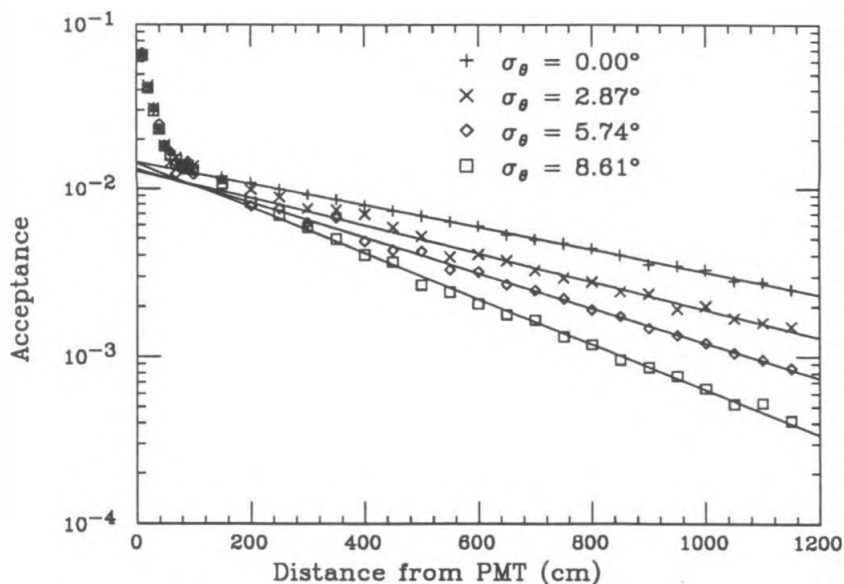


Figure 5.18: Response curves generated by OMC2 for a counter with a wrinkled Teflon lining, with several values of the ‘wrinkledness’ σ_θ . Exponential fits to the curves are shown. It can be seen that the primary effect of the wrinkles is to reduce the attenuation length.

wrinkle vector components was taken to be Gaussian along each axis in the surface, and σ_θ denotes the standard deviation of the Gaussians, in degrees from the normal, as the parameter that describes how wrinkled the surface was.

Figure 5.18 shows the response curves that were generated by OMC2 with several values of σ_θ . There is little difference for $z < 100$ cm, since most of the light from sources this close doesn’t reflect from the walls. It shows that the primary effect of the wrinkles is to reduce the attenuation length.

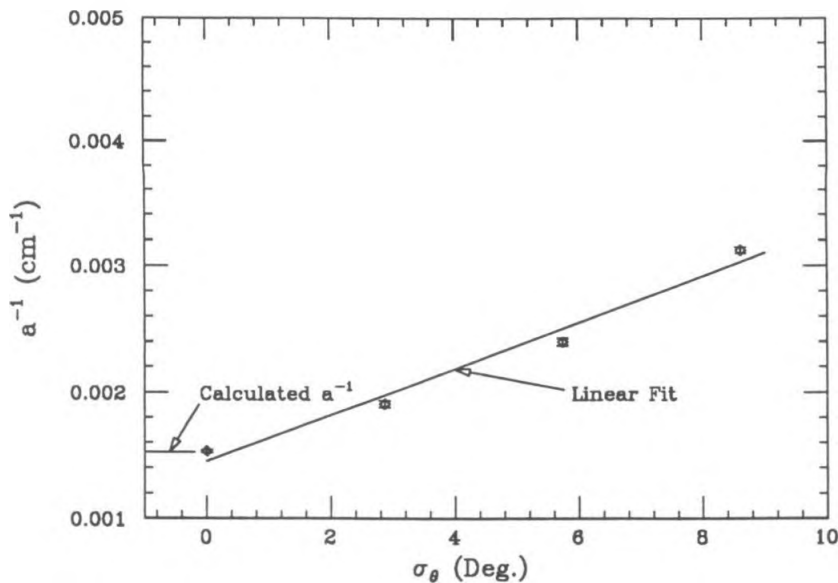


Figure 5.19: Values of the attenuation (1/attenuation length) from fits of wrinkled Teflon response curves. The attenuation increases with the degree of wrinkling. The calculated attenuation for an unwrinkled Teflon lining is shown. Error bars are from the fits.

When the response curves are fitted with exponentials, the fitted attenuation lengths and acceptances may be examined as a function of σ_θ (See Figures 5.19 and 5.20). Linear regression shows that the effect of wrinkles on the light level is $\lesssim 10\%$, even when the wrinkles decrease the attenuation length substantially.

Measurements made on the Caltech counter prototype constructed with a loose Teflon lining (and an abundance of wrinkles) showed an attenuation length of 5.3 m, indicating that wrinkles in the lining are only a minor con-

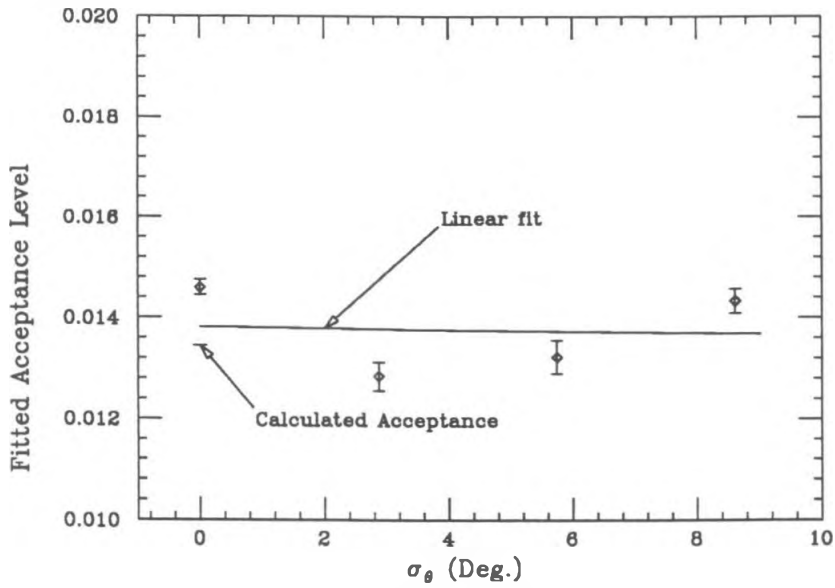


Figure 5.20: Values of the acceptance level from fits of wrinkled Teflon response curves. The calculated value for unwrinkled Teflon is shown. The data show no dependence of acceptance (equivalent to light level here) on the amount of wrinkling in the lining. Errors are from the fits.

cern for the attenuation length. After this counter was relined with a very smooth Teflon lining (among other improvements), it showed a *decrease* in attenuation length, which has since been traced to wavelength-dependent effects (see Section 5.9 below). So far, the ‘wrinkledness’ of prototype linings have shown no definite effect on either the attenuation length or the light level.

5.8 Timing

The MACRO counters need to have good timing accuracy for fast particles, so that the time-of-flight between two counters may be used to determine the direction in which the particle was moving. This capability is particularly important for the separation of up- and downgoing muons, since there are $\sim 10^4$ times as many downgoing cosmic ray muons as there are upgoing muons induced by neutrino interactions in the rock around the MACRO detector.

For counters separated by the 4–5 m between MACRO horizontal planes, the time-of-flight of a relativistic particle is 13–17 ns, and hence the separation between up- and downgoing muons is 26–34 ns. Only a small fraction

of misidentified downgoing muon flux is enough to contaminate the upgoing events, and so it is useful to see how much the optics contributes to the timing jitter of the counters.

Triggers that have been designed for slow particle detection^{39,40} use the characteristic pulse shape of a slow particle passing through a counter as a means of discriminating against background. The pulse shape from these counters has contributions from both the optics and the electronics; the optical pulse shape will be examined here, and some characteristic pulse shapes will be calculated for different counter lining materials.

5.8.1 Optical Pulse Shape

The time distribution of light at the PMTs (optical pulse shape) may be examined analytically in the case of dielectric or metallic linings. A ray from a source of light at a distance z from the PMT, emitted at $t = 0$, will have photons arrive at the PMT at time

$$t = \frac{zn}{c} \sec \theta, \quad (5.22)$$

where θ is the angle of the ray with respect to the z axis, and n is the refractive index of the oil. This allows the integrals over solid angle for light

intensity to be used for obtaining pulse shapes. Thus, for a dielectric lining

$$I = \frac{1}{2} f \int_{\text{res.}} \frac{dI_S}{d\Omega} \exp\left(-\frac{z}{a_b} \sec \theta\right) d\Omega = f \frac{I_S}{4\pi} \int_L^1 A(\theta) \exp\left(-\frac{z}{a_b} \sec \theta\right) d\cos \theta, \quad (5.23)$$

where

$$L = \begin{cases} \sqrt{-\cos 2\Theta_c} & \Theta_c > 45^\circ \\ 0 & \Theta_c < 45^\circ \end{cases}$$

and $A(\theta)$ is the remnant of the integral over ϕ :

$$A(\theta) = \begin{cases} 2\pi & 1 > \cos \theta > \sin \Theta_c \\ 2\pi - 8\sqrt{1 - \frac{\cos^2 \Theta_c}{\sin^2 \theta}} & \sin \Theta_c > \cos \theta > L. \end{cases}$$

When this is made into a timing distribution, one obtains

$$dI(t) = f \frac{I_S n z}{4\pi c t^2} A[\theta(t)] \exp\left(-\frac{tc}{na_b}\right) dt, \quad (5.24)$$

which agrees with photon timing from OMC2 as shown in Fig. 5.21.

For metallic linings, the integral is over the entire solid angle, and there is an extra term from the reflectivity of the lining (see previous section):

$$dI(t) = f I_S \frac{nz}{ct^2} \exp\left(-\frac{tc}{na_b} - \frac{\sqrt{t^2 c^2 - z^2 n^2}}{a_r n}\right) dt. \quad (5.25)$$

Figure 5.22 shows the optical pulse shapes obtained from these equations for Teflon, air, and metallic linings (85% reflectivity, $D = 50$ cm) at $z = 600$ cm.

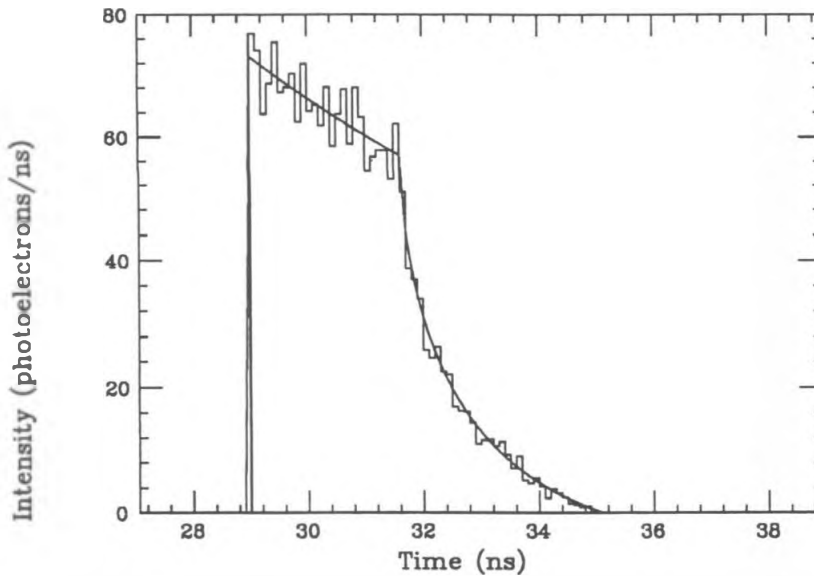


Figure 5.21: Time distribution of light calculated analytically, compared with OMC2 data for the same optical configuration.

Notice that while the air lining has considerably more light, the width of the light pulse is quite large. Both the air and the metallic linings have long ‘tails’ in their pulses, which have a considerable fraction of their total light. An aluminized-Teflon curve was not calculated directly, but can be approximated as the maximum of the Teflon and the metallic curves in each time bin. This indicates that aluminized Teflon will have the same ‘prompt light’ characteristics as Teflon linings, but also has tails on the pulses with about 1/3–1/4 of the total light, from metallic reflection.

The pulse shapes obtained so far are from a point source with a delta-

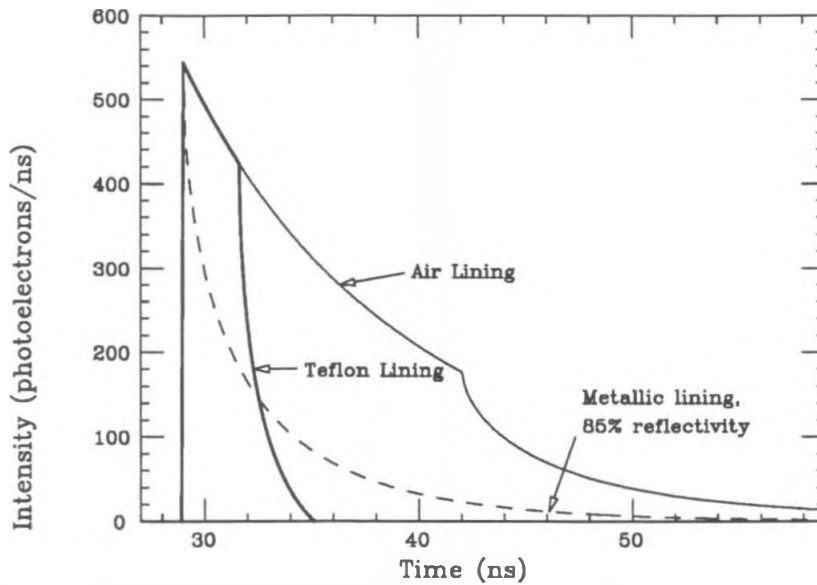


Figure 5.22: Calculated time distributions of light from a source at $z = 600$ cm from the PMTs for various counter linings. The intensities have been scaled to the expected MACRO counter response to a minimum ionizing particle at this distance. It can be seen that air and metallic linings have tails on their optical pulses.

function in intensity at $t = 0$. A pulse from an actual cosmic ray will be smeared by the transit time of the cosmic ray through the counter (~ 1 ns for $\beta = 1$), and also have smearing due to the PMT and other electronics. This will have the effect of smoothing the pulses over time scales of 5–10 ns, but the slow decay of the light tails will still remain. Such pulse tails could cause problems for slow particle triggers that use pulse shape to distinguish a slow particle from a fast cosmic ray particle.

5.8.2 Timing Jitter

This is one instance where it is necessary to distinguish between the ‘classical’ rays that have been used in the Monte Carlo and ‘photons,’ since photon statistics are needed for timing jitter calculations. The intensity of the classical rays may be used as probability amplitudes for the photons, however, and Poisson statistics applied.

If we take dI/dt to be in terms of photoelectrons per unit time, then the probability of the first photoelectron of the pulse arriving between t and $t + dt$ is

$$P^{first}(t) dt = \frac{dI}{dt}(t) \exp\left(-\int_{-\infty}^t \frac{dI}{dt}(t') dt'\right) dt. \quad (5.26)$$

The width of the probability distribution above is a measure of the timing jitter contributed by the optics. The timing jitter decreases very quickly with increasing light intensity, and the jitter from the optical pulses calculated above (with intensities scaled to match prototype data) is negligibly small.

The scintillation light from a cosmic ray is spread out over its transit time through the counter. The timing jitter from a typical cosmic ray was obtained by examining the ‘intensity vs. time’ histogram shown in Fig. 5.23, where the rays were produced along simulated $\beta = 1$ particle tracks at $z = 600$ cm

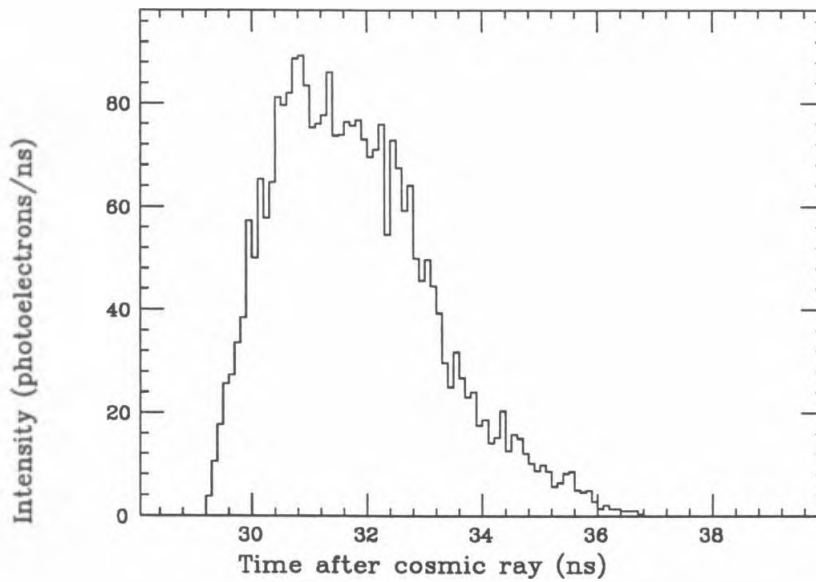


Figure 5.23: Time distribution of light from a $\beta = 1$ cosmic ray at $z = 600$ cm simulated by OMC2. This was then normalized to make a probability distribution for photon arrival times.

from the PMT. This histogram was normalized and used as a probability distribution for calculating photon arrival times.

From this distribution and μ , the mean number of photoelectrons for a minimum ionizing particle at the distance z , the probability distribution of the first photoelectron arriving in timing bin k was calculated (like the probability function above)

$$P_k^{\text{first}} = (1 - e^{-\mu p_k}) \exp\left(-\mu \sum_{j=1}^{k-1} p_j\right), \quad (5.27)$$

where p_j is the the probability of a photoelectron arriving in timing bin j obtained from the Monte Carlo histogram. Poisson statistics has been assumed. Figure 5.24 shows the resulting distribution using a value of $\mu = 30$; the standard deviation of the distribution is about 670 ps.

There is also timing jitter because of electron transit time variations in the PMTs. This jitter is typically ~ 1 ns and seems to be the dominant source of timing jitter. Figure 5.25³² shows timing measurements made with the liquid scintillator prototype at Caltech. These were taken with approximately 85 photoelectrons for a cosmic ray muon. Direct calculation indicates that the optics contributes a small amount of timing jitter compared with the other sources, as long as the intensity of the source is sufficiently large.

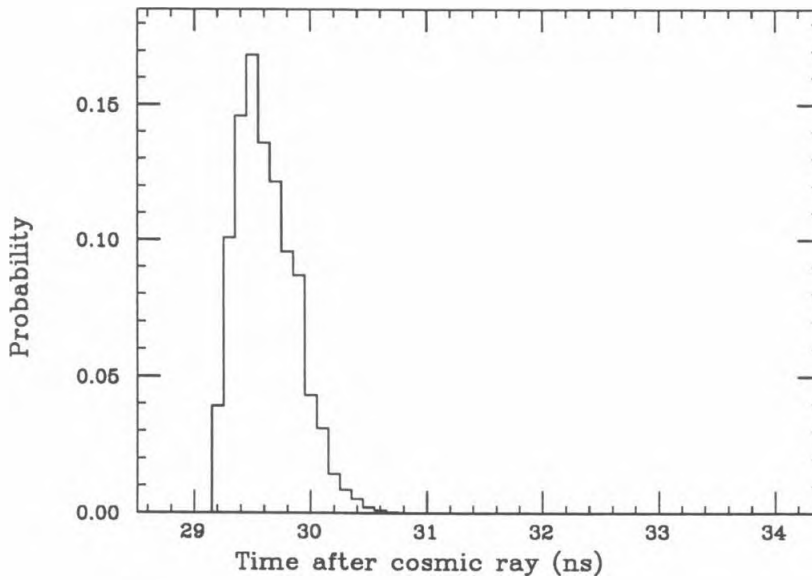


Figure 5.24: Time of first photoelectron calculated from the previous time distribution, with $\mu = 30$ photoelectrons mean intensity. The width of this distribution is indicative of the optical timing jitter.

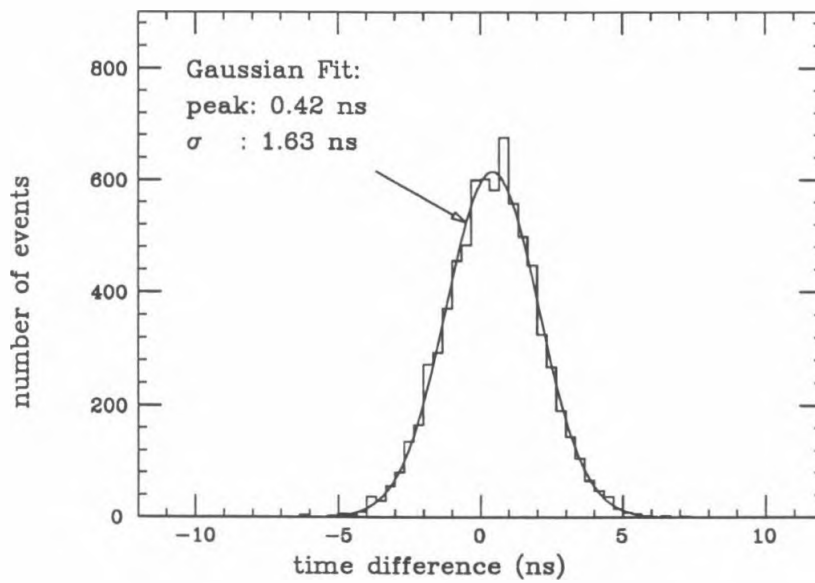


Figure 5.25: Time difference between PMTs at either end of the liquid scintillator prototype at Caltech for cosmic rays in the center of the counter. The width of the distribution gives the time jitter.

5.9 Wavelength Dependence

Response measurements taken with the liquid scintillator prototype show a ' $1/r^2$ ' feature out to distances several times larger than the calculations or Monte Carlos can account for. It was suggested that this could be due to wavelength-dependent attenuation of the scintillation light, and this hypothesis has been found to be correct.

Some of the attenuation length differences observed between different counters, and between our prototype counter with different window materials, have also been attributed to wavelength-dependent attenuation in the commercial scintillator oil that was used in the prototype.

While the 'light level' measurements have the attenuation length effects removed, the wavelength-dependent transmission of the windows that were used in the early tests had the effect of lowering the light level by about 20% and increasing the measured attenuation length. This was due to the removal of short wavelength components (with shorter attenuation lengths) in the scintillation light. When the windows were replaced, it was found that the light level was improved, but the attenuation length was significantly decreased.

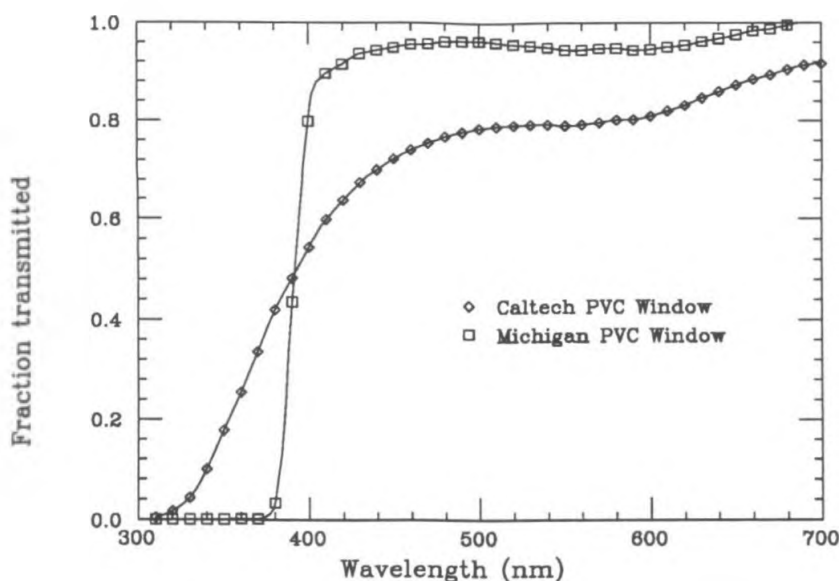


Figure 5.26: Transmission of PVC windows used on Caltech and Michigan prototypes as a function of wavelength. The Caltech PVC windows were later replaced with acrylic windows of much better transparency.

5.9.1 Window Materials

The original liquid scintillator counter at Caltech used hemispherical PVC windows in front of the PMTs. These windows had a blueish cast to them, and were found to have rather poor transmission of blue light. A prototype counter constructed later at the University of Michigan used a different type of PVC windows that were considerably more transparent.

Figure 5.26 shows curves of the transmission of the two window materials as a function of wavelength. The data have been corrected for the air-plastic

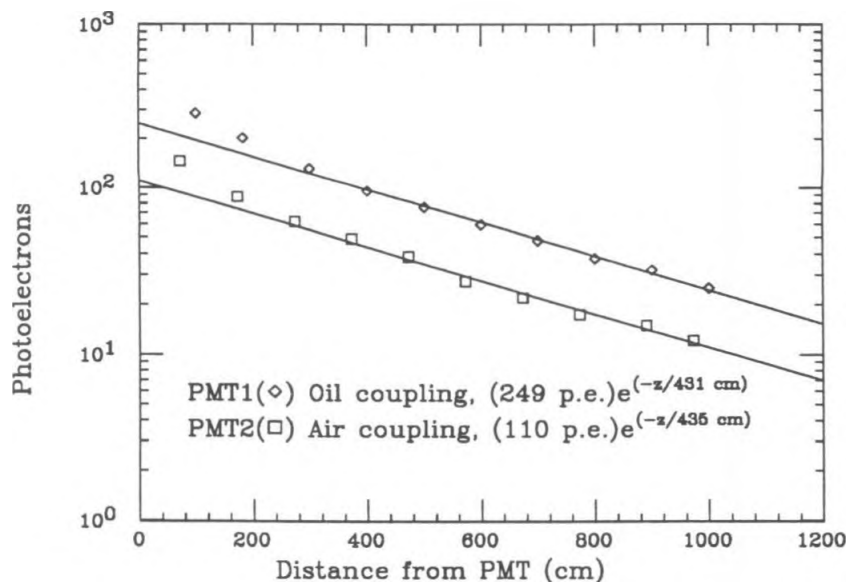


Figure 5.27: Response curves for liquid scintillator prototype with clear acrylic windows. Exponential fits to the data are shown.

interfaces. Blue scintillation light was attenuated preferentially, increasing the average wavelength to which the PMTs responded. This decreased the overall light level, but since the attenuation length increases with wavelength, the measured attenuation length was increased.

The early PVC windows on the Caltech prototype were replaced with acrylic windows before the counter was shipped to Italy. The acrylic windows were considerably more transparent ($\approx 95\%$ transmission) with a cutoff in the blue at about 340 nm. Measurements taken with these windows (see Fig. 5.27) showed a higher light level with a shorter attenuation length.

The figure also shows the effect of using an oil-filled PMT housing to achieve better optical coupling of the PMT to the scintillator. There is an improvement of a factor of ≈ 2.3 in the light level over a configuration in which there is air between the PMT and the scintillator.

5.9.2 Bulk Attenuation

The short attenuation length of the prototype counter with acrylic windows prompted an examination of the attenuation properties of the scintillator. The results of these measurements⁴¹ indicated that the Bicron scintillator used in the prototype had an inferior bulk attenuation length compared to that of the scintillator used in the Michigan prototype. This was not noticed originally, because of the effect of the 'blueish' PVC window, mentioned above.

The differences between the various prototype configurations were not laid to rest until the bulk attenuation length measurements were done, since measurements in the counters could not separate attenuation due to the scintillator and that due to the lining. It now seems that the lining has little effect on the attenuation length in Teflon-lined counters, while large

variations in attenuation length are found between different scintillator oils.

5.10 Prototype Results

It should now be possible to apply some of the matters discussed above to the prototype measurements.

A numerical calculation shows that the ratio of aluminum-backed Teflon to non-backed Teflon response curves,

$$\frac{I_{Al+Teflon}(z; a_b, a_r)}{I_{Teflon}(z; a_b)},$$

is only weakly dependent on a_b , the bulk attenuation length. This allows one to adjust the response curve obtained on the Michigan prototype, in order to see what its response curve would look like without the aluminum backing. It should be noted that the attenuation length observed on the corrected curve may have considerable error, but the light level should still be accurate to $\approx 20\%$.

Figure 5.28 shows the results of this correction procedure, where 80% reflectivity of the aluminum backing has been used. The exponential response of the resulting curve indicates that the reflectivity is approximately correct.

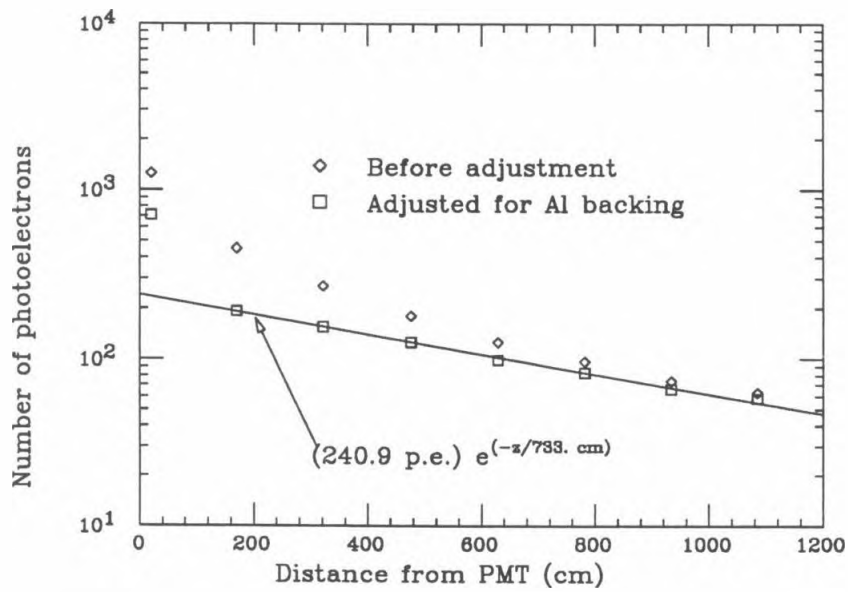


Figure 5.28: Response curve from the Michigan prototype, corrected for aluminized Teflon lining. An exponential fit of the resulting response curve is shown.

The light level obtained from this curve is in good agreement with those measured on the prototype in Italy (see Fig. 5.27).

The light level of ≈ 250 photoelectrons for a single 8 inch PMT in a 25×50 cm counter can be used to obtain the source intensities for minimum ionizing cosmic rays. Using the solid angles and factors mentioned above,

$$I_S = 1.85 \times 10^4 \text{ p.e.}$$

for a vertically incident minimum ionizing particle through 25 cm of scintillator. This gives a source intensity of 740 p.e./cm for a minimum ionizing particle, or (using 2 MeV/cm for the stopping power in oil) 370 p.e./MeV.

This may also be used to estimate the scintillation efficiency, since one may assume 3 eV per ultraviolet primary scintillation photon. When the $\approx 20\%$ quantum efficiency of the PMTs and the window transmission factors are included, this gives an estimated scintillation efficiency of 0.6%, which is reasonable for this low pulse height liquid scintillator. The estimated light yield of this liquid scintillator is then $\approx 1/5$ that of NE-110.

5.11 MACRO Counters

A number of different techniques were combined, trying to use the best points from each, in producing a design for MACRO counters. Some of the results of these optimizations were mentioned previously in this chapter.

The MACRO counter lining was done with vinyl-backed Teflon, avoiding the large PMT signal range of aluminized Teflon and having major advantages in ease of application and cost. Possible difficulties with tails on the light pulses from aluminum-backed Teflon linings were not a factor in this decision, although it can now be seen that such linings could cause problems for triggers.

The scintillation oil will be formulated in the same way as that used in the Michigan prototype, giving long attenuation lengths with good light output. The large differences in attenuation length that have been seen for scintillators that are superficially identical show that a great deal of care is required in the selection of mineral oil for the scintillator.

Winston cones are used around the PMTs at either end of the counters to improve the light collection. Both the cones and the PMTs are immersed in mineral oil for good optical coupling, and separated from the scintillator

by a window of clear PVC like that used on the Michigan prototype.

This chapter would not be complete without an estimation of the light level of a MACRO scintillation counter. So far, no light measurements have been made on a complete MACRO counter, so the calculations are necessarily a bit rough. It is difficult to do more than guess at the attenuation length of a completed counter, since it depends critically on the scintillation oil. One can make a rough estimate of 6 meters for the attenuation length and can hope that the proper selection of mineral oil for the scintillator will improve this.

Extrapolating the light level measurements made on the Caltech prototype is more straightforward, since it's primarily the effect of different counter dimensions and the use of Winston cones, which must be accounted for. Using the results in this chapter, a large z response estimate is obtained:

$$I(z) = (850 \text{ p.e.})e^{-z/(600 \text{ cm})}, \quad (5.28)$$

for a minimum ionizing particle passing through a MACRO counter vertically. A $\pm 10\%$ error in the light level is likely due to details of the window transmission, Winston cone reflectivity, and other unknown factors.

This light level is impressive when compared to the early measurements

on the prototypes and should be more than sufficient for accurate timing and pulse height information. With ≈ 100 photoelectrons at the far end of the counter, the detection of slow particles of ionization as low as 0.1 minimum should be efficient.

5.12 Response to Magnetic Monopoles

The results from previous chapters can be applied to the MACRO liquid scintillation counters to estimate the detectability of magnetic monopoles. Other components of MACRO affect the detection abilities as well; the information from streamer tubes and track-etch detectors would be included in a real situation. The primary concern here is to examine the detection ability of the liquid scintillator counters when considered in isolation from the other detector elements.

Applying the low-velocity scintillation results, one may then calculate the photoelectron rate for a monopole penetrating a MACRO counter at a velocity $1.5 \times 10^{-3} \gtrsim \beta \gtrsim 2.5 \times 10^{-4}$,

$$\frac{dI}{dt}(z) \approx (1.0 \text{ p.e./ns}) \left(\frac{\beta}{10^{-3}} \right)^{2.8} e^{-z/a}. \quad (5.29)$$

It is assumed here that since protons seem not to have a threshold in their

scintillation efficiency, the same should hold for monopoles. Again, because it is based on 'minimum' figures from Chapter 2, this should be taken as a lower limit estimate and should have validity for β down to $\approx 3 \times 10^{-4}$.

The existing trigger circuits that have been designed for these counters^{39,40} should be able to trigger efficiently on a signal of this magnitude down to $\beta \approx 4 \times 10^{-4}$ with 1 photoelectron/100 ns at the far end of a counter.

Since the trigger sensitivity limitations are determined by the acceptable false trigger rate, it is difficult at this point to estimate the lowest β for which the monopole trigger circuits will be able to respond. It is likely that efficient detection of Dirac-charged monopoles down to $10^{-4} c$ is possible.

5.13 Conclusions

The examination of differences between liquid scintillation prototypes has prompted the calculations and simulations that have been presented here. Many of the details of this process of examination have been omitted here; once the cause of a phenomenon is known, the process by which it was found is mostly uninteresting. However, in tracking down these effects, much has been learned about how to improve the design of large liquid scintillator

counters, and this knowledge was then applied to the design of MACRO counters.

The completed MACRO detector will have an outstanding ability to identify GUT monopoles and the size needed to search for them at fluxes below the Parker Bound. A substantial part of this capability is due to the liquid scintillator counters, which have been the subject of this chapter.

Chapter 6

Conclusions

This thesis presents an evolution in the methods of detection of GUT monopoles.

The GUT monopole is unlike the 'usual' elementary particles, in that it is both slow and highly penetrating. This posed a serious problem to those searching for monopoles, since it was uncertain whether existing detection techniques were sensitive to slow particles. The low β scintillation experiment demonstrated that slow particles could be detected in scintillator, and paved the way for large monopole detectors such as MACRO.

The experience gained by operating smaller monopole detectors was invaluable when the design of large detectors was considered. The desire for

an underground location, closed geometry, and a coincidence of many detector elements was a result of this experience. The analysis of the prototype monopole detector indicated the need for maximizing the scintillator light output, so that monopole signals would be clear and unambiguous.

The MACRO counters were examined with this goal in mind, and the tests and calculations have resulted in an improvement of the MACRO counter response and a better understanding of the counters in general. There is now considerable confidence that MACRO will be able to place new lower limits on the flux of magnetic monopoles in cosmic rays, or that the signature of a monopole candidate will be clear enough to firmly establish a flux.

Appendix A

The Optical Monte Carlo

The development of a Monte Carlo program to simulate the optics of a scintillator counter was motivated by a desire to study systematically the effects of changes in the optical configuration. It is possible to do this by means of prototypes, but for a 12 m long prototype the difficulty of varying a major component, such as relining with a different material for example, is prohibitive. There are other effects that are quite difficult to study systematically in a prototype, such as the effects of wrinkles in reflecting surfaces, and these are natural candidates for Monte Carlo simulation.

A ray-tracing program (OMC2) was developed for these purposes, which was intended to avoid problems found in other such programs, and which

was more flexible in its optical configurations.

The surfaces used in the program were modeled as general quadratic surfaces, which include most surfaces of interest optically. For simulating scintillator counters it was found that planes, spheres, and the occasional cone and oblate spheroid (for an accurate PMT shape) would cover most of the cases of interest.

Options were included in the program for turning off rays generated by partial reflection and refraction, so that the ray-tracing process may be faster when these rays are not of interest. Bulk attenuation by the medium is included by degrading the intensity of the ray, and the propagation time is also kept for each ray.

A.1 Description of a Surface

An optical configuration consists of different media with interfaces between them. Since most of the optics is in the interfaces, the volumes of the media are described in terms of the surfaces between them.

The surfaces are modeled with general quadratic surfaces, which may be

represented in the form

$$f(x, y, z) = a_{xx}x^2 + a_{yy}y^2 + a_{zz}z^2 + a_{xy}xy + a_{xz}xz + a_{yz}yz + a_x x + a_y y + a_z z + a = 0,$$

or more conveniently as

$$f(x, y, z) = [x, y, z, 1] \begin{bmatrix} a_{xx} & \frac{1}{2}a_{xy} & \frac{1}{2}a_{xz} & \frac{1}{2}a_x \\ \frac{1}{2}a_{xy} & a_{yy} & \frac{1}{2}a_{yz} & \frac{1}{2}a_y \\ \frac{1}{2}a_{xz} & \frac{1}{2}a_{yz} & a_{zz} & \frac{1}{2}a_z \\ \frac{1}{2}a_x & \frac{1}{2}a_y & \frac{1}{2}a_z & a \end{bmatrix} \begin{bmatrix} x \\ y \\ z \\ 1 \end{bmatrix} = 0.$$

When the quadratic surfaces are represented in this form, one may distinguish an 'inside' and an 'outside' of each surface by the condition that

$$f(x, y, z) \begin{cases} > 0 & \text{outside} \\ = 0 & \text{on surface} \\ < 0 & \text{inside,} \end{cases}$$

and one should notice that $-f$ gives the same surface but with the designation of 'inside' and 'outside' reversed. This feature makes it simple to 'bound' the surfaces which are of interest optically with other quadratic surfaces by testing that $f(x, y, z) < 0$ for each bounding surface.

Thus, a cone used for a reflector may be bounded with planes to cut off the parts that are not used, and bounded with the outside of an oblate spheroid describing the PMT to remove a part that would be inside the PMT.

This representation of surfaces is also useful in the evaluation of the surface normal vector (pointing towards the ‘outside’) at some point on the surface, since

$$\hat{\mathbf{n}} = \nabla f,$$

which is easily evaluated in the matrix form above.

A.2 Optical Surfaces

The general quadratics describes the surfaces mathematically, but the optical characteristics of the surfaces must be described as well. This was done by indicating the media that lie on each side of the surface, as well as a scattering probability of the interface that is used for simulating diffuse reflectors. The media are either *metals* with a given reflectivity, or *dielectrics* with a given index of refraction and attenuation length.

The optical surface may also have the characteristic of being a *gate*. Rays that hit gate surfaces cause data about the ray to be entered into histograms, so that the position, time, intensity, etc. of a ray hitting a gate can be recorded. Gates have the option of being totally absorbing, which is generally used if the ray is of no further interest after having hit the gate; otherwise

the optical surface on which the gate is placed acts on the ray in the normal way.

A.3 Sources & Rays

The rays are propagated in ‘vected’ form in sets of about 1,000. This makes the inclusion of partial reflection and transmission straightforward, since it just adds rays to the set. The use of vectorized lists of rays also speeds the calculations. Each ray is represented by a vector of an ID number, position and direction vectors, intensity, and time.

The rays are started from a *source* with unit intensity and random direction. The directions are actually random within bins of $\cos \theta$, and the bins selected sequentially in order to smooth the distribution somewhat and avoid forward/backward asymmetries along the z axis. For a simulation in which fluctuations are of interest rather than the mean values, this feature could be disabled.

There are several standard sources that were used: a simple point source, a line of constant velocity to simulate a particle track, and from random points in a box to simulate an ‘averaged’ response. The ‘time’ value for rays

generated by a line source were initialized according to their position along the line so that slow particles could be simulated with some accuracy.

One iteration of the program propagates the rays from their current position to the next interface that they hit. The new position \mathbf{x}' is calculated from the original position \mathbf{x} and the direction vector \mathbf{v} of the photon

$$\mathbf{x}' = \mathbf{x} + l\hat{\mathbf{v}},$$

and for each quadratic surface the equation

$$f(\mathbf{x}') = 0$$

gives a quadratic equation for l for each ray. The positive real solutions for l are checked against the bounds on the surface, and the minimum l for each ray is taken for all of the optical surfaces in the system. The result of this procedure is the first surface hit by the ray, and the position at which the ray hits that surface.

The ray was then attenuated by its path through the medium, and its 'time' value adjusted. Reflected and refracted rays were then calculated and checks made that the rays should continue propagation. A rather tricky point should be mentioned here: the reflected (and refracted) rays had to be displaced into the media in which they would be travelling on the next

iteration. This was because their starting position on the next iteration would otherwise be on an interface, and the machine accuracy could place them on either side. A displacement of ~ 1 micron was found to be sufficient to cure this problem in most cases. This was not directly dependent on the size of the optical system, but rather on the numerical precision of the computer.

The ray-tracing accuracy was limited by the single precision machine accuracy, but is estimated to be ~ 10 microns for optical configurations of typical ~ 100 cm size. Polarization effects are not included and the rays are always treated as incoherent light for the purposes of reflection and refraction.

Rays are discarded when they miss all optical surfaces (and hence are lost from the apparatus), when their intensity falls below a threshold (typically set at $\approx 10^{-6}$), when they have propagated for a time longer than the maximum allowed (typically ≈ 100 ns), or when they hit an absorbing 'gate.'

Bibliography

- [1] P. A. M. Dirac, *Proc. Roy. Soc.*, **A133**(1931)30.
- [2] S. P. Ahlen, T. M. Liss, C. Lane, and G. Liu, *Phys. Rev. Lett.*, **55**,
No. 2(1985)181.
- [3] D. J. Ficenec, S. P. Ahlen, A. A. Marin, J. A. Musser, and G. Tarlé.
Observation of electronic excitation by extremely slow protons with ap-
plications to the detection of supermassive charged particles. 1987. Sub-
mitted to Physical Review Letters.
- [4] T. M. Collaboration. Proposal for a large area detector dedicated to
monopole search, astrophysics, and cosmic ray physics. 1984.
- [5] G. 't Hooft, *Nucl. Phys.*, **B79**(1974)276.
- [6] A. M. Polyakov, *JETP Lett.*, **20**(1974)194.

- [7] I. G. Koh, Y. D. Kim, Y. J. Park, C. H. Kim, and Y. S. Kim, *J. Math. Phys.*, **23**(1982)1210.
- [8] M. K. Prasad and C. M. Sommerfield, *Phys. Rev. Lett.*, **35**(1975)760.
- [9] M. S. Turner, E. N. Parker, and T. J. Bogdan, *Phys. Rev.*, **D26**(1982)1296.
- [10] J. Arons and R. D. Blandford, *Phys. Rev. Lett.*, **50**(1983)544.
- [11] N. Enterprises. *Scintillators for the Physical Sciences*. Nuclear Enterprises, 1980.
- [12] W. D. Wilson, L. G. Haggmark, and J. P. Biersack, *Phys. Rev.*, **B15**(1977)2458.
- [13] J. Lindhard, M. Scharff, and H. E. Schiøtt, *Mat. Phys. Medd. Dan. Vid. Selsk.*, **33**, No. 14(1963).
- [14] U. Fano, *Ann. Rev. Nucl. Sci.*, (1963)1.
- [15] S. P. Ahlen, *Rev. Mod. Phys.*, **52**, No. 1(January 1980)121.
- [16] S. P. Ahlen, *Phys. Rev.*, **D17**(1978)229.

- [17] Y. Kazama, C. N. Yang, and A. S. Goldhaber, *Phys. Rev.*, **D15**(1977)2287.
- [18] J. Lindhard, *Mat. Fys. Medd. Dan. Vid. Selsk.*, **28**, No. 8(1954).
- [19] S. P. Ahlen and K. Kinoshita, *Phys. Rev.*, **D26**(1982)2347.
- [20] J. B. Birks. *Theory and Practice of Scintillation Counting*. Pergamon, New York, 1964.
- [21] I. B. Berlman. *Handbook of Fluorescence Spectra of Aromatic Molecules*. Academic Press, New York, 2nd edition, 1971.
- [22] S. P. Ahlen and G. Tarlé, *Phys. Rev.*, **D27**(1983)688.
- [23] V. V. Verbinski, W. R. Burrus, T. A. Love, W. Zobel, N. W. Hill, and R. Textor, *Nucl. Inst. Meth.*, **65**(1968)8-25.
- [24] S. D. Drell, N. M. Kroll, M. T. Mueller, S. J. Parke, and M. A. Ruderman, *Phys. Rev. Lett.*, **50**(1983)644.
- [25] L. Bracci, G. Fiorentini, and R. Tripiccione, *Nucl. Phys.*, **B238**(1984)167.
- [26] R. C. Greenwood and R. E. Chrien, *Nucl. Inst. Meth.*, **138**(1976)125.

- [27] S. F. Mughabghab, M. Divadeenam, and N. E. Holden. *Neutron Cross Sections*. Volume 1, Academic, New York, 1981.
- [28] H. Zetterström, S. Schwarz, and L. G. Strömberg, *Nucl. Inst. Meth.*, **42**(1966)277.
- [29] E. Segrè. *Nuclei and Particles*. Benjamin/Cummings, Reading, Massachusetts, 1977.
- [30] C. Renner, N. W. Hill, G. L. Morgan, K. Rush, and J. A. Harvey, *Nucl. Inst. Meth.*, **154**(1978)525-533.
- [31] Y. Furuta, S. Kinbara, and K. Kaieda, *Nucl. Inst. Meth.*, **84**(1970)269-274.
- [32] G. Liu. *In search of Slow-moving Ionizing Massive Particles*. Ph.D. thesis, California Inst. of Technology, 1987.
- [33] B. Barish, G. Liu, and C. Lane. A search for gut monopoles and other ionizing heavy particles using a scintillation detector at the earth's surface. CALT-68-1441, submitted to Phys. Rev. D, June 1987.
- [34] A. de Rújula and S. L. Glashow, *Nature*, **312**(1984)734.

- [35] X. Wen and E. Witten, *Nucl. Phys.*, **B261**(1985)651.
- [36] G. Liu. *First report on MACRO scintillation module at Caltech*. Technical Report 9/85, MACRO Collaboration, 1985.
- [37] W. T. Welford and R. Winston. *The Optics of Nonimaging Concentrators*. Academic Press, New York, 1978.
- [38] G. Tarlé and J. Musser. 1985. private communication.
- [39] G. Liu. *A possible scheme for a MACRO Monopole Trigger Circuit*. Technical Report 1010/85, MACRO Collaboration, 1985.
- [40] M. Severi and L. Petrillo. *Prototype of a Long Signal Digital Detector*. Technical Report 3/86, MACRO Collaboration, 1986.
- [41] C. Peck and R. Batitti. *Scintillation Oil Attenuation Measurements*. Technical Report 9/86, MACRO Collaboration, 1986.